ABSTRACT

Cooling and Heating of the Quantum Motion of Trapped Cd$^+$ Ions

by

Louis Deslauriers

Chair: Christopher R. Monroe

The quest for a quantum system best satisfying the stringent requirements of a quantum information processor has seen tremendous progress in many fields of physics. In the last decade, trapped ions have been established as one of the most promising architectures to accomplish the task. Internal states of an ion which can have extremely long coherence time can be used to store a quantum bit, and therefore allow many gate operations before the coherence is lost. Entanglement between multiple ions can be established via Coulomb interactions mediated by appropriate laser fields. Entangling schemes usually require the ions to be initialized to near their motional ground state. The interaction of fluctuating electric fields with the motional state of the ion leads to heating and thus to decoherence for entanglement generation limiting the fidelity of quantum logic gates. Effective ground state cooling of trapped ion motion and suppression of motional heating are thus crucial to many applications of trapped ions in quantum information science.

In this thesis, I describe the implementation and study of several components of a cadmium-ion-based quantum information processor, with special emphasis on the

control and decoherence of trapped ion motion. I first discuss the building and design of various ion traps that were used in this work. I also report on the use of ultrafast laser pulses to photoionize and load cadmium ions in a variety of rf Paul trap geometries. A detailed analysis of the photoionization scheme is presented, along with its dependence on controlled experimental parameters. I then describe the implementation of Raman sideband cooling on a single trapped ^{111}Cd$^+$ ion to the ground state of motion, where a ground state population of 97% was achieved. The efficacy of this cooling technique is discussed with respect to different initial motional state distributions and its sensitivity to the presence of motional heating. I also present an experiment where the motion of a single trapped ^{112}Cd$^+$ ion is sympathetically cooled by directly Doppler cooling a ^{114}Cd$^+$ ion in the same trap. The implications of this result are relevant to the scaling of a trapped ion quantum computer, where the unwanted motion of an ion crystal can be quenched while not affecting the internal states of the qubit ions. In order to understand the origin of heating in ion traps, a series of controlled measurements of trapped ion motional heating was performed, where the proximity of the ion to the electrodes and the temperature of the electrodes is varied. These measurements are carried out in a novel moveable ion trap structure that confines laser-cooled ions closer to the electrodes than any previous ion trap. This study sheds light on an important but poorly understood source of decoherence in ion traps and possibly other charge-based quantum systems.

Cooling and Heating of the Quantum Motion of Trapped Cd$^+$ Ions

by

Louis Deslauriers

A dissertation submitted in partial fulfillment

of the requirements for the degree of

Doctor of Philosophy

(Applied Physics)

in The University of Michigan

2006

Doctoral Committee:

"Never take life seriously. Nobody gets out alive anyways."

– Anonymous

To my wife, daughter, mom, dad, and sister

ACKNOWLEDGEMENTS

My academic journey has been shaped in large part by the people whom I have studied with, learned from, taught, etc. But or course it all started with my family. I want to thank my mother for always encouraging me to ask questions. And oddly enough, for my dad to show me that it was ok to not have an answer for everything. He would never try to pretend that he understood more than he actually did. Thanks also to my sister for believing so much in my capabilities.

My wife and my daughter, whom I cannot imagine life without, always remind me that there is so much that makes life worth living. My wife has always been very supportive of my goals and helped me believe I can succeed. My daughter, well, is always in my mind throughout the day - she helps me in every way, she just doesn't know it yet. They both have and still are playing a large part in the culmination of my studies - I thank them from the bottom of my heart.

My undergraduate experience at Embry-Riddle Aeronautical University was very fullfilling. I wish to thank professor Abas Sivjee for giving me the physics rigor needed to succeed in my graduate work. He is a dedicated teacher. I also want to thank two very special friends: professors Elliott Jacobs and Carol Jacobs. They have played an instrumental role in giving me the intellectual curiousity necessary in succeeding academically.

Understandably, my colleagues here at the University of Michigan have had a very tangible impact on the completion of this thesis. First, I want to thank all my professors that have taught me so much physics. In particular, I want to thank professor Paul Berman for giving me so much of his time through my years here in

the department. I really value his generosity. When I may have let doubts overcome my ability to perform, professor Jens Zorn has always been a consistant source of confidence. For instance, every semester he would generously allow me to be a guest lecturer in his classes. He has been a true inspiration. Other thanks go to Dr. Ralph Conti whom I have the greatest esteem for. His tremendous knowledge of physics and his humility is something I truly admire. Again, so many times he would patiently explain complicated atomic physics concepts until I fully understood. I also wish to thank professor Duncan Steel and Phil Bucksbaum for serving on my dissertation committee. I only wish circumstances would have allowed for more interaction with them; I find both of them to be particularly interesting individuals. Lately, I have to say, I have especially benefited from Phil Bucksbaum's advices regarding my upcoming post-doc at Stanford. I am also very thankful of the help that Richard Vallery and Steve Katnik have provided in my last year of work. Richard has, among other things, given me a lot of tips and tricks with the writing of this thesis, and Steve has been an incredible help in the building of a long-wavelength mode-locked Ti:Sapphire pulsed laser.

Now comes my research group - a truly impressive crew. I have learned so much from everyone, they all are so capable. I very much treasure their friendship: Mark Acton, Boris Blinov, Kathy-Anne Brickman, Paul Haljan, Winfried Hensinger, David Hucul, Rudy Kohn Jr., Patricia Lee, Martin Madsen, Peter Maunz, Russel Miller, David Moehring, Steve Olmschenk, Elizabeth Otto, Jim Rabchuck, Jon Sterk, Dan Stick, Mark Yeo, and Kelly Younge. Now, there is something that I am very anxious to aknowledge: my infinite gratitude to two post-doctoral fellows that I have worked with and also spent a lot of time with - Paul Haljan and Winfried Hensinger. First of all these two guys are amazing scientists! They both have taught me so much, it is literally impossible for me to enumerate all of their contributions to my becoming a scientist. I will always be grateful for their constant generous help. Another post-doctoral fellow that I worked with at the beginning of my tenure in this lab is Boris Blinov. I also have a very high esteem of Boris. He has also taught me a great deal. Finally, my advisor Christopher Monroe. Instead of listing all that I am indebted to

him, I will simply recount a simple but telling anecdote. Each time someone asks me if professor Christopher Monroe is a good advisor (which happens frequently), my answer is very simple: "nobody comes even close, period!!" Now, I believe he is exactly the advisor that I needed. Chris, thank you for everything you have given me. You are truly amazing.

TABLE OF CONTENTS

LIST OF TABLES

LIST OF FIGURES

CHAPTER 1

Introduction

In the last fifty years, the ability to store and manipulate single atoms has opened up many new possibilities for studying the implications of quantum mechanics in systems that are accessible. It is well known that quantum theory allows for a system to be placed in a superposition of states, and that these superposed states can interfere with one another while undergoing unitary evolution. When quantum superposition involves different parts of a larger system, the different subsystems can be found in correlated states, which are often referred to as entangled states. It was recognized early on that that these phenomena form one of the most intriguing parts of quantum mechanics [1, 2], and the concept of quantum entanglement is now thought to form the basis of the emerging fields of quantum information and quantum computation [3, 4].

In order to study and apply these concepts, it is desirable to have the ability to confine and manipulate single atoms in a well-controlled manner. Larger systems with many degrees of freedom are not currently convenient platforms for testing these quantum phenomena because of the uncontrolled interactions between the individual atoms. Ideally, the degrees of freedom involved in a single atom system (motion and the internal levels) should be prepared in well defined states and then manipulated in a precise manner. The ion trap, which confines charged particles by coupling to their excess charge, allows for the aforementioned degree of control. Charged particles can typically be confined for hours in potentials that are up to several electron-volts deep, without perturbing the internal states.

The main categories of ion traps are the Penning and rf Paul traps [5]. The Penning trap uses a combination of static electric and magnetic fields to confine the charged particles [6]. The first observation of individual trapped charged particles involved electrons in a Penning trap, and was based on work done in 1973 at the University of Washington by Hans Dehmelt and coworkers [7]. On the other hand, the rf Paul trap dynamically confines charged particles with quadrupole rf electric fields [8]. In 1980, a single Ba^+ ion was confined in an rf Paul trap, also by Dehmelt and coworkers [9]. The invention of the Penning trap is attributed to Hans Georg Dehmelt, while Wolfgang Paul is credited with inventing the rf Paul trap. They both shared one half of the Nobel Prize in Physics in 1989 for their work; the other half was awarded to Norman Ramsey for his work on the separated oscillatory fields method and its subsequent use in the hydrogen maser and atomic clocks [10]. The use of static electric and magnetic fields in the Penning trap has one major advantage over the rf Paul trap in that there is no "micromotion" and resultant heating of the ion due to the dynamic fields. However, laser cooling in the Penning trap is more complicated because one degree of motion (the magnetron motion) is not stable and cannot be cooled directly. The rf Paul trap does not suffer from this drawback, as all motional degrees of freedom can be cooled directly. This makes it perhaps more appropriate for quantum computing applications which use the motional degree of freedom to couple the ions. For this reason, the experiments presented here are performed using only rf Paul traps.

The discovery of laser cooling of atoms was a major advance, enabling the precise control of trapped ions and many other seminal experiments in the atomic physics field. Today it has become an essential tool with many applications, from precision frequency metrology to quantum information science and fundamental studies of quantum mechanics. Laser cooling of atoms was first proposed jointly by two research groups: Wineland and Dehmelt [11] for studying harmonically bound atoms and by Hänsch and Schawlow for studying free neutral atoms [12]. The first demonstrations came three years later with the work of Wineland and Dehmelt [13] using magnesium ions and independently by Neuhauser *et al.* [14] using barium ions. More specifically,

these laser cooling schemes used a technique referred to as Doppler cooling. While this was sufficient for many applications, cooling to the ground state of motion was not achieved until 1989, when Wineland's group at NIST implemented another type of laser cooling on Hg^+ [15], known as resolved sideband cooling. Since then slight variations of the scheme have been used to cool other ion species to the motional ground state. In 1995 the NIST group cooled Be^+ in all three dimensions of motion, this time using a two photon resolved sideband cooling technique [16]. In 1999, Ca^+ was cooled on a narrow electric quadrupole allowed transition [17]. Some of the work for this thesis (first performed in 2004) involved cooling Cd^+ to its ground state [18], also using a two photon resolved sideband technique.

The explosion of interest in quantum computing following Peter Shor's discovery of a quantum factoring algorithm in 1994 [19] resulted in increased theoretical interest in finding physical systems amenable to implementing universal quantum gates. In 1995 Cirac and Zoller presented the first formal proposal for implementing a quantum gate with trapped ions [20]. It was implemented a few months later by the NIST group [21], who took advantage of the many experimental techniques which had grown out of the efforts to build frequency standards with cooled trapped ions [22]. The Cirac-Zoller scheme involves entangling the internal states of the ions by coupling their collective quantized motion. A particular disadvantage of this scheme is that it requires the ion to be cooled to and remain near the ground state, making the fidelity of quantum logic gates sensitive to motional decoherence due to anomalous heating. Later theoretical proposals [23, 24, 25] somewhat relaxed the constraints on cooling to the ground state before operating a quantum gate, but are still sensitive to heating during gate operations. The source of this heating is still poorly understood; every ion trap in which heating has been measured [15, 26, 17, 27, 28] has shown a heating rate many orders of magnitude above the expected heating rate from fundamental mechanisms (Johnson noise). Understanding this decoherence is expected to become even more critical as ion traps become weaker in order to support larger ion crystals and allow shuttling of ions through complex and microscale electrode structures.

In this thesis, I describe the implementation and study of several components of

a Cadmium-ion-based quantum information processor with special emphasis on the control and decoherence of trapped ion motion. The first part of the thesis (chapters 1-4) describes the basic components involved in the experiments. In chapter 2 I discuss the building and design of different ion trap geometries. Ancillary components necessary for the ion trap, such as the vacuum technology and ovens, are also described in detail. Chapter 3 presents the characteristic energy levels of the cadmium ion and the various laser-ion interactions used to manipulate them. In chapter 4, I describe the experimental setup of the laser system and the experimental control and data aquisition systems. The second part of the thesis (chapters 5-7) presents the experimental results. Chapter 5 discusses a clean and efficient ion trap loading technique using photoionization with ultrafast pulses. With reasonable amounts of laser power, this technique can nearly ionize every atom traversing the laser beam within the trapping volume. In chapter 6 the laser cooling and sympathetic cooling techniques used in these experiments are presented. I discuss the experimental results, in particular the efficacy of these cooling techniques with respect to different initial motional state distributions and their sensitivity to the presence of motional heating. Chapter 7 presents a series of controlled measurements of trapped ion motional heating, where the proximity of the ion to the electrodes and the temperature of the electrodes are varied. These measurements are carried out in a novel moveable ion trap structure that confines laser-cooled ions closer to the electrodes than any previous ion trap. This study sheds light on an important but poorly understood source of decoherence in ion traps and possibly other charge-based quantum systems.

CHAPTER 2

Ion trap technology

Significant advances in physics can often be traced back to the invention of a new device. There are a few modern examples that come to mind: the laser, the electron microscope, stable RF sources, etc. These inventions all have triggered tremendous progress in the understanding of many different phenomena. The radiofrequency ion trap (i.e. rf Paul trap), while not in the same influential category as the laser, falls within the general realm of devices that have spawned new advances in physics. The rf Paul trap used in this work was first proposed and experimentally verified in the 1950's in professor Wolfgang Paul's laboratory in Bonn, Germany. The ability to store and interrogate a single atom for an extended period of time has led to several astonishing experimental observations. Notably, zero-point laser cooling of a trapped atom [15, 16], observation of quantum jumps [29, 30, 31], realization of the first quantum logic gate [21], entanglement of an atom and a photon [32], etc. Currently, the rf Paul trap system is seen as an ideal platform to harbor a quantum information processor. This chapter will describe the rf Paul traps used in this work and the technology associated with their operations.

2.1   The Paul trap: Exact 3-D rf quadrupole potential

It is well known that a static electric field cannot produce a three dimensional confining potential in free space. In other words, any electrostatic potential obeying the Laplace equation does not have a minima in its solution - a result embodied in Ernshaw's theorem [33]. To circumvent this electrostatic constraint, two different

solutions were proposed and experimentally verified in the 1950's - the Penning and the rf Paul ion traps. The Penning ion trap uses a combination of a static magnetic field and a static quadrupole electric field to confine the charged particles, while the rf Paul trap uses time dependent quadrupole electric fields to dynamically trap the charged particles. The development of these powerful trapping techniques is generally attributed to the efforts of Wolfgang Paul and Hans Dehmelt; they both shared the 1989 Nobel prize for their contributions. For the applications of trapped ions relating to quantum computing, the rf Paul trap seems, so far, to be the most suitable technique since every motional degree of freedom can be cooled to the ground state [5]. For this reason, the work described in this thesis is conducted in several types of rf Paul traps (to be described in the next section of this chapter).

The essence of the how the rf Paul trap can dynamically confine an ion relies on its ability to produce a three dimensional (3-D) trapping time-averaged potential. The confining pseudo-potential produced by the rf Paul trap is 3-D simple harmonic oscillator potential:

$$\Psi(x, y, z) = \frac{m}{2}(\omega_x^2 x^2 + \omega_y^2 y^2 + \omega_z^2 z^2), \tag{2.1}$$

where m is the ion mass and ω_x, ω_y, and ω_z are the harmonic frequencies associated with the x, y, and z directions, respectively. Such a harmonic oscillator pseudo-potential can be produced by applying an rf potential to the trap electrodes, as shown in Fig. 2.1. The hyperbolic shaped electrodes, consisting of a "ring" electrode and two "endcap" electrodes, give rise to a quadrupole potential

$$V(x, y, z, t) = (U_0 + V_0 cos(\Omega_{rf}t)) \left[\frac{1}{2} - (\frac{x^2 + y^2 - 2z^2}{d_T^2})\right] \tag{2.2}$$

where

$$d_T^2 \equiv r_0^2 + 2z_0^2 \quad \text{with} \quad r_0^2 = 2z_0^2. \tag{2.3}$$

Here U_0 and V_0 are the amplitudes of the static and rf voltages applied to the end-cap electrodes (the ring electrode is held at ground), r_0 is the radius of the ring electrode and $2z_0$ is the distance between the endcaps, and $\Omega_{rf}/2\pi$ is the rf drive frequency.

The classical equation of motion (along the ith direction) for an ion immersed in such a potential reads

$$m\ddot{r}_i = -e(\vec{\nabla}V(x,y,z,t) \cdot \hat{r}_i), \tag{2.4}$$

where e is the charge of the ion. These equations can be transformed, through simple substitutions, into the Mathieu equation [34]. Along the x-direction, the equation reads

$$\frac{\partial^2 x}{\partial \tau^2} + [a + 2q cos(2\tau)]x = 0, \tag{2.5}$$

where we have defined

$$\tau \equiv \frac{1}{2}\Omega_{rf}t, \quad a \equiv \frac{8eU_0}{m\Omega_{rf}^2(r_0^2 + 2z_0^2)}, \quad \text{and} \quad q \equiv \frac{4\mathrm{e}\,V_0}{m\Omega_{\mathrm{rf}}^2(\mathrm{r}_0^2 + 2\mathrm{z}_0^2)}. \tag{2.6}$$

Note that the equation along the y-direction is identical to Eq. (2.5), whereas for the z-direction the parameters a and q are simply multiplied by a factor of -2.

The solution to the equation of motion (Eq. 2.5) for each direction of motion ultimately yields the expected oscillatory solution of a harmonic oscillator. However, even though the Mathieu equation is a "linear" differential equation, it cannot be solved analytically in terms of standard functions. The reason is that one of the coefficients isn't constant but time dependent. Fortunately, the coefficient is periodic in time; allowing the use of the well known Floquet theorem [34].

Before the full analytical solution to the ion trajectory is presented, which can be tedious, a simple and easy to remember form for the ponderomotive pseudo-potential is given. This shortcut follows from a heuristic derivation [35]. If satisfied, the reader may then want to skip the somewhat formal derivation of the Mathieu equation's solution that will follow.

Using convincing physical arguments, it is easy to derive the form of the ponderomotive pseudo-potential that results when an ion is immersed in a potential like that in Eq. 2.2, with static voltage U_0 set to zero [35]. The pseudo-potential that results is

$$\Psi(x,y,z) = \frac{e^2}{2m\Omega_{rf}^2}\left\langle \left|\vec{E}(x,y,z,t)\right|^2 \right\rangle_{avg}, \tag{2.7}$$

where the expression is to be averaged over a time interval of $T = \pi/\Omega_{rf}$.

From here it is very easy to see how the harmonic oscillator pseudo-potential comes about. The quadrupole electric field is first computed from Eq. 2.2, resulting in

$$\vec{E}(x,y,z,t) = \left[\frac{V_0 cos(\Omega_{rf}t)}{d_T^2}\right](2x\hat{x} + 2y\hat{y} - 4z\hat{z}), \tag{2.8}$$

note that the divergence of the electric field $\vec{E}$ is zero ($\nabla \cdot \vec{E}$=0) as required by Earnshaw's theorem. Next, the electric field is inserted into the above equation (Eq. 2.7), leading to the anticipated harmonic oscillator trapping potential

$$\Psi(x,y,z) = \frac{e^2}{m\Omega_{rf}^2}\left[\frac{V_0^2}{d_T^4}\right](x^2 + y^2 + 4z^2). \tag{2.9}$$

By comparing Eq. 2.1 and Eq. 2.9, we deduce the harmonic oscillator trap frequency along the z-direction to be

$$\omega_z = \frac{2\sqrt{2}eV_0}{m\Omega_{rf}d_T^2}, \tag{2.10}$$

where the frequencies along the x and y directions are ω_x=ω_y=$(1/2)\omega_z$. The effect of applying a nonzero static voltage U_0 on the end-cap electrodes is a change in the ratio of the radial (ω_x, ω_y) and vertical (ω_z) oscillation frequencies. For instance, a positive voltage applied on the end-cap electrodes has the effect of increasing ω_z at the expense of ω_x and ω_y.

Now we turn to a more rigorous treatment of the solution to the Mathieu equation (Eq. 2.5). This time, in addition to the rf voltage considered so far, we include the effect of an applied static voltage U_0. This analysis will show the inherent complexity of the full ion trajectory. Additionally it will show that the ponderomotive pseudo-potential solution described in [35], with U_0=0 Volts, is usually an excellent approximation to the ion trajectory.

By making use of the Floquet theorem the general solution to the Mathieu equation reads

$$x(\tau) = Ae^{+i\mu\tau}\phi(\tau) + Be^{-i\mu\tau}\phi(-\tau). \tag{2.11}$$

Here A and B are constants to be determined by simple initial conditions and

$U_o + V_o \cos(\Omega t)$

Top end-cap

z_o

Ring

r_o

Bottom end-cap
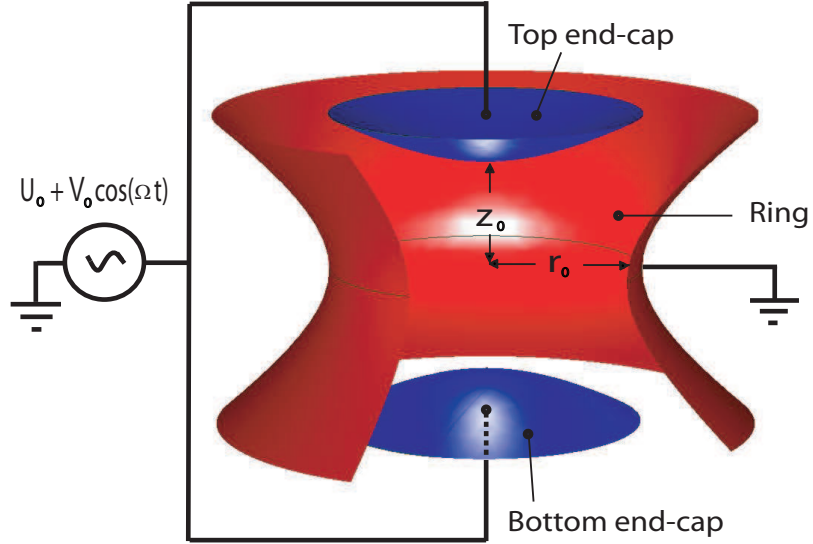
Figure 2.1: Schematic of the electrodes for a 3-D rf Paul trap with a cylindrically symmetric electrode configuration. The rf and static voltages are applied simultaneously to the end-cap electrodes while the ring electrode is held at ground. An exact quadrupole potential results when the electrode configuration satisfies $r_0^2 = 2z_0^2$. Typical dimensions for the inter-electrode distance are $r_0 = \sqrt{2}z_0$=50-500 μm, with V_0=100-2000 Volts, U_0=0-100 Volts, and $\Omega_{rf}/2\pi$=10-250MHz.

$$\phi(\tau) = \phi(\tau + \pi) = \sum_{n=-\infty}^{\infty} c_n e^{2in\tau}. \tag{2.12}$$

is a periodic function.

When the characteristic exponent μ has an imaginary component, the motion $x(\tau)$ contains an exponentially growing contribution, leading to unstable motion. But if instead the characteristic exponent μ is purely real, the solution is bounded and thus stable. The parameters a and q, dependent on the static and rf voltages applied to the trap electrodes, determine if the motion is stable or not.

In order to determine the stability of the ion trajectory along the x-direction [1], given particular values for a and q, we substitute the Floquet trial solution

$$\phi(\tau) = \sum_{n=-\infty}^{\infty} c_n e^{i(2n+\mu)\tau} \tag{2.13}$$

into the Mathieu equation (Eq. 2.5) and arrive at

$$\sum_{n=-\infty}^{\infty} \left\{ [-(2n+\tau)^2 + a]c_n e^{i[2n+\mu]\tau} + qc_n(e^{i[2(n+1)+\mu]\tau} + e^{i[2(n-1)+\mu]\tau}) \right\} = 0.$$

Then, by shifting the indices of the second and third term, $n \rightarrow n-1$ and $n \rightarrow n+1$, respectively, we recover the three term recurrence relation

$$[-(2n+\tau)^2 + a]c_n + qc_{n-1} + qc_{n+1} = 0. \tag{2.14}$$

When written into a matrix form, this recurrence relation becomes

$$M\vec{c} = \begin{pmatrix} & \vdots & \vdots & \vdots & \vdots & \vdots & \\ \cdots & q & -(-2+\mu)^2 + a & q & 0 & 0 & \cdots \\ \cdots & 0 & q & -\mu^2 + a & q & 0 & \cdots \\ \cdots & 0 & 0 & q & -(2+\mu)^2 + a & q & \cdots \\ & \vdots & \vdots & \vdots & \vdots & \vdots & \end{pmatrix} \begin{pmatrix} \vdots \\ c_{-2} \\ c_{-1} \\ c_0 \\ c_1 \\ c_2 \\ \vdots \end{pmatrix} = \vec{0}.$$

---

[1] Recall that the Mathieu Equation reads the same along the y-direction whereas for the z-direction the parameters a and q are simply multiplied by a factor of -2.

For a non-trivial solution to this equation ($\vec{c} \neq 0$), the inverse of the matrix M should not exist. In other words, the determinant of M must be zero [2].

$$\det M = \det \begin{pmatrix} \vdots & \vdots & \vdots & \vdots & \vdots \\ \cdots\ q & -(-2+\mu)^2 + a & q & 0 & 0\ \cdots \\ \cdots\ 0 & q & -\mu^2 + a & q & 0\ \cdots \\ \cdots\ 0 & 0 & q & -(2+\mu)^2 + a & q\ \cdots \\ \vdots & \vdots & \vdots & \vdots & \vdots \end{pmatrix} = 0$$

(2.15)

It is non-trivial to find the characteristic exponent μ for any given value of the dimensionless a and q voltage parameters. Usually, in order to access the exponent μ, one is required to use numerical techniques. Nevertheless, solving this determinant is extremely helpful as it provides a stability diagram for the solution of the ion trajectory along each direction of motion[8]. Three dimensional confinement of the ion is achieved when both the radial x-y motion and the "vertical" z-motion are stable simultaneously. These constraints imposed on the voltage parameters a and q can be best assessed with the help of such a stability diagram [3].

Fortunately, for the vast majority of experimental settings, the value of the dimensionless voltage parameters a and q are both smaller than unity ($|a| << 1, q < 1$) - allowing the determinant of the matrix M to be solved analytically. Indeed, in the limiting case where $|a| << 1$ and $q < 1$, the matrix M can be reduced to a 3×3 matrix around $n = 0$,

$$M\,\vec{c}_{reduced} = \begin{pmatrix} -(-2+\mu)^2 + a & q & 0 \\ q & -\mu^2 + a & q \\ 0 & q & -(2+\mu)^2 + a \end{pmatrix} \begin{pmatrix} c_{-1} \\ c_0 \\ c_1 \end{pmatrix} = \vec{0}. \quad (2.16)$$

Solving the above set of equations (Eq. 2.16) yields a value for the characteristic Floquet exponent of

---

[2] Recall that the inverse of the matrix M goes as $M^{-1} = \frac{\text{cofactor}\,M}{\det M}$

[3] For more information on the stability diagram of the Paul trap, the reader is referred to a very nice/clear treatment of the topic in [8]

$$\mu^2 = \frac{1}{2}q^2 + a. \tag{2.17}$$

At this point, we can already gain some insight into the stability diagram of the ion trajectory (for the special case of $|a| \ll 1$, $q < 1$). For a stable solution, the Floquet exponent μ is not allowed to have an imaginary component, hence the stability condition $\mu^2 = \frac{1}{2}q^2 + a \geq 0$.

Having the characteristic Floquet exponent μ now yields the following corresponding values for the coefficients c_{-1} and c_1, both in terms of the coefficient c_0:

$$c_{-1} = qc_0 \quad \text{and} \quad c_1 = qc_0.$$

Plugging these value of c_n's into the Floquet solution (Eq. 2.11) yields, at last, the complete solution of the ion trajectory. This of course, is in a limited region of the a-q parameter space, but as mentioned earlier, this particular region of the a-q stability diagram is usually the *assumed* mode of operation in an rf Paul trap. The solution for $x(\tau)$ reads

$$x(\tau) = Ac_0(e^{i[\mu\tau]} + qe^{i[2+\mu]} + qe^{i[-2+\mu]}) + Bc_0(e^{-i[\mu\tau]} + qe^{-i[2+\mu]} + qe^{-i[-2+\mu]}).$$

The above expression in its most transparent form reads

$$x(t) = 2Ac_0 cos(\omega_x t)\left[1 - \frac{q}{2}cos(\Omega_{rf}t)\right], \tag{2.18}$$

where, without loss of generality, we made use of the initial condition $A = B$, and inserted $\tau = \Omega_{rf}t/2$. Most importantly we identify the Floquet exponent μ as being proportional to the trap secular frequency along the x or y direction of motion [4], where

$$\omega_x \equiv \frac{\Omega_{rf}}{2\sqrt{2}}\mu = \frac{\Omega_{rf}}{2}\sqrt{\frac{q^2}{8} - \frac{a}{2}}. \tag{2.19}$$

Upon examination of Eq. 2.18, we find that the ion motion $x(t)$ is made up of two superimposed components: a slow (*secular*) oscillatory motion at the trap frequency ω_x, and a fast component synchronous with the applied rf frequency Ω_{rf} (*micromotion*). The rf voltage parameter q is generally assumed to be smaller than

---

[4]The trap frequency along the z-direction is obtained by multiplying the voltage parameters a and q by a factor of -2.

unity. In this case, the amplitude of the micromotion is a factor $q/2$ smaller than the amplitude of the secular motion. If the micromotion can be neglected, the motion is then purely that of a three dimensional harmonic oscillator with oscillation frequencies ω_x, ω_y, and ω_z.

The presence of a static background electric field at the center of the ion trap modifies Eq. 2.18 somewhat. Assuming an electric field with component E_0 along the x-direction, the equation of motion (Eq. 2.5) becomes

$$\frac{\partial^2 x}{\partial \tau^2} + [a + 2q cos(2\tau)]x = \frac{eE_0}{m}, \tag{2.20}$$

with solution

$$x(t) = x_0 cos(\omega_x t)\left[1 - \frac{q}{2}\cos(\Omega_{rf}t)\right] + \frac{eE_0}{m\omega_x^2} + \frac{\sqrt{2}eE_0}{m\omega_x\Omega_{rf}}\cos\left(\Omega_{rf}t\right). \tag{2.21}$$

The effect of the background static electric field is seen in the third and fourth term of Eq. 2.21. The third term represents a constant offset $x(E_0)$ in the position of the ion from the rf node at the center of the trap. The "excess" micromotion that results from the driven motion at frequency Ω_{rf} is represented in the fourth term. This excess micromotion differs from the unavoidable micromotion associated with the secular motion of amplitude x_0 in that it cannot be laser cooled because it is driven motion. The presence of excess micromotion has several adverse effects, including reduced ion trapping lifetime, significant second order Doppler shifts in spectroscopic studies, and broadening of the atomic transitions [36]. In this experiment, the excess micromotion typically caused a significant broadening of the cycling transition used for Doppler cooling, which prevented the ion motion from being laser cooled to its ground state (chapter 6) and it also supressed Raman Rabi frequencies from Debye-Waller effect. In order to cancel the background static electric field E_0, static voltages are applied to compensation electrodes positioned along each principle axis of the ion trap (sections 2.2.1 and 2.2.2).

The harmonic oscillation associated with the secular motion plays a crucial role in all modern experiments conducted in an rf Paul trap. In general, the ion-trap system consists of two independent quantum systems: the electronic internal levels and the

quantized harmonic motion of the ion. As we will see in the following chapters, these two simple quantum systems can be addressed independently or coupled directly with the use of appropriate laser beams.

2.2   Ion traps used in this work

The 3-D rf Paul trap discussed in the previous section is an *ideal* model. That is, the vast majority of ion traps in use today do not have a hyperbolic electrode geometry giving rise to the exact quadrupole potential discussed above. As we will see, the building of perfectly hyperbolic trap electrodes is unnecessarily cumbersome. In fact, the shape of the electrodes seldom resembles the ideal model, yet in the neighborhood of the trap center the *exact* solution described in the previous section is a very good approximation.

There are two classes of Paul traps in use today – the three dimensional ion trap and the linear (two dimensional) ion trap. The 3-D Paul trap provides a confining potential with respect to a single point in space and therefore is mostly used in single ion experiments. On the other hand, the rf fields applied on the electrodes of a linear ion trap provide two dimensional transverse confinement. Additional static electrodes provide for the longitudinal confinement - yielding a *static* trap along this direction.

In this section I will summarize all ion traps that have been used for this work; 3-D Paul traps (2.2.1) and linear Paul traps (2.2.2).

2.2.1   3-D quadrupole traps

The work in this thesis was conducted over several years, and comprises different types of experiments. In order to accommodate the various research directions through the years, several different rf Paul traps were built. The first two traps built for the work in this thesis consisted of a simple, yet very robust *ring-and-fork* design [37]. A schematic of the ring-and-fork traps is shown in Fig. 2.2; both traps were built identically to one another.

The ring-and-fork trap consists of two thin sheets of molybdenum, 125μm thick. One sheet has a hole in it (*ring* electrode) with radius $r_0 \simeq 200$ μm, while the other sheet, perpendicular to the ring electrode, has a gap (*fork* or endcap electrode) with spacing $2z_0 \simeq 300$ μm. As mentioned earlier, the resulting confining potential near the rf node, is, to a good approximation, a quadrupole. Higher order terms or anharmonicities of the potential can, in general, be neglected since the excursion of the ion is typically small, i.e. the ion remains near the trap center.

The only difference encountered in dealing with a non-ideal electrode configuration such as the ring-and-fork trap is a *voltage efficiency factor* $0 < \epsilon \leq 1$, which characterizes the reduction in trap confinement compared to the analogous quadrupole rf trap with ideal hyperbolic electrodes. Additionally, the cylindrical symmetry characterizing the ideal hyperbolic electrode configuration is broken when using the ring-and-fork design. The $\vec{E}$-field gradient giving rise to the restoring force is weakest along the direction of the fork; we define the x-axis to be along this direction. This is actually a very useful feature as it allows Doppler cooling with a single laser beam (see chapter 2). The secular frequencies are

$$\omega_x = \frac{\Omega}{2}\sqrt{\frac{\alpha^2}{2}(\epsilon q)^2 - \alpha\epsilon a}, \;\; \omega_y = \frac{\Omega}{2}\sqrt{\frac{(1-\alpha)^2}{2}(\epsilon q)^2 - (1-\alpha)\epsilon a}, \;\; \omega_z = \frac{\Omega}{2}\sqrt{\frac{1}{2}(\epsilon q)^2 + \epsilon a}, \tag{2.22}$$

where $0 < \alpha \leq 1/2$ characterizes the radial trap anisotropy ($\alpha=1/2$ for cylindrically symmetric electrodes).

In general the trap frequencies can be calculated with the help of the formulas in Eq. 2.22, but this requires precise knowledge of the voltage efficiency ϵ and the trap anisotropy α parameters. However, for most electrode configurations these quantities are very difficult to obtain analytically. One is usually forced to use numerical techniques in order to obtain these parameters.

Generally, the trap frequencies are directly measured and then used to obtain the trap parameters ϵ and α. One common method used to measure the secular frequencies is straightforward [5]. A small sinusoidal voltage on the order of 1 V is

---

[5]In addition to the technique presented here, we will show in chapter 3 that the trap frequencies

applied to one of the trap electrodes; either the ring or the fork. The secular frequency is measured by sweeping the applied frequency across the motional resonance. The feedback is very clear – the image of the ion becomes "fuzzy" as the ion motion becomes excited by the resonant drive. Using this type of measurement allows the trap frequencies (typically a few MHz) to be determined well within an error of 10 kHz.

Using this simple technique, some ring-and-fork trap parameters were measured: when applying an rf voltage of $V_0 \simeq 400$ Volts with a drive frequency of $\Omega/2\pi = 50$ MHz, and a static potential $U_0 = 30$ Volts, The resulting trap secular frequencies are $(\omega_x, \omega_y, \omega_z)/2\pi \approx (5.8, 8.9, 9.7)$MHz. For $U_0 = 6$ Volts, the trap frequencies are $(\omega_x, \omega_y, \omega_z)/2\pi \approx (4.8, 7.4, 11.3)$MHz.
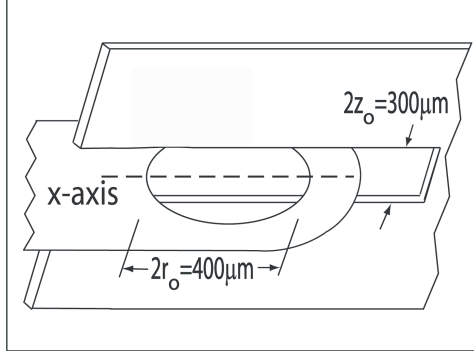
Figure 2.2: Schematic diagrams for the two identical *ring-and-fork* ion traps used in this experiment. It is an asymmetric ($\omega_x < \omega_y$) quadrupole trap with closest electrode distance $z_0 = 150$ μm (fork electrode). The ring electrode has a circular hole in it, with a diameter of $2r_0 \simeq 400$ μm. Both electrodes are constructed from 125 μm thick molybdenum sheets. Compensation of static background electric fields is achieved by applying appropriate static voltages (~ 2000 Volts) on three metallic electrodes (not shown in figure) pointing along each axis of the ion trap.

Additional auxiliary electrodes are added in order to compensate for uncontrolled background electric fields. These fields, when left uncompensated, displace the ion

---

can also be obtained with the use of stimulated Raman transitions.

from the rf node and hence cause an undesirable increase of the micromotion amplitude experienced by the ion. All three compensation electrodes are located at a distance of $\sim$ 1cm from the trap center, and each is positioned along a particular axis of the ion trap. Thus applying appropriate static voltages on each one of them allows cancellation of stray $\vec{E}$-fields pointing in an arbitrary direction. Typical voltages applied to the ring-and-fork's compensation electrodes are around 2000 Volts. The need for such large voltages stems from the fact that the effect of the compensation electrodes is greatly reduced due to the efficient shielding provided by the *ring* and *fork* metallic electrodes.

A third 3-D rf Paul trap was built for the investigation of motional heating in ion traps (chapter 7). It consists of a cylindrically symmetric ($\alpha = 1/2$) electrode structure formed by two opposing tungsten needle-tipped electrodes. They are mounted on independent translation stages which allows for the tip-to-tip electrode separation $2z_0$ to be controllably varied over a wide range $0 \leq 2z_0 \leq 1$ cm with micrometer resolution. This variable ion trap geometry gives the ability to study how the anomalous motional heating of trapped ions scales as a function of trap size (as detailed in chapter 7).

2.2.2 Linear traps

The characteristic feature of a linear Paul trap is its ability to confine a string of ions along a line (i.e. the rf node line). This is a crucial feature of a trapped ion quantum register, where linear arrays of ions are required [20]. In a linear Paul trap, the three-dimensional confinement is realized by the superposition of two confining potentials: (1) a transverse ponderomotive rf potential, and (2) a longitudinal static potential. In Fig. 2.3 is a schematic of the electrode configuration for a generic linear Paul trap. The rf voltage provides the transverse (x-y) two-dimensional ponderomotive confinement, while leaving the longitudinal z-direction unaffected. For longitudinal confinement, appropriate static voltages are applied to the "endcap" electrodes. The resulting static trap along the z-axis provides for static confinement

of the ions, leading to a very simple description of the longitudinal motion. The potential resulting from applying a static voltage U_0 on all endcaps reads

$$V_{DC}(x,y,z) = \frac{\kappa U_0}{z_0^2}\left[z^2 - \frac{1}{2}(x^2+y^2)\right] = \frac{1}{2e}m\omega_z^2\left[z^2 - \frac{1}{2}(x^2+y^2)\right],\qquad(2.23)$$

where κ is a voltage efficiency factor for the static electrodes, $\omega_z/2\pi$ is the longitudinal trap frequency, m represents the mass of the ion and e its charge, and

$$\omega_z = \sqrt{\frac{2eU_0\kappa}{mz_0^2}}\qquad(2.24)$$

is the longitudinal trap frequency. As seen in Eq. 2.23, the transverse direction is also affected by the static potential; in fact it leads to anti-trapping along the transverse x-y plane. This, however, is hardly a problem as the transverse ponderomotive potential is easily set to overwhelm the anti-trapping effect originating form the static voltage U_0.

The two-dimensional rf ponderomotive potential is derived using the same arguments as in the three-dimensional case (section 1). For this reason, only the main results are summarized. A potential $V_0 cos(\omega_{rf}t) + U_t$ is applied as depicted in Fig. 2.23. In order for each rod segment to have the same rf potential, each segment is capacitively coupled to its neighbor. Near the axis of the trap, the resulting potential reads

$$V_t(x,y) = \frac{\beta(V_0 cos(\Omega_{rf}t) + U_t)}{2}\left(1 + \frac{x^2 - y^2}{R^2}\right).\qquad(2.25)$$

Here β is the voltage efficiency factor for the transverse potential, and V_0 and U_t represent the rf and static transverse voltage, respectively. The rf drive frequency is denoted by Ω_{rf}, and R is the distance between the axis of the trap and the electrode. The static voltage U_t allows to break the symmetry in the strength of the x and y confinement, an important condition for effective Doppler cooling. The resulting secular frequencies are

$$\omega_{x,y} = \sqrt{\left(\frac{\beta eV_0}{\sqrt{2}m\Omega_{rf}R^2}\right)^2 - \frac{\kappa eU_0}{mz_0^2} \pm \frac{\beta eU_t}{mR^2}},\qquad(2.26)$$

where $\pm$ denotes the x, y directions, respectively.
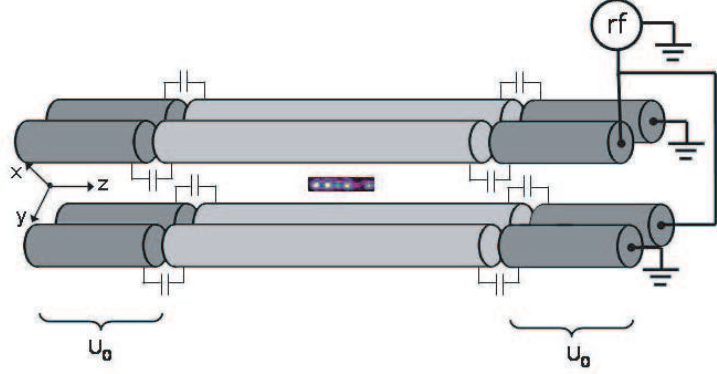
Figure 2.3: Schematic diagram of a generic linear Paul trap. A potential $V_0 cos(\omega_{rf}t) + U_t$ is applied to two opposite rods, while leaving the other two electrodes grounded, resulting in a two-dimensional quadrupole potential near the center of the trap. Each electrode segment is capacitively coupled to its neighbor, allowing the rf potential to be constant along the rod. The transverse static voltage U_t gives the ability to lift the degeneracy in ω_x and ω_y. Confinement along the z axis is realized by applying static voltages U_0 on the endcap electrodes (dark gray). Typically, in order to allow for a string of ions to be trapped, the transverse confinement is set to be significantly tighter than its longitudinal static counterpart.

Fig. 2.4 shows a schematic of the *three-layer* linear Paul used in this experiment. This three-layer design is nearly identical to the 4-rod linear trap described above, in the sense that the same expressions for the trap secular frequencies apply. The added complexity of the three-layer design is justified by two main advantages: (1) the ability to compensate for a background uniform electric field in any direction, which is more difficult with the simpler 4-rod design, and (2) an electrode structure compatible with more complicated ion trap architectures, such as T-junctions [38]. The three-layer linear trap consists of gold-coated alumina substrates vertically stacked with 125 μm alumina spacers between them, as shown in Fig. 2.4. The outer electrodes are axially segmented into three sections with appropriate static potentials applied to each for axial confinement and for compensation of background static electric fields.
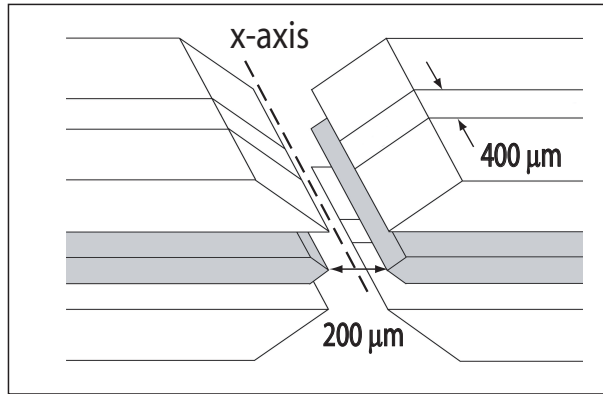
Figure 2.4: Schematic diagram of the *three-layer* linear trap used in this experiment. The rf layer (gray) is 125 μm thick, while the top and bottom segmented layers are 250 μm thick; the gold-plated alumina layers are separated by alumina spacers (not shown) with a thickness of 125 μm. The outer segments of the top and the bottom layers are separated by 400 μm. The evaporated gold coating on each electrode is approximately 0.3 μm thick.

Throughout the experiments, the longitudinal trap frequency $\omega_z/2\pi$ ranged from about 400 kHz to 4 MHz as the potential difference between the outer and the inner segments was varied from 5 V to 275 V. This potential difference was limited to 275 V in order to avoid discharges across the surface mount capacitors positioned on the trap itself (rated at 250 V). For transverse confinement, an rf potential with amplitude $V_0 \approx 400$ V with respect to the outer electrode layers is applied to the middle electrode layer, resulting in transverse trap frequencies of $\omega_x/2\pi \sim 8.1$ MHz and $\omega_y/2\pi \sim 8.3$ MHz. The degeneracy in ω_x and ω_y was lifted by applying appropriate static potentials on the inner electrodes. This also served the important function of tilting the transverse principle axis of motion, crucial for effective Doppler cooling of the ion's motion [39].

2.3 Ion trap components

So far the discussion has been limited to the rf Paul trap itself, leaving out many crucial auxiliary components that are required in order to load an ion. In the following sections I will review several important ion trap components, and in the process explain their fabrication methods (when applicable) and operational settings.

2.3.1 Atomic beam source

Producing Cd^+ ions at the center of the rf Paul trap requires the ability to (1) send a flux of neutral Cd atoms in the trapping region, and (2) efficiently ionize the neutral atoms. The Cd atomic beam is produced by an *oven*. Simply put, the oven consists of a solid source of Cd material placed inside a tube, which, when heated to a sufficiently high temperature, induces the solid Cd material to effuse through a single small opening in the direction of the trap center.

Throughout the work described in this thesis, the Cd oven design was improved significantly. In using a solid piece of Cd material, it was found that while undergoing a high temperature vacuum bake ($T \sim 225^oC$) typically lasting 2 weeks, early oven

designs would deposit a metallic layer of Cd everywhere inside the vacuum system. This gray metallic layer was especially pronounced on the surface of gold-coated linear trap electrodes. This Cd layer can cause many problems, such as degrading the trap stability [40] or even shorting out adjacent electrodes, and also become an additional source of electric field noise at the ion's position [26, 27, 18]. The solution, which is implemented in the majority of new Cd ovens, is to replace the solid Cd material (boiling point of 769°C at 1 atm) by cadmium oxide (CdO) - a powder-like substance with a boiling point of 1559°C at 1 atm. The use of CdO with its lower vapor pressure virtually eliminated the problem of cadmium coating of the electrodes during the bake. However, the significantly higher melting point of CdO required the oven to be completely redesigned. Here I briefly describe both designs.

The first oven design is very simple. It consists of a stainless steel tube with one end closed shut (pinched with pliers and spot welded) and the other end left open to let the Cd atoms effuse through. The solid piece of Cd is placed at the bottom of a tube, with inner diameter of 0.035 in., wall thickness of 0.007 in., and a typical length of $\sim$2 cm. In order to produce a Cd vapor, the temperature of the solid Cd is increased by heating the stainless steel tube with a current running along the tube, typically on the order of $\sim$1 A. The most important aspect of operating an oven is to always make sure that the current is well below its threshold value, typically a few amps for this setup. At a threshold current, the oven will, in a few minutes, deposit a visible layer of Cd on nearby surfaces - a regime that must be avoided for previously mentioned reasons. Of course, since each oven's characteristics may differ from one to the next (such as tube wall thickness etc.), testing is an important part of operating these home-made devices.

The second oven design, which incorporated the use of the CdO powder required a much higher temperature in order to produce the Cd vapor. The stainless steel tube was replaced by an alumina tube, which can sustain temperatures as high as 2000°C. A small tungsten filament with diameter 0.0025 in. is tightly wrapped around a ceramic tube, with inner diameter 0.0625 in. and wall thickness 0.035 in. The oven, packed with CdO powder, is then heated by running a current through the resistive

tungsten wire, typically under 1 A. Again, the same care must be taken in knowing the threshold current (few amps) of the particular oven in use and making sure that the operating current is always comfortably smaller.

2.3.2   Ionization of Cd

The standard method for producing positively charged trapped ions is electron bombardment, usually from electron beams having kinetic energies comfortably above the ionization threshold of the neutral Cd atom ($\sim$ 9 eV). In this experiment, this is achieved with another home-made device, the electron-gun. The source of high energy electrons is a thoriated tungsten filament resistively heated to very high temperatures by running a current through it. The high energy thermal electrons are accelerated through the hole of a metallic plate, biased at -130V, and are directed toward the center of the trapping region. The optimal electron-gun settings in our experiment consisted of a current and biased voltage large enough to produce a total collected current of $\sim$150 μA. To load an ion, the electron-gun is turned on until an ion appears on the camera, then both oven and electron-gun are simultaneously turned off. It is very costly to leave the oven and electron-gun "ON" longer than is necessary, since both tend to increase the ambient pressure in the vacuum system, leading to a shorter lifetime of the ion in the trap.

This use of an e-gun worked fine until the need for simultaneously loading multiple Cd^+ ions of a given isotope. For instance, in order to load two $^{111}Cd^+$ ions, the oven and e-gun had to be turned on and off approximately a dozen times. By the time two $^{111}Cd^+$ions are loaded, the ion trap lifetime is already reduced from several hours down to tens of minutes - making any two-ion experiments nearly impossible to carry out. For this reason and others, an alternative ionization method was implemented. It consists of using ultrafast laser pulses to photoionize the neutral Cd atoms. This method is an attractive alternative for many reasons, but mainly it avoids the use of electron filaments which corrupt the pressure and can be much more efficient than electron bombardment.

This novel ionization technique was an integral part of this work and hence it is described in great details in chapter 4 of this thesis. The photoionization technique also required the construction of a long-wavelength pulsed laser, which is described in section 4.1.3.

2.3.3 Rf voltage source

Typical trapped ion experiments demand secular frequencies on the order of a few MHz, requiring several hundred volts of rf applied to the trap electrodes. In order to achieve this, each trap electrode is attached, via a vacuum feedthrough, to the high voltage end of an rf quarter-wave *helical* coil resonator. The resonator takes the output of an rf amplifier (few watts) with 50Ω output impedance, and steps it up to a voltage as high as a few thousand volts. This voltage is typically limited by electrical discharge across the vacuum feedthrough, which are commonly rated to a few thousand volts. As many as 10 resonators were built in order to accommodate the various experiments described in this thesis. Below I describe the design and operation of a typical helical coil resonator used in this work.

In principle, a simpler *coaxial* quarter-wave resonator could be used, however the wavelengths associated with the typical rf drive frequencies in this work (20-50 MHz) are on the order of meters, making the coaxial design impractical. The helical design was first proposed in the late 50's in a series of papers by W. Macalpine and R. Schildknecht [41, 42]. This design yields a fairly compact device with a quality factor Q that can reach a thousand[6]. However, it has one drawback; the lack of symmetry makes it very difficult to calculate the electromagnetic field inside the cavity and hence predict with high accuracy the resulting Q and resonance frequency of the resonator. For this reason, the design of each resonator was based on an empirical formula, described in [41]. This formula takes as its input the desired resonance frequency, quality factor Q, and size of the resonator, and outputs a value for all resonator parameters needed to build it: the inner *coil* length, diameter, number of

---

[6]The highest quality factor observed for the various resonators in this experiment is $\sim$600

turns, wire gauge, winding pitch, and the cylindrical outer conductor's length and diameter. In designing the resonator it is important to consider the fact that the resonance frequency is typically reduced by up to a factor of two when the resonator is attached to the trap electrodes – due to the parallel capacitive impedance of the trap+feedthrough, typically around 5 pF.

Often, a trapped ion experiment requires the ability to apply a static potential U_0 to one of the trap electrode (Eq. 2.2). This is achieved by biasing parts of the resonator at the appropriate voltage. However, in order to avoid large and often crippling rf reflections, rf low-pass filters must be inserted in series between the DC voltage supply and the resonator. The low-pass filters used in this work consist of standard π-networks, typically made from $0.1\mu F$ capacitors and $100\mu H$ inductors.

An important variation in the standard quarter-wave helical coil resonator design consists of introducing a second inner coil wounded along the other coil. This type of resonator, depicted in Fig. 2.5, is typically referred to as a "bifilar" resonator. The bifilar resonator allows both rf leads going to the trap electrodes to have the same ac voltage but different bias voltages. In order to ensure that both rf leads have the same rf amplitude and phase, a shunt capacitor (typically 0.1 μF) is connected across both leads. The bifilar resonator was important in the motional heating experiment, where the ability to apply independent static voltages was used to cancel micromotion (chapter 7).

2.3.4 Vacuum technology

Trapped ion experiments must be performed in an ultra-high vacuum environment ($\sim 10^{-11}$ Torr) in order to achieve long trap lifetimes – typically ranging from a few hours to several days. The lifetime in the Cd^+ ion setup is limited mainly by inelastic collisions with background atoms and molecules. Calculations show elastic collisional rate under UHV conditions are expected to occur on the order of 1/min, which has a negligible effect on experiments that are typically conducted at a repetition rate of 100 Hz. The observed lifetime of hours indicates that the probability of an inelastic
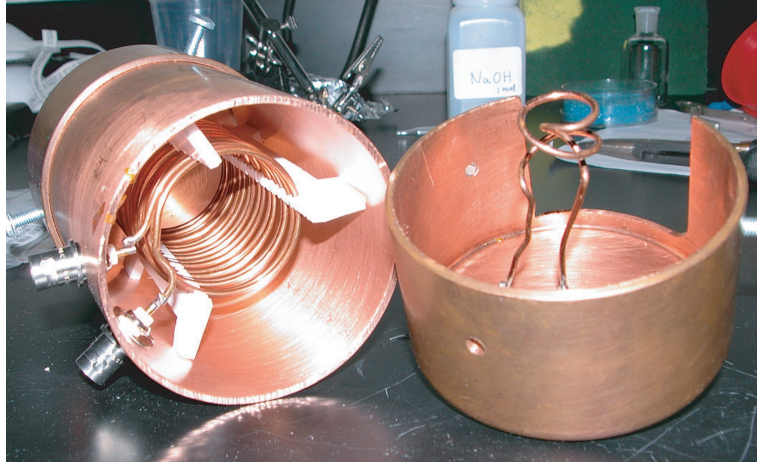
Figure 2.5: Picture of a typical quarter-wave bifilar helical coil resonator used in this work. The antenna with its characteristic pigtail shape inductively couples power from the rf amplifier into the resonator. This results in a high voltage at the other end of the coil, positioned at the center of the copper cylinder. The three pieces of white material (Teflon) around the coil serve the purpose of keeping the coil at the center of the resonator and damp any mechanical vibrations. This particular resonator was the source of high voltage for the two-needle trap. Since each needle electrode required its own particular bias voltage in order to compensate for background electric fields, a bifilar resonator was constructed. Essentially, this resonator consists of two coils which provide two identical but independent sources of rf. This bifilar resonator has a Q of $\sim$300 and a resonance frequency of $\Omega_{rf}/2\pi$=29 MHz.

collision is therefore very small.

The various vacuum systems used in this work are nearly identical to one another. They primarily consisted of standard (off the shelf) 2 3/4" UHV conflat fittings, with a few 3 3/8" fittings around the hemisphere containing the trap apparatus. An ion pump with a pumping speed of 20 l/sec was continuously turned on to keep the ambient pressure around 10^{-11} Torr. Additionally, a titanium sublimation pump was run periodically at a 60 Hz current of 45 Amps for a duration of 90 seconds. The titanium layer deposited on the surface of the vacuum system provides additional pumping. Fig. 2.6 shows the picture of a typical vacuum system used in this work[7]. Clearly visible in Fig. 2.6 are the various UV compatible fused-silica viewports attached to the hemisphere, providing the essential optical access to the trapped ion. Also attached to the hemisphere are the various electrical feedthroughs needed to power up the ion trap apparatus: high voltage rf output from the resonator, high static voltage for compensation electrodes, and high current (few amps) for the e-guns and ovens etc.

The most important step in reaching a vacuum pressure as low as 10^{-11} Torr is the *bake*. The required procedure actually consists of several successive steps. First, before assembling the trapping apparatus, each stainless steel vacuum parts is pre-baked in an oven at 400°C for a period of a few days. The oxidation layer that forms on the surface of the stainless steel is thought to help in reducing the outgassing of material trapped inside the metal. Once the whole trapping apparatus is assembled, the vacuum system is first pumped under vacuum ($\sim 10^{-6}$ Torr) with a roughing pump. The system is then placed in a large oven, where (1) the roughing pump is turned off and a large 500 L/sec ion pump is turned on, then (2) the oven temperature is slowly increased toward 225°C [8] for a duration of about 2 weeks. During this time the pressure is monitored with an ion gauge, signaling the end of the *external* bake (with the 500 l/s ion pump) and the beginning of the *internal* bake (with the 20l/s

---

[7]This particular vacuum system contained the three-layer linear trap

[8]We limit the temperature of the bake to 225°C, since the zero-length quartz-to-metal seal is rated to a maximum temperature of 250°C

ion pump) when the pressure reaches a steady state, typically around 10^{-6}-10^{-7} Torr. This internal bake proceeds for a few more days, again until the pressure reaches a steady state, usually around 10^{-7}-10^{-8} Torr. Then the temperature is slowly reduced to room temperature. This process is done slowly in order to prevent thermal stresses, especially with the viewports.

Once at room temperature, the vacuum may or may not be at the target pressure of 10^{-11} Torr. Even if it is not there yet, it is a good habit to turn on the titanium sublimation pump successively at an interval of 1 hour over the course of a day. If at the end of this step, the pressure is still above 10^{-10} Torr, this may indicate a vacuum leak.
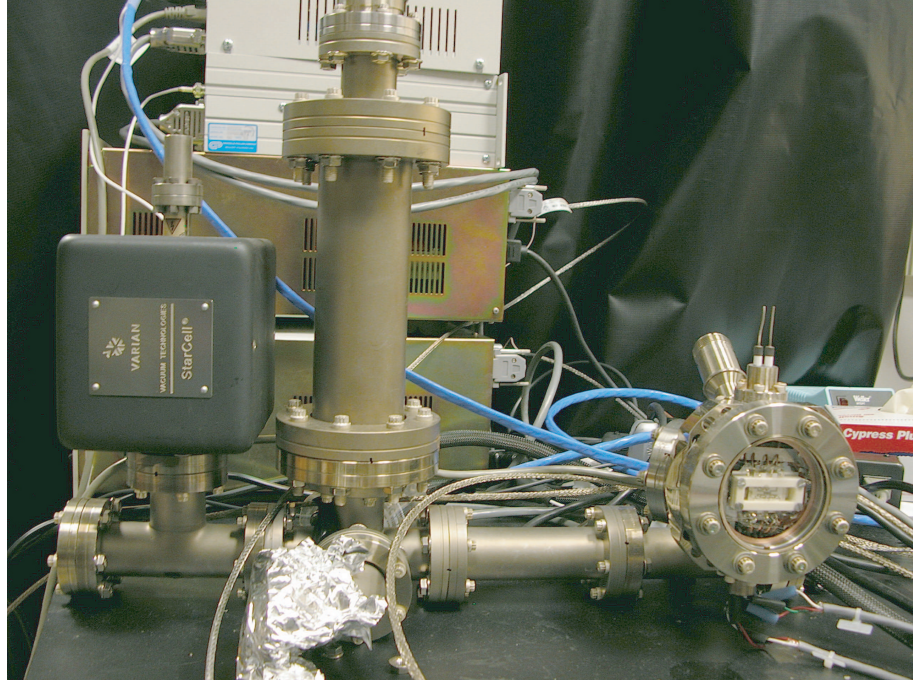
Figure 2.6: Picture of a typical vacuum system used in this work. The particular system shown here was built to hold the three-linear trap. The system is essentially built around the hemispheric chamber from Kimball Physics, which houses the ion trap along with ancillary components (ovens, e-guns, etc.). Clearly visible are several critical parts attached to the hemisphere: the UV compatible vacuum viewports, and various electrical feedthroughs. The 20 L/s ion pump (black casing) is seen slightly to the left, while the titanium sublimation pump is the vertical tube, centered in the picture.

CHAPTER 3

Energy levels of the ^{111}Cd$^+$ ion and relevant laser transitions

A trapped ^{111}Cd$^+$ ion with an energy level structure similar to the hydrogen atom is manipulated with laser light near 214.5 nm. Typical experiments described in this thesis consist of successive laser interactions, designed to transform the atomic wavefunction of the ^{111}Cd$^+$ ion in a specific way. Two types of laser manipulations are carried out, consisting of resonant interactions, and far-detuned coherent interactions. Nearly resonant light with a strongly allowed dipole transition Doppler cools the motion of the trapped ion, initializes its internal electronic state, and detects the state of the qubit. A pair of non-resonant Raman beams drive two-photon stimulated Raman transitions, which coherently couple the internal electronic levels and the motional state of the ion. This tool gives the ability to cool the ion to the ground state of motion, a crucial aspect of the work described in this thesis. More broadly, these motional sensitive Raman transitions are used to "engineer" a rich set of interaction Hamiltonians, notably the well known Jaynes-Cummings Hamiltonian of cavity QED [43, 36].

3.1 Energy levels of ^{111}Cd$^+$

The majority of atomic species chosen for a trapped ion experiment are alkali-like elements. That is, once ionized, they are left with a single unpaired valence electron. Their resulting electronic structure is then very simple and resembles that of the hydrogen atom. The cadmium atom falls within this category - the ground state of the neutral Cd atom is comprised of two valence electrons in the $5s^2$ $^1S_0$ state.

Once singly ionized, the resulting Cd^+ ion is left with a single valence electron with a hydrogen-like ground state manifold (5s $^2S_{1/2}$).

As shown in Fig. 3.1, many naturally occurring isotopes of cadmium are available. The most attractive isotopes for quantum computing applications possess a ground state hyperfine structure with a microwave frequency splitting (i.e. nonzero-nuclear spin), namely the $^{111}Cd^+$ and $^{113}Cd^+$ isotopes [44]. This work is carried out using the $^{111}Cd^+$ isotope, wich has a nuclear spin $I = 1/2$ and a natural abundance of $\sim$10%. The many naturally occuring isotopes of cadmium are expected to play an important role in the future realization of a trapped $^{111}Cd^+$ ion based quantum information processor, insofar as other isotopes having a different laser transition (i.e. isotope shift) can be used to quench the unwanted motion of the $^{111}Cd^+$ ion qubits through "sympathetic cooling" [45].

Relevant energy levels for the $^{111}Cd^+$ ion are shown in Fig. 3.2, including the $5s$ $^2S_{1/2}$ ground state and two excited P state manifolds, namely $5p$ $^2P_{1/2}$ and $5p$ $^2P_{3/2}$. The two optical transitions used in this work are $^2S_{1/2} \rightarrow {}^2P_{1/2}$ and $^2S_{1/2} \rightarrow {}^2P_{3/2}$, with a wavelength of 226 nm and 214.5 nm, respectively. Both are strongly allowed electric dipole transitions with radiative linewidth $\gamma_{1/2}/2\pi = 50$ MHz and $\gamma_{3/2}/2\pi = 60$ MHz [46]. Since the quantity $\gamma_{1/2}$ is seldom used in this thesis, and the quantity $\gamma_{3/2}$ is ubiquitous throughout, I will simply express the radiative linewidth of the $^2P_{3/2}$ level as γ_0. The fine structure splitting between the $^2P_{1/2}$ and $^2P_{3/2}$ excited states is 74 THz. The hyperfine splitting of the ground state $^2S_{1/2}$ is 14.5 GHz, while for the $^2P_{1/2}$ and $^2P_{3/2}$ states, it is $\sim$2 GHz and $\sim$800 MHz, respectively. The qubit ($|\downarrow\rangle$ and $|\downarrow\rangle$) is formed by two long-lived ground state hyperfine levels: specifically $|\downarrow\rangle \equiv {}^2S_{1/2} |F = 1, M_F = 0\rangle$ and $|\uparrow\rangle \equiv {}^2S_{1/2} |F = 0, M_F = 0\rangle$, both expressed in the total angular momentum basis $|F, M_F\rangle$. The fairly simple ground state energy level structure of the $^{111}Cd^+$ ion is indeed very convenient, as it allows the qubit to be formed by these two "clock states" (i.e. $M_F = 0$) that are first-order insensitive to magnetic field noise . The quantization z-axis is defined by an externally applied magnetic field. For this, a current of a few amps runs through a primary coil, typically providing a magnetic field of $\sim$10 Gauss at the ion's position. The magnetic field is

"trimmed" with the use of two auxiliary coils, both oriented perpendicular to the primary coil. The Zeeman splitting of the magnetic sublevels is given by $\Delta E = \mu_B g_F B_z M_F$, where μ_B=1.4 MHz/Gauss is the Bohr magneton, g_F is the Lande-g factor, B_z is the applied magnetic field, and M_F is the projection of the total angular momentum operator $\hat{F}$ along the quantization axis. For example, taking into account the different Lande-g factors for each electronic levels[1], the cycling transition[2] $^2S_{1/2} \rightarrow ^2P_{3/2}$ driven with σ^+-polarization light is frequency *blue*-shifted by an amount $\mu_B B_z$, while the cycling transition driven with σ^--polarization light is frequency *red*-shifted by an amount $\mu_B B_z$.

3.2   Resonant laser-ion interactions

Below I describe three single-photon laser processes used in large amounts throughout the work described in this thesis. They are all near-resonant with the $^2S_{1/2} \rightarrow ^2P_{3/2}$ dipole allowed transition. They form a basic set of tool required in each experiment involving a trapped ion quantum register, namely, initialization of the electronic state population, Doppler cooling the ion's harmonic motion, and detection of the qubit state.

3.2.1   Qubit state initialization: optical pumping

The beginning of each experiment described in this thesis starts with the initialization of the electronic population into a pure state, in our case $|\uparrow\rangle$. To do this, we use a standard optical pumping technique [47]. We turn on π-polarized laser light ("π-beam") near-resonant with the $S_{1/2}(F=1) \rightarrow P_{3/2}(F=1)$ transition. With spontaneous emission through the various $^2P_{3/2} \rightarrow ^2S_{1/2}$ decay channels, of which $^2P_{3/2} \rightarrow |\uparrow\rangle$ is the strongest (see Fig. 3.3), the population quickly approaches unity

---

[1]The Lande-g factors are: $g_F = 5/3$ for $P_{3/2}(F = 1)$, $g_F = 1$ for $P_{3/2}(F = 2)$, $g_F = 1$ for $S_{1/2}(F = 1)$, and $g_F = 0$ for $S_{1/2}(F = 0)$

[2]This is a closed transition, due to a single decay channel.
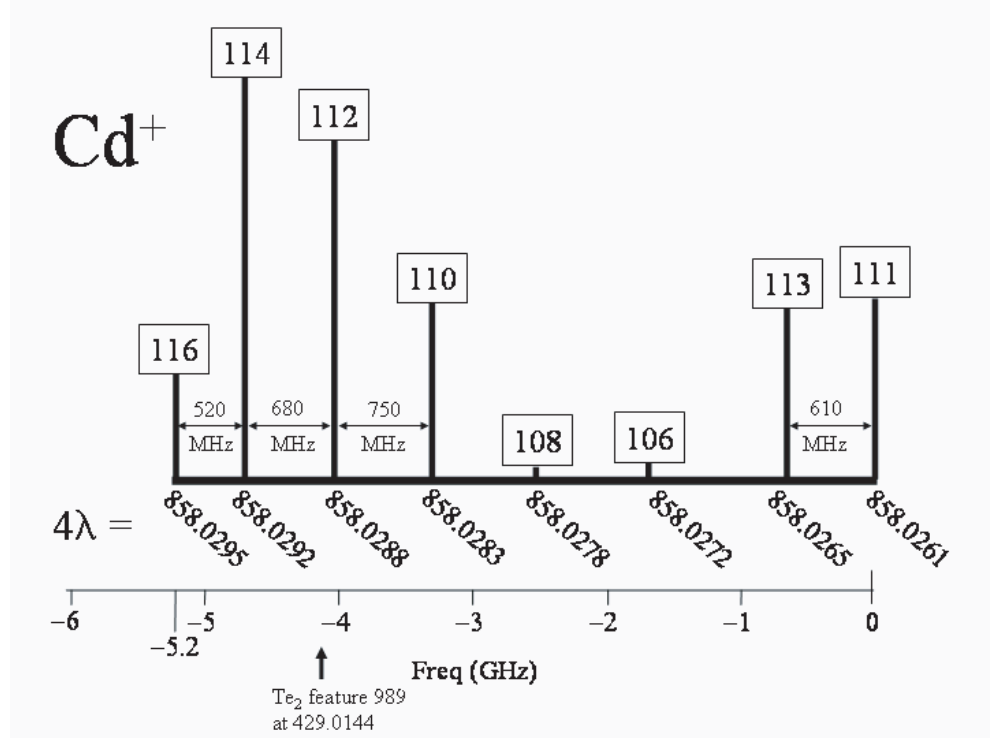
Figure 3.1: Plot showing the many isotopes of Cadmium. The relative abundance of all isotopes is plotted against the wavelength of their respective cycling transition. The wavelength shown in the plot corresponds to the output of the tunable Ti:Sapphire laser in the *infrared*, before it is frequency quadrupled to 214.5 nm, which is the wavelength required to excite the cycling transition of the Cd^+ ions. The reason for this is simply that the wavemeter used to monitor the wavelength operates in the infrared and not in the deep UV. However, the relative detunings shown on the horizontal axis and the noted frequency spacings between isotopes are in units of GHz at λ =214.5 nm. Only the $^{113}Cd^+$ and $^{111}Cd^+$ isotopes possess a ground state hyperfine structure with a microwave frequency splitting (i.e. nonzero-nuclear spin) required for quantum computation using hyperfine qubits. The ion used in this experiment (i.e. $^{111}Cd^+$), has a natural abundance of $\sim 10\%$.
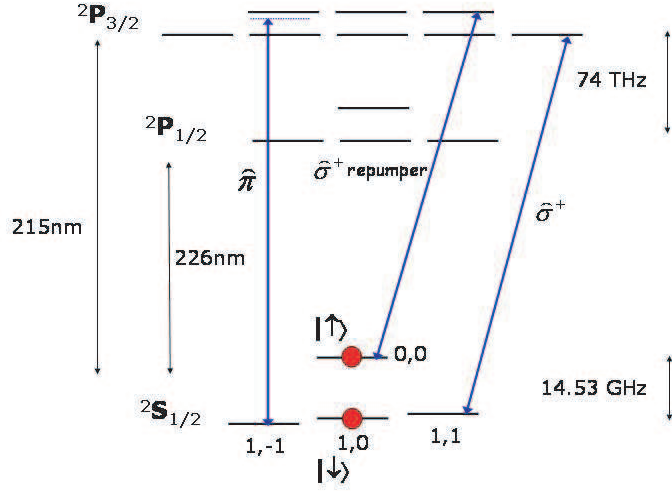
Figure 3.2: Energy level diagram of the ^{111}Cd$^+$ ion with relevant laser transitions. Every optical transition shown here couples the $^2S_{1/2}$ ground state to the $^2P_{3/2}$ excited state (radiative linewidth $\gamma_0/2\pi =60$ MHz) with a wavelength of 214.5 nm. The fine structure splitting between the excited P states is 74 THz. The hyperfine splitting of the $^2S_{1/2}$ ground state manifold is 14.5 GHz, while for the $^2P_{3/2}$ and $^2P_{1/2}$ excited state manifolds, it is $\sim$800 MHz and $\sim$2 GHz, respectively. The ground-state hyperfine levels used in the experiment are $|\downarrow\rangle \equiv |1,0\rangle$ and $|\uparrow\rangle \equiv |0,0\rangle$, both expressed in the $|F, M_F\rangle$ basis. The laser light with π-polarization couples to the $^2S_{1/2} \rightarrow ^2P_{3/2}$ transition and is used to initialize the population into the $|\uparrow\rangle$ qubit state. Both laser beams with σ^+-polarization are used to Doppler cool the ion's harmonic motion. Here, the repumper beam is turned on in order to prevent the electronic population from decaying and subsequently remaining into the $|\uparrow\rangle$ state. Detection of the qubit state is obtained with the use of the σ^+-polarized laser beam, with the repumper beam turned off. A magnetic field pointing along the z-axis (quantization axis) with a magnitude of $\sim$10 Gauss is present at the ion's position. The resulting Zeeman frequency splitting between adjacent M_F levels is $\sim$14 MHz.

in the desired qubit state, namely $|\uparrow\rangle$. In principle, a strict $S_{1/2}(F=1)\rightarrow P_{3/2}(F=1)$ transition has a *dark state*[3], which can reduce the efficiency of this state initialization step. However, this potential difficulty is removed by off-resonant coupling to the $P_{3/2}$ ($F=2$) manifold. We observed maximum efficiency for the optical pumping when the π-beam is red-detuned from the $P_{3/2}$ ($F=1$) by 200 MHz, corresponding to a blue-detuning of $\sim$600 MHz from the $P_{3/2}$ ($F=2$) manifold. We typically used a π-*beam* with $\sim$50 μW of optical power focused to a $\sim$15 μm waist; a state preparation of $\geq 99\%$ was obtained by turning on the π-beam for a time duration of 5 μsec. The performance of the optical pumping into the $|\uparrow\rangle$ state is determined using a qubit state detection technique, discussed in section 2.2.3.
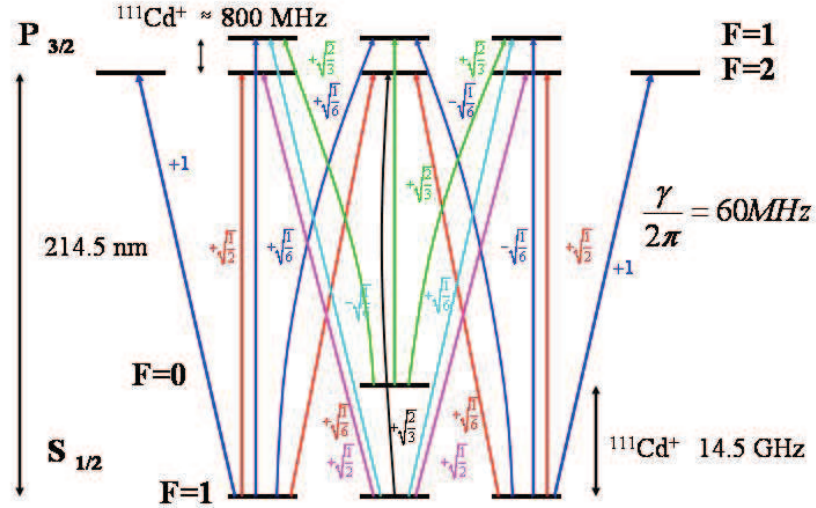
Figure 3.3: Energy level diagram of the ^{111}Cd$^+$ ion along with $^2S_{1/2}\rightarrow^2P_{3/2}$ transition amplitudes. Each amplitude is normalized to the strongest allowed transition (i.e. cycling transition).

---

[3]Stationary state with respect to the coupling

3.2.2 Doppler cooling

Another single-photon resonant process that is ubiquitous in this work is Doppler cooling of the trapped ion's harmonic motion. Here, only the type of laser interaction is presented, since the technique as a whole is described in more details in the "laser cooling" chapter of this thesis (chapter 5).

In order to achieve this, a σ^+-polarized laser beam is slightly red-detuned from the $5s\ ^2S_{1/2} \rightarrow 5p\ ^2P_{3/2}$ cycling transition ($\lambda = 214.5nm$), as shown in Fig. 3.2. Specifically, the intensity and the detuning from the excited state are set to $I \sim I_{sat}/4$ and $\Delta \sim \gamma_0/2 = 2\pi(30\text{ MHz})$, respectively - in order to obtain the most efficient Doppler cooling [36, 48]. In practice, the polarization of the laser beam isn't perfectly σ^+, and this imperfection leads to optical pumping into the $|\uparrow\rangle$ state, which essentially turns off the required photon scattering for the remainder of the cooling pulse. To prevent this, an additional laser beam ("repumper"), resonant with the $|\uparrow\rangle \rightarrow\, ^2P_{3/2}\,|1,1\rangle$ transition, is turned on with the laser beam that's resonant with the cycling transition. In the rest of this thesis, this pair of laser beams is simply referred to as "Doppler beam." In order to Doppler cool the ion's motion along the three principle axes of the ion trap, the $\vec{k}$-vector of the Doppler beam must have a component along each axis.

3.2.3 Qubit state detection

The last "step" in any experiment described in this thesis consists of detecting the state of the qubit, which is generally found in an arbitrary superposition $|\Psi\rangle = \alpha\,|\uparrow\rangle + \beta\,|\downarrow\rangle$. Simply put, the application of a *detection beam* results in the presence (or absence) of light scattering from the ion, which is correlated to the internal electronic state ($|\uparrow\rangle$ or $|\downarrow\rangle$). In repeating this measurement "step" a sufficient number of times, the probabilities $|\alpha|^2$ and $|\beta|^2$ can be determined with very high fidelity [49].

The *detection beam* is derived from the same source as the *π-beam* and the *Doppler beam*, with its optical power and frequency adjusted appropriately with the use of

an acousto-optical modulator (discussed in chapter 4). The polarization (σ^+) and frequency of the detection beam are tuned such that it *resonantly* couples to the $5s\ ^2S_{1/2}\,|1,1\rangle \rightarrow 5p\ ^2P_{3/2}\,|2,2\rangle$ cycling transition, with wavelength $\lambda = 214.5$ nm, as shown in Fig. 3.2. When the ion is in $|\downarrow\rangle$ and the detection beam is turned on, the ion repeatedly cycles between this state and the excited $^2P_{3/2}\,|2,2\rangle$ state, spontaneously emitting a photon every time. When instead the ion starts in $|\uparrow\rangle$, the *detection laser* now couples to the $|\uparrow\rangle \rightarrow 5p\ ^2P_{3/2}\,|1,1\rangle$ transition, but this time it is very far blue-detuned from it (by 14.5 GHz-0.8 GHz=13.7 GHz), resulting in very little photon scattering. Thus, by the presence (absence) of photon scattering, we can determine with almost 100% efficiency the state of the qubit. We typically refer to $|\uparrow\rangle$ as the "dark" state and $|\downarrow\rangle$ as the "bright" state, for obvious reasons. This technique offers an excellent opportunity to sharpen our intuition vis-a-vis the concept of quantum measurement. For example, lets assume that the ion starts in the equal superposition $|\Psi\rangle = \frac{1}{\sqrt{2}}\,(|\uparrow\rangle + |\downarrow\rangle)$. Immediately after the detection beam is turned on, the wavefunction randomly collapses to $|\uparrow\rangle$ or $|\downarrow\rangle$, with a 50% probability for each outcome. When the measurement is assumed to be 100% efficient, the previous example becomes equivalent to a coin toss experiment. Hence, after repeating the measurement process N times, the probability to be in either qubit state ($|\uparrow\rangle$ or $|\downarrow\rangle$) is obtained, along with "statistical" noise proportional to $\sqrt{N}$, commonly referred as *quantum projection noise* [50]. This is a fundamental source of noise, which, for uncorrelated ions (i.e. no entanglement), can only be reduced by increasing the number N of measurements.

In this work, the discrimination between $|\uparrow\rangle$ and $|\downarrow\rangle$ was typically achieved with an efficiency near 99.7%. Several factors contribute to the errors in the detection process. For instance, while detecting $|\uparrow\rangle$, the population should ideally remain in the dark state. However, there is a small probability that the population will be optically pumped from the dark state into the cycling transition (bright state), via off-resonantly coupling to the $^2P_{3/2}\,|1,1\rangle$ excited state. This off-resonant coupling constrains the intensity of the detection beam to be below saturation ($I < I_{sat}$), in order to prevent power broadening of the excited state. In fact, in the time interval

it takes to scatter a single photon while in the bright state, the probability to have a single photon scattering event from the dark state (error) is proportional to the square of the ratio of their respective detunings, that is $(\Delta_{bright}/\Delta_{dark})^2=(400$ MHz$/13.8$ GHz$)^2 = 8.4 \times 10^{-4}$. This small error makes evident a virtue of the ^{111}Cd$^+$ ion, namely its relatively large hyperfine splitting of 14.5 GHz.

In the case of the bright state detection, the error is dominated by optical pumping from the cycling transition to the dark state via off-resonant coupling to the $^2P_{3/2}(F = 1)$ excited state manifold. Ideally, this error can be made to vanish for a pure σ^+-polarization, since in this case it would not couple to the $^2P_{3/2}(F = 1)$ manifold. In order to minimize this error, we "align" the polarization of the detection beam[4] while monitoring the ion fluorescence, where the optimal polarization (maximum amounts of σ^+-polarization) corresponds to a maximum ion fluorescence.

In this work, we typically detected the state of the ion $N=100$ times. Then by binning the results according to the number of photons detected, we construct a histogram of the photon statistics for that experiment. Two such histograms are shown in Fig. 3.4 - with the top (bottom) one corresponding to the dark (bright) state. By direct inspection, we can already see that the distributions have very little overlap, implying a high detection efficiency. These histograms are accumulated with an optimal detection time and laser beam intensity of 200μs and $0.10I_{sat}$, respectively. The resulting bright state photon counts follow a Poissonian distribution, with average photon count of 12. On the other hand, the dark state histogram follows a more complicated distribution, consisting of a convolution of different bright state distributions, each occurring at different off-resonant optical pumping times [49]. The photons are collected with a photomultiplier tube (PMT), having a quantum efficiency of $\sim$20%. However, the total photon collection efficiency of the entire imaging system is approximately 0.3%, primarily limited by the small solid angle of the primary imaging lens (discussed in more detail in section 4.2).

---

[4]The polarization of the detection beam is rotated to $\hat{\sigma}^+$ by passing it through a $\lambda/4$-waveplate.
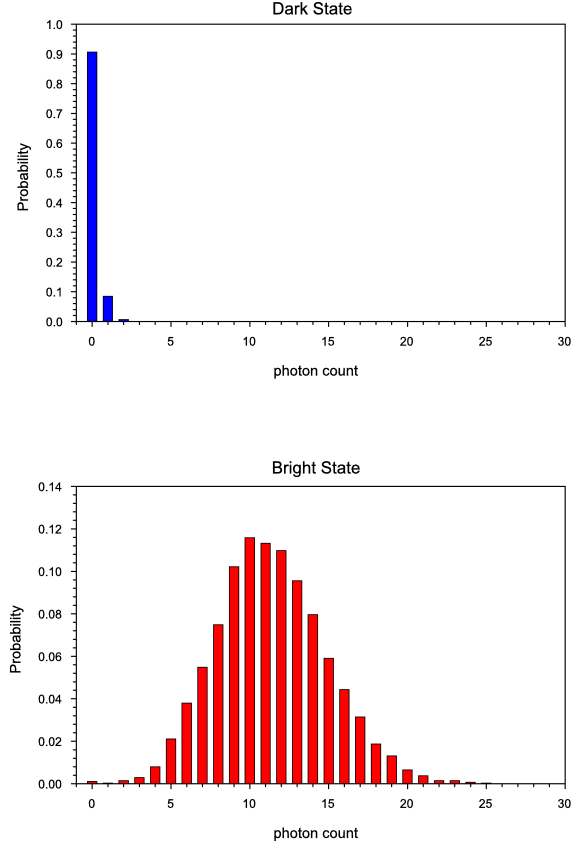
Figure 3.4: Detection histograms of the $|\uparrow\rangle$ (top) and $|\downarrow\rangle$ (bottom) states for a single $^{111}Cd^+$ ion. The bright state photon counts follow a Poissonian distribution with a mean of 12, while the dark state photon counts follow a more complicated distribution, which consists of a convolution of different bright state distributions, each occurring at different off-resonant optical pumping times. The non zero counts in the dark state distribution are mainly from light leakage onto the PMT (i.e. room lights). A discriminator threshold is set at 2 photon counts, above (below) which the ion is assumed in the bright (dark) state. This leads to a detection efficiency of 99.7%, a fairly typical condition for each experiments described in this thesis.

3.3   Coherent "laser"-ion interactions

With the appropriate application of electromagnetic fields, the internal levels of the trapped ion ($|\uparrow\rangle$ and $|\downarrow\rangle$) can be coherently manipulated, as well as coupled to the motional degree of freedom. Below I give a detailed description of the two techniques which enable the realization of these type of couplings.

3.3.1   Single-photon transitions

Every coherent interaction used in this work always involves **only** two internal levels of the ion. This two-level approximation is justified since the frequency of the electromagnetic field that provides the coupling is always near resonance of two internal levels, and the strength of the interaction (i.e. Rabi frequency) is always much smaller than the detuning to off-resonant transitions. Hence, we conveniently represent these two-level systems by the analogous spin-$\frac{1}{2}$ magnetic moment in a constant magnetic field [51, 52].

The corresponding unperturbed Hamiltonian associated with the internal levels of the ion ($|\uparrow\rangle$ and $|\downarrow\rangle$), separated in frequency by ω_0 is

$$\hat{H}_{int} = \frac{\hbar\omega_0}{2}\left(|\uparrow\rangle\langle\uparrow| - |\downarrow\rangle\langle\downarrow|\right) = \frac{\hbar\omega_0}{2}\hat{\sigma}_z \qquad (3.1)$$

where

$$\hat{\sigma}_z = \begin{pmatrix} 1 & 0 \\ 0 & -1 \end{pmatrix}, \quad |\uparrow\rangle = \begin{pmatrix} 1 \\ 0 \end{pmatrix}, \quad |\downarrow\rangle = \begin{pmatrix} 0 \\ 1 \end{pmatrix}.$$

When the external motional degree of freedom is included, the unperturbed Hamiltonian of the trapped ion takes the form

$$\hat{H}_0 = \frac{\hbar\omega_0}{2}\hat{\sigma}_z + \hbar\omega_x\hat{a}^\dagger\hat{a}. \qquad (3.2)$$

Here, only the motion along the x-axis with secular frequency ω_x is considered[5].

---

[5]In this work, only a single direction of motion is addressed by these "coherent" interactions. The generalization to more dimensions is straightforward.

When the external electromagnetic field is turned *on*, the total Hamiltonian of the system reads

$$\hat{H}_T = \hat{H}_0 + \hat{H}', \tag{3.3}$$

where $\hat{H}'$ represent the Hamiltonian provided by the applied field.

It should be noted that both types of coherent couplings used in this work, namely the magnetic dipole allowed transition and stimulated Raman transition, can be described using the same formalism, where we associate a Rabi frequency Ω, effective frequency ω, and an effective wavevector $\vec{k}$ for each transition type. This, as we will see, allows for a clear and efficient description of these different interactions.

The following derivation is meant to be general, relevant to any two-level interaction. However, for concreteness in the following derivation, we consider a magnetic dipole allowed transition, such as that inducing a transition $|\uparrow\rangle \rightarrow |\downarrow\rangle$. The perturbed Hamiltonian reads

$$\hat{H}' = -\hat{\vec{\mu}}_B \cdot \vec{B}(t), \tag{3.4}$$

where $\hat{\vec{\mu}}_B$ is the magnetic dipole moment of the two-level system, and $\vec{B}(t) = \hat{z}B_0 cos(kx - \omega t + \phi)$ is the applied time-varying magnetic field with polarization along $\hat{z}$, frequency near ω_0, and wavevector direction along $\hat{x}$. Using the spin-$\frac{1}{2}$ algebra, the z-component of the magnetic dipole moment can be rewritten as $\hat{\mu} = \mu(\hat{\sigma}_+ + \hat{\sigma}_-)$, where

$$\hat{\sigma}_+ \equiv \begin{pmatrix} 0 & 1 \\ 0 & 0 \end{pmatrix}, \quad \hat{\sigma}_- \equiv \begin{pmatrix} 0 & 0 \\ 1 & 0 \end{pmatrix}.$$

Using these results to rewrite the interaction Hamiltonian yields

$$\hat{H}' = -\frac{\mu B_0(\hat{\sigma}_+ + \hat{\sigma}_-)}{2} \left(e^{i(k\hat{x} - \omega t + \phi)} + e^{-i(k\hat{x} - \omega t + \phi)} \right). \tag{3.5}$$

At this point we transform the perturbed Hamiltonian and express it in the interaction picture. This is a very useful procedure in quantum optics as it results in a time dependent state vector only if the perturbation is turned on, otherwise the state remains stationary [52]. The transformed interaction Hamiltonian is obtained by the following similarity transformation

$$\hat{H}_{int} = U_0^\dagger \hat{H}' U_0 \tag{3.6}$$

where $U_0 \equiv e^{-i\frac{H_0}{\hbar}t}$ is the time evolution operator for the unperturbed system with Hamiltonian H_0. The interaction hamiltonian reads

$$\hat{H}_{int} = \frac{\hbar}{2}\Omega(\hat{\sigma}_+ e^{i\omega_0 t} + \hat{\sigma}_- e^{-i\omega_0 t})e^{\frac{i}{\hbar}\hat{a}^\dagger \hat{a}}\left[e^{i(k\hat{x}-\omega t+\phi)} + e^{-i(k\hat{x}-\omega t+\phi)}\right]e^{-\frac{i}{\hbar}\hat{a}^\dagger \hat{a}}. \qquad (3.7)$$

By inserting $\hat{x}=x_0(\hat{a} + \hat{a}^\dagger)$, where $x_0 = \sqrt{\frac{\hbar}{2m\omega_x}}$ is the rms spread of the wavefunction in the ground state of the harmonic oscillator, and rotating the field into the interaction frame gives

$$\hat{H}_{int} = \frac{\hbar}{2}\Omega(\hat{\sigma}_+ e^{i\omega_0 t}+\hat{\sigma}_- e^{-i\omega_0 t})\left[e^{i\eta(\hat{a}e^{-i\omega_x t}+\hat{a}^\dagger e^{i\omega_x t})}e^{-i(\omega t-\phi)} + e^{-i\eta(\hat{a}e^{-i\omega_x t}+\hat{a}^\dagger e^{i\omega_x t})}e^{i(\omega t+\phi)}\right].$$
$$(3.8)$$

In this equation, I have defined the Lamb-Dicke parameter $\eta \equiv kx_0$.

Now we have to perform the well known rotating wave approximation (RWA), with the assumption that the applied field is near resonance $\omega \approx \omega_0$. The RWA consists of neglecting the terms that oscillate at optical frequencies, on the basis that upon integration of the Schroedinger equation for time scales much longer than optical frequencies, they average to zero. Defining the detuning $\delta = \omega - \omega_0$ of the applied field from resonance, we have

$$\hat{H}_{int} = \frac{\hbar}{2}\Omega\hat{\sigma}_+ e^{i\eta(\hat{a}e^{-i\omega_x t}+\hat{a}^\dagger e^{i\omega_x t})}e^{-i(\delta t-\phi)} + h.c. \qquad (3.9)$$

Here, we are assuming that the levels have long lifetimes, which brings us in the resolved-sideband limit ($\omega_x >> \omega$). Hence, depending on the detuning δ, the interaction Hamiltonian will couple particular internal and motional states. To better see this, we expand the first exponential in a power series, yielding

$$\hat{H}_{int} = \frac{\hbar\Omega}{2}\left[\hat{\sigma}_+ \sum_{m=0}^{\infty} \frac{1}{m!}(i\eta)^m(\hat{a}e^{-i\omega_x t} + \hat{a}^\dagger e^{i\omega_x t})^m\right]e^{-i(\delta t-\phi)} + h.c. \qquad (3.10)$$

Here we can see that choosing a particular value for the detuning near the resonance of a particular transition $\delta = (n'-n)\omega_x+\Delta$, results in a **single** quasi-stationary term, with the remaining terms oscillating at frequencies that are at multiples of ω_x. Neglecting these "fast" oscillating terms is yet another iteration of the rotating wave approximation, where we now assume to be looking at time scales longer than the

trap frequency ω_x. Another way to explain this is that choosing a specific detuning δ (always assumed near resonance), selects a particular power of $\hat{a}$ and $\hat{a}^\dagger$, which then couple different motional levels together.

At this point we are ready to look at the time evolution of the two-level system's state vector, expressed in the interaction frame as

$$|\Psi\rangle = \sum_{n=0}^{\infty} \sum_{K=\uparrow,\downarrow} C_{K,n}(t)|K\rangle|n\rangle, \tag{3.11}$$

where the coefficient $C_{K,n}(t)$ acquires a time dependence only if the interaction is turned on. Solving for these coefficients using the Schroedinger equation $i\hbar|\dot{\Psi}\rangle = \hat{H}_{int}|\Psi\rangle$, yields

$$\dot{C}_{\uparrow,k} = -i^{1+|n-k|}e^{-i(\Delta t - \phi)}\Omega_{k,n}C_{\downarrow,n} \tag{3.12}$$

$$\dot{C}_{\downarrow,n} = -i^{1-|n-k|}e^{i(\Delta t - \phi)}\Omega_{n,k}C_{\uparrow,k} \tag{3.13}$$

In these equations, we define the generalized Rabi frequency as

$$\Omega_{n,k} = \Omega\langle n|e^{i\eta(\hat{a}+\hat{a}^\dagger)}|k\rangle. \tag{3.14}$$

This matrix element is the coupling strength (Rabi frequency) between the two-level system formed by $|\downarrow,n\rangle$ and $|\uparrow,k\rangle$. When evaluating this matrix element we obtain

$$\Omega_{n,k} = \Omega e^{-\eta^2/2}\sqrt{\frac{n_<!}{n_>!}}\eta^{|n-k|}L_{n_<}^{|k-n|}(\eta^2), \tag{3.15}$$

where $n_<(n_>)$ denote the smaller (larger) of n and k, and L_α^β is an associated Laguerre polynomial [53]. This expression is somewhat complicated, but it can be simplified when we are in the Lamb-Dicke limit $\eta \ll 1$, which is often satisfied in quantum computing applications. In this limit, expanding the Laguerre polynomial to lowest order in η results in $\Omega_{n,n} = \Omega$, $\Omega_{n-1,n} = \Omega\eta\sqrt{n}$, and $\Omega_{n+1,n} = \Omega\eta\sqrt{n+1}$. These are the carrier, upper sideband (blue sideband), and lower sideband (red sideband), respectively.

These first order differential equations describe Rabi oscillations between the states $|\downarrow,n\rangle$ and $|\uparrow,k\rangle$. In a matrix form, if we express the state vector as $|\Psi(t)\rangle =$

$\{C_{\uparrow,k}(t), C_{\downarrow,n}(t)\}$, the time evolution of the system $|\Psi(t)\rangle = \hat{U}_{k,n}(t)|\Psi(0)\rangle$ is governed by the time evolution operator $\hat{U}_{k,n}(t)$:

$$
\begin{pmatrix}
e^{-i\frac{\Delta}{2}t}\left[cos\left(\frac{\Omega'_{k,n}t}{2}\right) + i\frac{\Delta}{\Omega_{k,n}}sin\left(\frac{\Omega'_{k,n}t}{2}\right)\right] & -i\frac{\Omega_{k,n}}{\Omega'_{k,n}}e^{i(\phi+\frac{\pi}{2}|k-n|-\frac{\Delta}{2}t)}sin\left(\frac{\Omega'_{k,n}t}{2}\right) \\
-i\frac{\Omega_{k,n}}{\Omega'_{k,n}}e^{-i(\phi+\frac{\pi}{2}|k-n|-\frac{\Delta}{2}t)}sin\left(\frac{\Omega'_{k,n}t}{2}\right) & e^{-i\frac{\Delta}{2}t}\left[cos\left(\frac{\Omega'_{k,n}t}{2}\right) + i\frac{\Delta}{\Omega_{k,n}}sin\left(\frac{\Omega'_{k,n}t}{2}\right)\right]
\end{pmatrix},
$$
(3.16)

where we identify $\Omega'_{k,n} = \sqrt{\Delta^2 + \Omega_{k,n}^2}$. On resonance $\Delta = 0$, the expression for the time evolution simplifies to

$$
|\Psi(t)\rangle = \begin{pmatrix}
cos\left(\frac{\Omega_{k,n}t}{2}\right) & -ie^{i(\phi+\frac{\pi}{2}|k-n|)}sin\left(\frac{\Omega_{k,n}t}{2}\right) \\
-ie^{-i(\phi+\frac{\pi}{2}|k-n|)}sin\left(\frac{\Omega_{k,n}t}{2}\right) & cos\left(\frac{\Omega_{k,n}t}{2}\right)
\end{pmatrix} |\Psi(0)\rangle. \qquad (3.17)
$$

In order to better understand the meaning of this formalism, we need to see how these equations relate to a particular type of interaction. These equations imply that given a single photon transition, say a magnetic dipole allowed transition between two hyperfine levels of the Cd^+ ion, we can apply a driving field (magnetic field) to induce a coherent population transfer from $|\uparrow, k\rangle \rightarrow |\downarrow, n\rangle$. We know we can rotate a magnetic dipole with microwaves ($|\uparrow\rangle \rightarrow |\downarrow\rangle$), but if $n \neq k$, how can we change the motional state of the ion? Well, the short answer is that we cannot affect the motion of a trapped ion with such low frequency, since the momentum of individual microwave photons is too small. This conclusion is embedded in the generalized Rabi frequency $\Omega_{k,n}$, where the coupling strength critically depends on the Lamb-Dicke parameter $\eta = kx_0$. In the case of a microwave driving field (i.e. 14.5 GHz for $^{111}Cd^+$) and a trap secular frequency of $\omega_x/2\pi = 2$ MHz, the Lamb-Dicke parameter is $\eta = 5 \times 10^{-6} << 1$. Given such a small Lamb-Dicke parameter simplifies the expression for the generalized Rabi frequency to $\Omega_{k,n} = \Omega\sqrt{\frac{n_>!}{n_<!}\frac{\eta^{n-k}}{|n-k|!}}$. As expected, in the case of a small Lamb-Dicke parameter ($\eta << 1$), this coupling does not allow the driving field to couple to the ion's motion.

Having said that, it is important to note that there are physical systems, such as vibrational transitions in molecules, that are magnetic dipole allowed in the optical region of the spectrum. Hence, these one-photon magnetic dipole transitions can have a sizable Lamb-Dicke parameter and thus can drive the motion of a trapped

ion. In our case, the ^{111}Cd$^+$ ion do not have any magnetic dipole transitions[6] at optical frequencies, hence we use stimulated Raman transitions which provide the necessary field gradient (or Lamb-Dicke parameter) needed to excite the ion's motion (see detailed discussion in section 3.2.2)

The magnetic dipole transition between two hyperfine levels in the ground state of our Cd$^+$ ion was seldom used for the work described in this thesis. However, it is such a an easy/simple tool that I will briefly describe how it was implemented. Additionally, this will give the opportunity to apply the formalism (Eq. 3.16) to a simple case.

The source of the microwave field is a stable signal generator which is typically amplified to a power of 1 Watt. The amplified output is then coupled into a microwave horn, which is located 10 cm away from the trap center and oriented such that the wavevector of the magnetic field is at an angle of 45° with the $\hat{x}$-axis of the trap. The polarization of the magnetic field is mixed, such that all three possible magnetic dipole transitions in the ground state of the Cd$^+$ ion can be driven. We did observe that some magnetic dipole transitions were faster than others, presumably due to the uneven mixture of magnetic field polarization. For instance the "clock" transition $(^2S_{1/2}|0,0\rangle \rightarrow ^2S_{1/2}|1,0\rangle)$ was typically a factor of ~ 2 faster than the other two transitions $(^2S_{1/2}|0,0\rangle \rightarrow ^2S_{1/2}|1,-1\rangle$ and $^2S_{1/2}|0,0\rangle \rightarrow {}^2S_{1/2}|1,1\rangle)$. The quantization $\hat{z}$-axis is defined by applying a static magnetic field of 3.75 Gauss, producing a first order Zeeman shift of 5.75 MHz.

We can use Eq. 3.17 to infer the dynamics of this magnetic dipole transition. First we assume that the magnetic field is resonant with the transition formed by two particular ground state hyperfine levels (i.e.$\Delta = 0$). This gives the following time evolution for the state vector:

$$|\Psi(t)\rangle = \begin{pmatrix} cos\left(\frac{\Omega t}{2}\right) & -ie^{i\phi}sin(\frac{\Omega t}{2}) \\ -ie^{-i\phi}sin(\frac{\Omega t}{2}) & cos\left(\frac{\Omega t}{2}\right) \end{pmatrix} |\Psi(0)\rangle. \qquad (3.18)$$

As expected, this transformation is completely independent of the motional degree

---

[6]Indeed, there are other trapped ion research groups that use one-photon (optical) electric quadrupole transitions to excite the motion of trapped ions.

Microwave Rabi Flopping -- Clock Transition

Microwave Rabi Flopping -- Zeeman Level ($\Delta m = 1$)
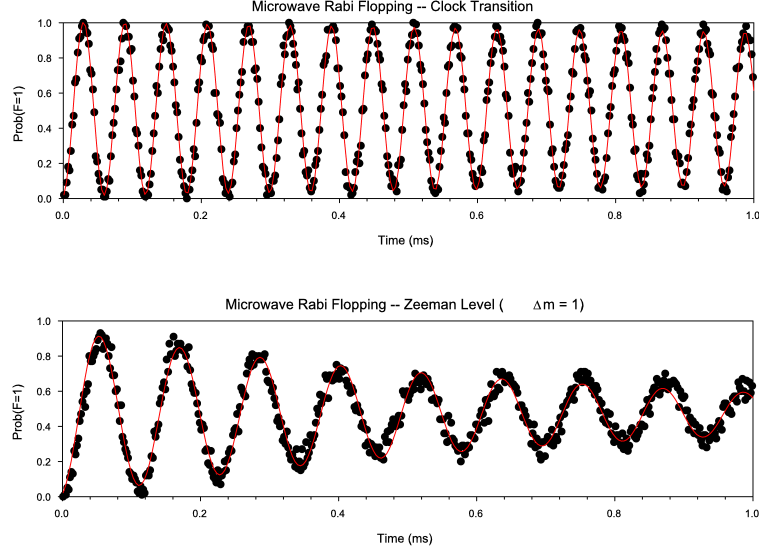
*Rabi frequency is slower for the Zeeman level transition due to the polarization of the microwave.

Figure 3.5: Rabi flopping curves showing "bright state" ($F = 1$) population occupation probability vs application time of the microwave driving field (14.5 GHz). For the top curve, the frequency of the microwave is resonant with the $^2S_{1/2}|0,0\rangle \rightarrow ^2S_{1/2}|1,0\rangle$ "clock" transition ($\Delta M_F = 1$), while for the bottom curve, the frequency of the microwave is resonant with the $^2S_{1/2}|0,0\rangle \rightarrow ^2S_{1/2}|1,1\rangle$ transition ($\Delta M_F = 1$). An static magnetic field of 3.75 Gauss is applied in order to define the quantization $\hat{z}$-axis. The resulting Zeeman shift between adjacent Zeeman levels is 5.25 MHz. The loss of contrast in the bottom curve ($\Delta M_F = 1$) is caused by ambient fluctuating magnetic fields.

of freedom. Hence the components of the state vector (amplitudes) can be rewritten accordingly as: $|\Psi(t)\rangle = \{C_\uparrow, C_\downarrow\}$. The resulting dynamics consists of oscillatory population transfer between the two levels $|\uparrow\rangle$ and $|\downarrow\rangle$, which is commonly referred to as *Rabi flopping*. It should be noted that by varying the application time of the driving field and the phase ϕ, any arbitrary qubit superposition can be achieved. Other than being intrinsically useful, this capability constitutes one of the fundamental DiVincenzo requirement to having a quantum computer [54]. Fig. 3.5 shows two such resonant ($\Delta = 0$) Rabi flopping curves. These curves are acquired by measuring the population transfer from (a) $|\uparrow\rangle \rightarrow |\downarrow\rangle$ and (b) $|\uparrow\rangle \rightarrow {}^2S_{1/2}|1, 1\rangle$, as the interaction time is increased in small increments. Prominently, the contrast of the "clock" ($\Delta M_F=0$) transition Rabi flopping is much better than its counterpart ($\Delta M_F=1$). This difference in contrast can be attributed to the ambient fluctuating magnetic field, which couples to the $\Delta M_F=1$ magnetic dipole transition more efficiently. Specifically, the magnetic field noise sensitivity of the "clock" transition in the $^{111}Cd^+$ ion is $\delta\nu = \frac{600Hz}{G^2}B\delta B$, where for the $\Delta M_F=1$ transition it is $\delta\nu = \frac{1.4MHz}{G}\delta B$. At an applied static magnetic field of 3.75 Gauss, the ratio in the sensitivities is 625. Using this ratio, we can estimate that the 1/e time for the decoherence of the clock state due to fluctuating magnetic fields should be on the order of 625 msec. For the clock transition we observed a decoherence time of $\sim$50 msec, presumably limited by phase noise in the electronics used to generate the microwave signal.

3.3.2 Two-photon stimulated Raman transitions

In this section I will describe the technique used to couple the spin and the motion of the trapped ion. This is a very important aspect of this experiment, as it gives the ability to laser cool the ion's motion to its ground state, which in turn, allows for the observation of motional decoherence (discussed in chapter 7). We already saw that a driving field which directly couples the two qubit states ($|\uparrow\rangle$ and $|\downarrow\rangle$) via a magnetic dipole transition doesn't have enough momentum to excite the motion (i.e. $\eta = kx_0 << 1$). The technique used to obtain the required high field gradient is a

two-photon stimulated Raman transition through a third, optical level as indicated in Fig 3.6. Here two laser beams couple the intermediate level $|e\rangle$ ($^2P_{3/2}$) to each qubit levels $|\uparrow\rangle$ and $|\downarrow\rangle$, where each coupling is through an electric dipole allowed transition with operators $\hat{\mu}_1$ ($|e\rangle \rightarrow |\uparrow\rangle$) and $\hat{\mu}_2$ ($|e\rangle \rightarrow |\downarrow\rangle$). Each laser beam, $\vec{E}_1(\vec{r},t) = \hat{\epsilon}_1 cos(\vec{k}_1 \cdot \vec{r} - \omega_1 t + \phi_1)$ and $\vec{E}_2(\vec{r},t) = \hat{\epsilon}_2 cos(\vec{k}_2 \cdot \vec{r} - \omega_2 t + \phi_2)$, is detuned by Δ_R from the intermediate excited state $|e\rangle$ and are assumed to have a non-copropagating geometry, where $\vec{\Delta k} = \vec{k}_2 - \vec{k}_1$. The difference frequency $\Delta\omega = \omega_2 - \omega_1 = \omega_0 + \delta\omega$ between the two Raman beams is chosen to be near the frequency splitting of the two qubit states. In order to change the motional state of the ion, the small detuning $\delta\omega$ is set to near a multiple of the trap frequency ω_x (i.e. $\delta\omega = n\omega_x - \Delta$), as depicted in Fig. 3.6.

As mentioned in the previous section, both magnetic dipole and stimulated Raman transitions can be described in a unified framework, which associates an effective driving field frequency ω, wave vector $\vec{k}$, and a Rabi frequency Ω with each of these two transition types. In the case of two-photon stimulated Raman transitions, the effective driving field frequency and wave vector are $\omega \rightarrow \omega_2 - \omega_1$ and $\vec{k} \rightarrow \vec{\Delta k}$, respectively. Thus according to Eq. 3.5, the interaction Hamiltonian becomes

$$\hat{H}' = -\frac{\hbar\Omega(\hat{\sigma}_+ + \hat{\sigma}_-)}{2} \left(e^{i(\Delta k \hat{x} - (\omega_2 - \omega_1)t + \phi)} + e^{-i(\Delta k \hat{x} - (\omega_2 - \omega_1)t + \phi)} \right). \tag{3.19}$$

Here, by having $\vec{\Delta k} \cdot \hat{\vec{x}} = \Delta k \hat{x}$, I have assumed that we are only sensitive to motion along the x-direction[7]. This interaction Hamiltonian describes an effective field with frequency $\omega = \omega_2 - \omega_1$ and wave vector Δk which *directly* couples both qubit levels ($|\uparrow\rangle$ and $|\downarrow\rangle$). The Lamb-Dicke parameter in this case becomes $\eta = \Delta k x_0$, which acquires a maximum value of $\eta = 2k_1$ when both laser beams are set in a counter-propagating geometry (here I assumed $\left|\vec{k}_2 - \vec{k}_1\right| \approx 2\left|\vec{k}_1\right|$). In this case, the resulting high field gradient is the ingredient necessary to drive the motion of the trapped ion.

Writing this effective Hamiltonian (Eq. 3.19) by replacing $\vec{k} \rightarrow \vec{\Delta k}$ and $\omega \rightarrow \omega_2 - \omega_1$ gives physical insights into this type of transition, but it still does not contain

---

[7]The experiments described in this work only require motional sensitivity along a single direction of motion.
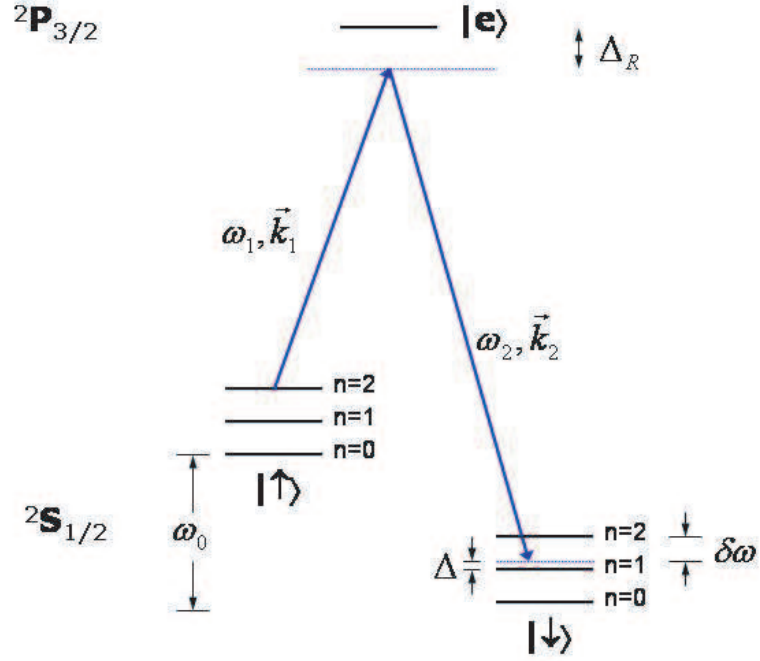
Figure 3.6: Schematic diagram relevant to the two-photon stimulated Raman transitions coupling the ground states $|\uparrow\rangle$ and $|\downarrow\rangle$. Raman laser beam 1 (2) having frequency ω_1 (ω_2) and wave vector $\vec{k}_1$ ($\vec{k}_2$), off-resonantly couples to the electric dipole transition formed by $^2S_{1/2}|\uparrow\rangle$ ($^2S_{1/2}|\downarrow\rangle$) and $^2P_{3/2}|e\rangle$. Each internal state ($|\uparrow\rangle$ and $|\downarrow\rangle$) is dressed with equally spaced (ω_x) harmonic oscillator levels corresponding to the motion of the trapped ion along the x-direction.

an expression for the Rabi frequency Ω, and also does not address the issue of optical Stark shifts experienced by each qubit state. To obtain these, we need to solve the three level problem including both qubit levels and the excited intermediate state $|e\rangle$. In the process of doing this, we will recover the effective interaction Hamiltonian (Eq. 3.19), along with expressions for the Rabi frequency and Stark shifts.

Inserting the expressions for the two driving fields into the dipole interaction Hamiltonian gives

$$
\begin{aligned}
\hat{H}_{dip} &= -\hat{\vec{\mu}} \cdot (\vec{E}_1 + \vec{E}_2) & (3.20) \\
&= -\hbar \left[g_1' e^{i(\vec{k}_1 \cdot \hat{\vec{x}} - \omega_1 t + \phi_1)} + g_2' e^{i(\vec{k}_2 \cdot \hat{\vec{x}} - \omega_2 t + \phi_2)} + h.c. \right] & (3.21)
\end{aligned}
$$

where $\hat{\vec{\mu}}$ is the atomic dipole moment operator, and $g_j' = \frac{E_j}{2\hbar} e^{i\phi_j} \hat{\epsilon}_j \cdot \hat{\vec{\mu}}$ is the jth "electric dipole" Rabi frequency (where j=1,2).

Using the same notation as in the previous section, we transform the Hamiltonian into the interaction picture. Then we insert the state vector $|\Psi(t)\rangle = \{C_{\uparrow,n}(t), C_{\downarrow,n}(t), C_{e,n}(t)\}$ in the Schrödinger equation, which gives

$$
\begin{aligned}
\dot{C}_{e,k} &= i\frac{g_1}{2} \sum_{k=0}^{\infty} e^{i[\omega_x(k-n)+\Delta_R+\delta\omega]t} \langle k| e^{i\vec{k}_1 \cdot \hat{\vec{x}}} |n\rangle C_{\uparrow,n} + & (3.22) \\
&\quad i\frac{g_2}{2} \sum_{k=0}^{\infty} e^{i[\omega_x(k-n)+\Delta_R]t} \langle k| e^{i\vec{k}_2 \cdot \hat{\vec{x}}} |n\rangle C_{\downarrow,n} \\
\dot{C}_{\uparrow,k} &= i\frac{g_1^*}{2} \sum_{k=0}^{\infty} e^{i[\omega_x(k-n)-\Delta_R-\delta\omega]t} \langle k| e^{-i\vec{k}_1 \cdot \hat{\vec{x}}} |n\rangle C_{e,n} & (3.23) \\
\dot{C}_{\downarrow,k} &= i\frac{g_2^*}{2} \sum_{k=0}^{\infty} e^{i[\omega_x(k-n)-\Delta_R]t} \langle k| e^{-i\vec{k}_2 \cdot \hat{\vec{x}}} |n\rangle C_{e,n}, & (3.24)
\end{aligned}
$$

where g_1 and g_2 are now electric dipole matrix elements connecting the excited state $|e\rangle$ to the ground states $|\uparrow\rangle$ and $|\downarrow\rangle$, respectively. Here the optical rotating wave approximation was performed to remove terms oscillating at optical frequencies. Only the x-direction of motion is considered here, which is represented by the Fock state $|n\rangle$. In order to obtain an effective two-level coupling between both ground states, the Raman beams are both far-detuned from the excited state $|e\rangle$, such that $(\Omega_{Raman}/\Delta_R \ll 1)$. Mathematically, this allows to adiabatically eliminate the excited state $|e\rangle$

from the expressions describing the dynamics (Eq. 3.22). In order to do this, we first transform into a new rotating frame via the substitution $C_{e,n} \to C'_{e,n} e^{i\Delta_R t}$, yielding

$$
\dot{C}'_{e,k} = i\frac{g_1}{2} \sum_{k=0}^{\infty} e^{i[\omega_x(k-n)+\delta\omega]t} \langle k| e^{i\vec{k}_1 \cdot \hat{\vec{x}}} |n\rangle C_{\uparrow,n} + \tag{3.25}
$$

$$
i\frac{g_2}{2} \sum_{k=0}^{\infty} e^{i[\omega_x(k-n)]t} \langle k| e^{i\vec{k}_2 \cdot \hat{\vec{x}}} |n\rangle C_{\downarrow,n} - i\Delta_R C'_{e,k}
$$

$$
\dot{C}_{\uparrow,k} = i\frac{g_1^*}{2} \sum_{k=0}^{\infty} e^{i[\omega_x(k-n)-\delta\omega]t} \langle k| e^{-i\vec{k}_1 \cdot \hat{\vec{x}}} |n\rangle C'_{e,n} \tag{3.26}
$$

$$
\dot{C}_{\downarrow,k} = i\frac{g_2^*}{2} \sum_{k=0}^{\infty} e^{i[\omega_x(k-n)]t} \langle k| e^{-i\vec{k}_2 \cdot \hat{\vec{x}}} |n\rangle C'_{e,n}. \tag{3.27}
$$

The last step in the adiabatic elimination procedure is to neglect the term $\dot{C}'_{e,k}$ in Eq. 3.27, via the assumption that $\dot{C}'_{e,k} << i\Delta C'_{e,k}$. Qualitatively, this assumption implies that the long time scale behavior of the resulting two-level system $(1/\Omega_{Raman} >> 1/\Delta_R)$, such as Rabi oscillations between $|\uparrow\rangle$ and $|\downarrow\rangle$, is not affected by fast oscillations in the excited state population. In other words, the *average* excited state population is sufficient to describe the two-level dynamics. This is not so surprising since the detuning Δ_R of both Raman beams from the excited state is always assumed to be very large, to the extent where the excited state population $\left|C'_{e,n}\right|^2$ is negligibly small at all times.

The average excited state population obtained from the adiabatic elimination reads

$$
C'_{e,k} = i\frac{g_1}{2\Delta_R} \sum_{k=0}^{\infty} e^{i[\omega_x(k-n)+\delta\omega]t} \langle k| e^{i\vec{k}_1 \cdot \hat{\vec{x}}} |n\rangle C_{\uparrow,n} + \tag{3.28}
$$

$$
i\frac{g_2}{2\Delta_R} \sum_{k=0}^{\infty} e^{i[\omega_x(k-n)]t} \langle k| e^{i\vec{k}_2 \cdot \hat{\vec{x}}} |n\rangle C_{\downarrow,n}
$$

After obtaining the average excited state population from the adiabatic elimination procedure, we plug it into Eq. 3.26 and Eq. 3.27, yielding the two-level system dynamics

$$
\dot{C}_{\uparrow,n} = i\frac{|g_1|^2}{2\Delta_R} C_{\uparrow,n} + i\frac{g_1 g_2^*}{2\Delta_R} \sum_{n'=0}^{\infty} e^{i[\omega_x(n-n')-\delta\omega]t} \langle n| e^{i\Delta k x} |n'\rangle C_{\downarrow,n'} \tag{3.29}
$$

$$
\dot{C}_{\downarrow,n} = i\frac{|g_2|^2}{2\Delta_R} C_{\downarrow,n} + i\frac{g_1^* g_2}{2\Delta_R} \sum_{n'=0}^{\infty} e^{i[\omega_x(n'-n)+\delta\omega]t} \langle n| e^{-i\Delta k x} |n'\rangle C_{\uparrow,n'}. \tag{3.30}
$$

As mentionned earlier, $\vec{\Delta k} = \vec{k}_2 - \vec{k}_1$ is aligned along the x-axis, thereby providing motional sensitivity along this direction only. We identify the first term in each equation, $\frac{|g_1|^2}{2\Delta_R}$ and $\frac{|g_2|^2}{2\Delta_R}$, as the AC Stark shift experienced by $|\uparrow\rangle$ and $|\downarrow\rangle$, respectively. If the AC Stark shifts are equal to one another, the energy separation of the qubit ω_0 remains unchanged. Their contribution can then be removed by a suitable transformation to another rotating frame, consisting of $C''_{\uparrow,n} \to C_{\uparrow,n} e^{i\frac{|g_1|^2}{2\Delta_R}t}$ and $C''_{\downarrow,n} \to C_{\downarrow,n} e^{i\frac{|g_2|^2}{2\Delta_R}t}$. However, when the AC Stark shifts are *not* the same, the qubit spacing is shifted accordingly. A frequency scan of the Raman laser beatnote $\omega = \omega_2 - \omega_1$ typically reveals such differential AC Stark shifts. A common experimental situation where this comes up is when the waist of a single Raman laser beam, say beam 1, is realigned onto the ion. The increased intensity at the ion due to Raman beam 1 results in an additional AC Stark shift to $|\uparrow\rangle$, while the AC Stark shift of $|\downarrow\rangle$ remains unchanged, thereby producing a differential AC Stark shift.

Assuming that we are in the rotating frame of the Stark-shifted resonance, and that the detuning $\delta\omega$ is chosen such that the Raman beatnote is near resonance to a particular transition $\delta\omega = \omega_x(n - n') + \Delta$, we can apply the motional rotating wave approximation which results in a single stationary term in the sum, hence a much simpler expression. The equations of motion are then

$$\dot{C}_{\uparrow,n} = -i\Omega_{n,n'}e^{-i\Delta t}C_{\downarrow,n'} \tag{3.31}$$

$$\dot{C}_{\downarrow,n} = -i\Omega_{n,n'}^*e^{i\Delta t}C_{\uparrow,n'}. \tag{3.32}$$

Here we identify $\Omega_{n,n'} = \Omega_{n',n}$ as the generalized Rabi frequency - already discussed in the context of 1-photon transitions in the previous section (Eq. 3.14). It reads

$$\Omega_{n,n'} = \frac{g_1^*g_2}{2\Delta_R}\left\langle n \left| e^{i\eta(\hat{a}+\hat{a}^\dagger)} \right| n' \right\rangle, \tag{3.33}$$

where the previous expression for the Lamb-Dicke parameter in Eq. 3.14 is modified by replacing $k \to \Delta k$, yielding $\eta = \Delta k x_0$. The only difference between this expression and the one in Eq. 3.14 is the base Rabi frequency Ω. For the case of a single-photon magnetic dipole transition, the base Rabi frequency reads $\Omega = \frac{\mu_B B}{2\hbar}$, which depends linearly on the field. Whereas in the two-photon case, the base Rabi

frequency is replaced by $\frac{g_1^* g_2}{2\Delta_R}$, which has a quadratic dependence on the field strengths - a characteristics of coherent two-photon processes.

The expressions in Eq. 3.31 are analogous to the ones in Eq. 3.14 as they both describe Rabi flopping in a two-level system. However, this time, the spin **and** motional state of the ion can simultaneously undergo a population transfer, such as $|\uparrow, n'\rangle \rightarrow |\downarrow, n\rangle$. Thus choosing a particular frequency beatnote between the two Raman beams $\omega_{n' \rightarrow n} = \omega_0 + \omega_x(n' - n)$, results in a simultaneous coupling between all pairs of levels separated in frequency by $\omega_{n' \rightarrow n}$. The coupling strength for each manifold (two-level system) is given by $\Omega_{n',n}$ and generally varies as the quantum number n increases. This feature becomes evident as multiple motional levels simultaneously undergo Rabi oscillations, each at a different Rabi frequency. Similar behavior is observed in the cavity QED system, where the motional degree of freedom is replaced by a single quantized mode of the electromagnetic field. There, "collapse" and "revival" in the Rabi flopping signal is observed, and is attributed to the interference between the superposed Rabi oscillation curves, each corresponding to different number of photons ($|n\rangle$) in the cavity [55].

In order to maximize the motional coupling (i.e. $n' \neq n$), both Raman beams must propagate in directions such that $\vec{\Delta k} = \vec{k}_2 - \vec{k}_1$ is largest. Ideally, a counterpropagating geometry would certainly achieve the objective, however the ion trap electrode structure prevents this particular arrangement. Instead we adopt a 90° noncopropagating geometry, as shown in Fig. 3.7. Both Raman beams are propagating in perpendicular directions and each is directed at an angle of 45° to the x-axis of the ion trap. The resulting wave vector difference $\left|\vec{\Delta k}\right| = \sqrt{2}k$ (assuming $\left|\vec{k}_1\right| \approx \left|\vec{k}_2\right| = k$) allows coupling to the ion's motion along the x-direction. With a Raman wavelength of $\lambda = 214.5$ nm and a ^{111}Cd$^+$ ion mass of m $= (111)1.67 \times 10^{-27}$ kg, the Lamb-Dicke parameter is $\eta = \frac{0.28}{\sqrt{\nu_x}}$, where ν_x denotes the trap frequency (MHz) along the x-axis. At a typical trap frequency of $\nu_x = 2$ MHz, the Lamb-Dicke parameter is 0.2, which gives an appreciable coupling strength for the first order sidebands (i.e. $|n' - n| = 1$).

The polarization of each Raman laser beam is constrained for two reasons: (i) the desired coupling between $|\uparrow\rangle$ and $|\downarrow\rangle$ constitutes a $\Delta M_F = 0$ transition, while
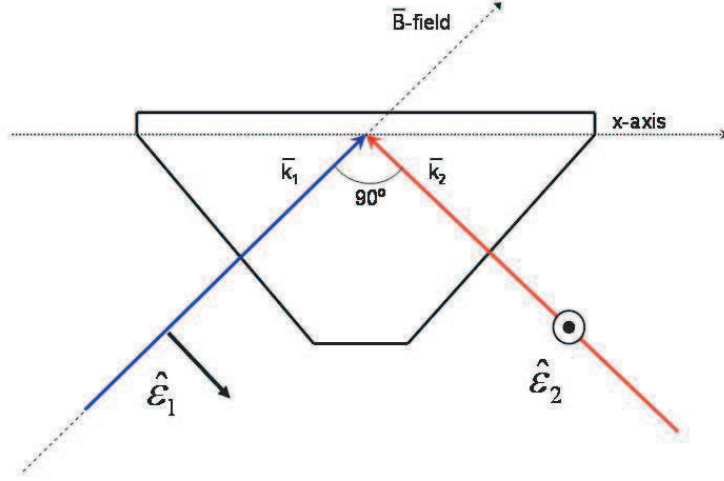
Figure 3.7: Schematic of the polarization and propagation geometry of the Raman laser beams. In order to maximize the Lamb-Dicke parameter $\eta = \Delta k x_0$, the Raman beams are each propagating at an angle of 45° with respect to the trap x-axis, and are propagating at an angle of 90° from one another. The resulting wave vector difference $\left| \Delta \vec{k} \right| = \sqrt{2} k$ is aligned parallel to the x-axis of the ion trap (assuming $\left| \vec{k}_1 \right| \approx \left| \vec{k}_2 \right| = k$). An external magnetic field $\vec{B}$ is applied in order to define the quantization axis. It is directed at an angle of 45° with respect to the x-axis of the trap. The polarization of the two Raman beams is perpendicular to each other and the quantization axis. Given the propagation geometry, this polarization arrangement achieves an optimal coupling to the excited state.
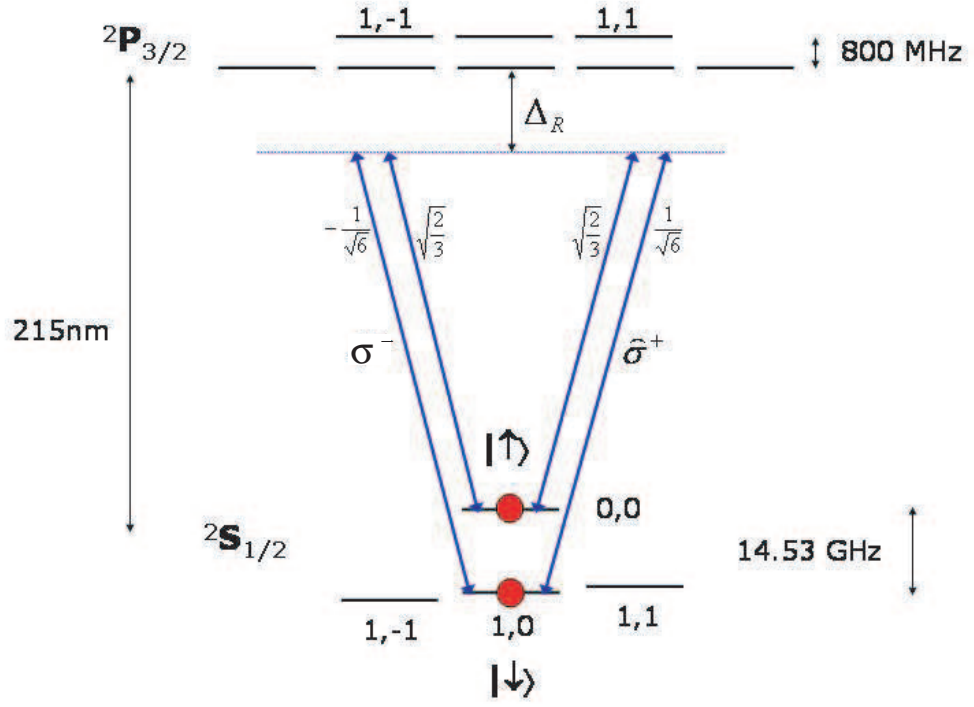
Figure 3.8: Schematic of the stimulated Raman transition paths ($\hat{\sigma}^+$ and $\hat{\sigma}^-$) along with relevant Clebsch-Gordon coefficients. Both Raman beams are linearly polarized as shown in Fig. 3.7 and are red detuned $\Delta_R/2\pi$=127 GHz from the $^2S_{1/2} \rightarrow ^2P_{3/2}$ transition. The polarization of Raman beam 1 is rotated perpendicular to that of Raman beam 2, in order to account for the π-phase shift between the $\hat{\sigma}^+$ and $\hat{\sigma}^-$ Raman transition paths.

(ii) Raman beam 1 (2) propagates in a direction that is parallel (perpendicular) to the quantization axis. The polarization arrangement of the Raman beams that yields the optimal coupling is shown in Fig. 3.7. In addition to these two constraints, the signs of the various dipole transition matrix elements (Fig. 3.3) which enter into the bare Rabi frequencies ($\frac{g_1^* g_2}{2\Delta_R}$) of both Raman transition paths ($\hat{\sigma}^+$ and $\hat{\sigma}^-$ in Fig. 3.8), require the polarization of Raman beam 1 to be rotated at an angle of 90° with respect to that of Raman beam 2, as shown in Fig. 3.7. This polarization setting, combined with the particular dipole transitions signs result in constructive interference between both Raman transition paths, as depicted in Fig. 3.8.

Some experimental data showing resonant Rabi flopping with the non-copopragating and polarization Raman beam setup discussed above is shown in Fig. 3.9. Each data set is taken at a trap frequency of $\omega_x/2\pi = 2.8$ MHz, resulting in a Lamb-Dicke parameter of $\eta = 1/6$. Before acquiring each Rabi flopping curve, the motion is prepared to its ground state ($|n = 0\rangle$), resulting in simple expressions for the Rabi frequency of the (a) carrier ($\Omega_{n,n} = \Omega$), and the (b) first lower (red) sideband ($\Omega_{n-1,n} = \eta\Omega$). For each data set, the Rabi frequency can be extracted by fitting the curve to $sin^2(\frac{\Omega t}{2})$. The expected difference in the Rabi frequency between these two transitions is clearly visible in Fig. 3.9, where the Raman beam application time required for a complete population transfer (π-pulse) is 6 times longer for a first rsb as compared to the carrier, which is consistent with a Lamb-Dicke parameter of $\eta = 1/6$.

The nature of the stimulated Raman process presented here always involves a certain amount of spontaneous emission, originating from the small population in the excited $|e\rangle$ state (Eq. 3.28). A convenient metric for this source of decoherence involves comparing the spontaneous emission rate to the Rabi flopping rate. For typical operations involving large Raman beam detunings from the excited state (i.e. $\Delta_R >> \gamma_0$), the spontaneous emission rate γ_{sp} goes as $\gamma_{sp} = s_0\gamma_0/(8\Delta_R^2)$, where s_0 denotes the saturation parameter ($s_0 = I/I_{sat}$). Comparing this spontaneous emission rate to a Raman transition rate of $s_0\gamma_0^2/\Delta_R$, yields a $\gamma_0/8\Delta_R$ probability of decay for each coherent π-pulse driven by stimulated Raman transition. With a typical detuning $\Delta_R/2\pi$=150 GHz, the probability of decay is approximately 10^{-4}. This of
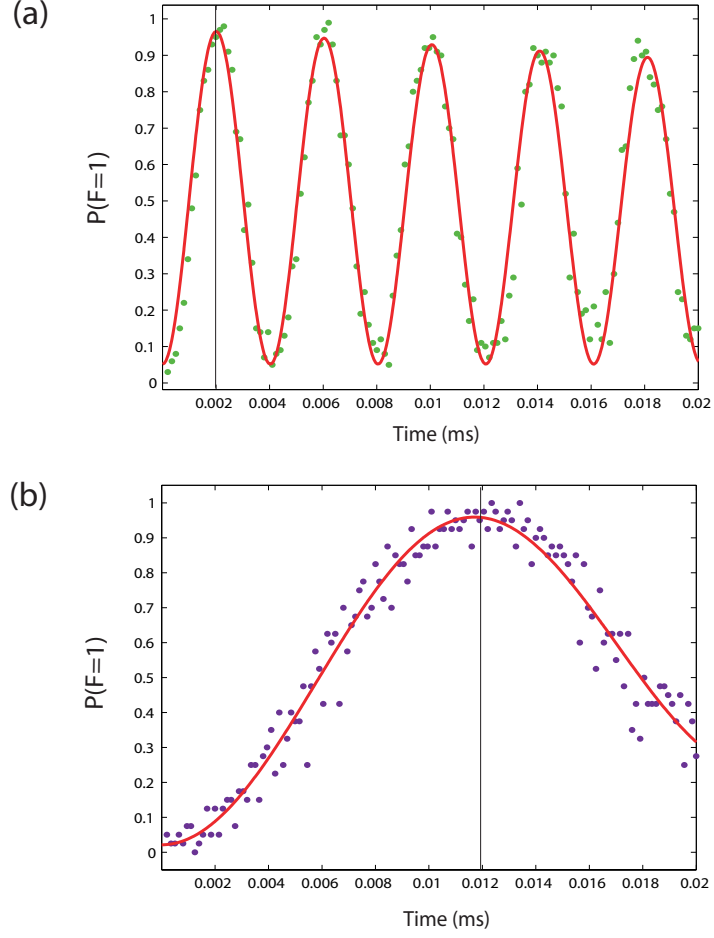
Figure 3.9: Motional sensitive (a) carrier and (b) first red sideband (rsb) Rabi flopping curves showing the ground state occupation probability $P(F = 1)$ vs application time of the Raman beams. Both Raman beams are coupled to the excited $^2P_{3/2}|F = 1, M_F = \pm 1\rangle$ states with a detuning of $\Delta_R/2\pi = 127$ GHz, while the Raman frequency beatnote ω is tuned to ω_0 and $\omega_0 - \omega_x$ in order to resonantly excite the carrier and first rsb, respectively. The trap frequency along the x-direction is $\omega_x/2\pi = 2.77$ MHz, giving a Lamb-Dicke parameter $\eta = 0.16$. For each set of data the motion is initially prepared in the the ground state $|n = 0\rangle$, yielding $\Omega_{n,n} = \Omega$ and $\Omega_{n,n+1} = \Omega\eta$ for the carrier ($|\uparrow, 0\rangle \rightarrow |\downarrow, 0\rangle$) and rsb transition ($|\uparrow, 0\rangle \rightarrow |\downarrow, 1\rangle$), respectively. The vertical gray line indicates the Raman beam application time required for a population inversion ("π-pulse"), which is factor of $1/\eta$=6 longer for the first rsb transition, as compared to the carrier.

course, is a fairly acceptable level of decoherence. However, the actual decoherence level from spontaneous emission is observed to be an order of magnitude higher. The cause of this discrepancy has not yet been understood.

In order to determine the amount of spontaneous emission present in each Rabi flopping curves, as for the ones shown in Fig. 3.9, a "spontaneous emission time scan" is performed. The qubit is initially prepared in $|\uparrow\rangle$, then the Raman beams are turned on for a time t while being off-resonantly detuned from any transition ($|\uparrow, n\rangle \rightarrow |\downarrow, n'\rangle$). The state of the qubit is then detected, yielding the amount of population that has been optically pumped from the dark state $|\uparrow\rangle$ into the bright state (F=1) via spontaneous emission. Fig. 3.10 shows a typical "spontaneous emission time scan". Here the bright state (F=1) population increases linearly showing increased optical pumping as the Raman beam application time is increased. In the time required for a π-pulse on the carrier ($\sim$12 μs, Fig. 3.10), the probability of spontaneous decay is about 5%. In order to reduce the decoherence due to spontaneous emission, the detuning Δ_R of the Raman beams can be increased further. However, for the experiment presented here, this level of spontaneous emission per Rabi cycle is already comparable to the decoherence originating from laser fluctuations (i.e. beam pointing noise).

The relatively large hyperfine splitting ($\omega_0/2\pi$ =14.53 GHz) in the ^{111}Cd$^+$ ion system is advantageous in terms of realizing near perfect detection of the qubit state [44]. However, in order to obtain two Raman beams having a 14.53 GHz frequency beatnote and relative phase stability, this large frequency splitting prevents the use of standard techniques. Typically, with a smaller hyperfine splitting such as in the ^{9}Be$^+$ (1.25 GHz) and ^{25}Mg$^+$ (1.8 GHz) ions, an acousto-optic modulator (AOM) is used to frequency shift one Raman beam with respect to the other, thus creating the phase-stable pair of Raman beams with proper frequency difference. In order to accommodate the large hyperfine splitting of the ^{111}Cd$^+$ ion, we instead modulate a single laser source with an electro-optic modulator (EOM) which produces a frequency comb with the needed high frequency spacings [56]. Below I briefly describe the "EOM setup" used to drive the stimulated Raman transitions.
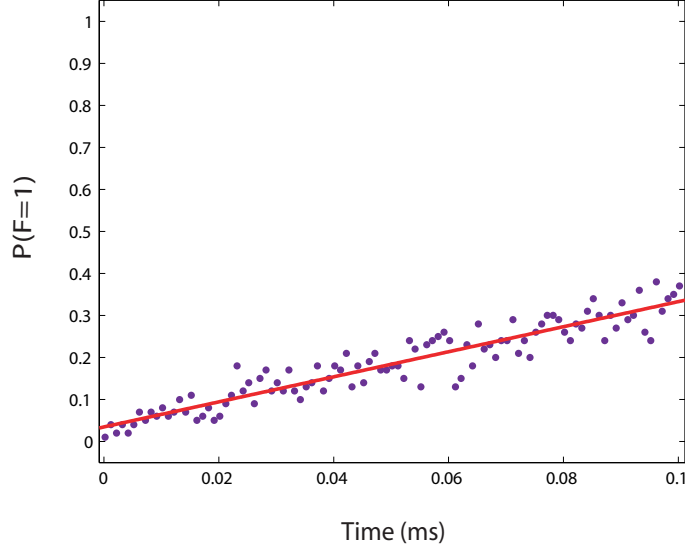
Figure 3.10: Plot of spontaneous emission vs Raman beam application time. The population is initially prepared in the dark state ($|\uparrow\rangle$), then the Raman beams are applied for a time t while being tuned off-resonance to any nearby transition (i.e. $|\uparrow, n\rangle \rightarrow |\downarrow, n'\rangle$). The population in the bright state (F=1) is then measured, yielding the amount of population that has been optically pumped from the dark state $|\uparrow\rangle$ to the bright state (F=1) via spontaneous emission. Due to the particular Raman beams polarizations (Fig. 3.8) and various transition matrix elements (Fig. 3.3), spontaneous emission is expected to produce a maximum bright state population of 2/3 as the optical pumping approaches steady state. In looking at Fig. 3.9, steady state seems to correspond to a Raman beam application time of 0.2 sec, which is much longer than any Raman pulse time involved in this experiment. This spontaneous emission time scan belongs to the same data set as the curves shown in Fig. 3.9.

Commercially available EOM's cannot operate at a short wavelength of 214.5 nm, mainly due to the lack of materials having a combined high transmissivity and high electro-optic coefficient at this wavelength. For this reason, we instead modulate a 2×214.5 nm (429 nm) laser beam at a frequency of $\omega_0' = 2\pi$ (7.265 GHz). The UV sidebands spaced by $\omega_0 = 2\pi$ (14.5 GHz) are generated by frequency-summing the laser output of the EOM in a build-up cavity containing a BBO nonlinear crystal. The free spectral range of the cavity is properly tuned to a subharmonic of the modulation frequency ($\omega_{fsr} = \omega_0'/8$ in the setup used for the experiment) such that all comb lines resonate simultaneously inside the cavity.

The electric field of the EOM output at 429 nm can be written as

$$E_{blue} = \frac{E_0}{2} e^{i(kx-\omega t)} \sum_{n=-\infty}^{\infty} J_n(\phi) e^{in[(\delta k)x - \omega_0' t/2]} + c.c., \tag{3.34}$$

where E_0 is the electric field amplitude of the EOM laser input, $J_n(\phi)$ is the n-th order Bessel function with modulation index ϕ, and δk is the wave vector difference between two adjacent sidebands spaced by a frequency $\omega_0'/2$. The resulting UV output, at a wavelength of 214.5 nm is

$$E_{UV} = \chi E_{blue} E_{blue}^* = \chi \frac{E_0^2}{4} e^{2i(kx-\omega t)} \sum_{n=-\infty}^{\infty} J_n(2\phi) e^{in[(\delta k)x - \omega_0' t/2]} + c.c., \tag{3.35}$$

where χ denotes the conversion efficiency of the frequency summing process (assumed constant over the bandwidth of the 429 nm frequency comb). The UV output is the same as the 429 nm frequency comb, but with a phase modulation of 2ϕ. All pairs of spectral components separated by 14.5 GHz produce the required beatnote to drive a stimulated Raman transition. To obtain the net bare Rabi frequency $\frac{g_1^* g_2}{2\Delta_R}$, all beatnotes at 14.5 GHz are superposed, which gives

$$\Omega = 2\Omega_0 \sum_{n=-\infty}^{\infty} J_n(2\phi) J_{n+2}(2\phi) e^{i[(2\delta k)x]} = 0. \tag{3.36}$$

This result can be justified by considering the fact that a *phase* modulated laser beam does not have an intensity beatnote at 14.5 GHz, which is required to drive a 2-photon stimulated Raman transition. In fact, the intensity of the phase modulated laser beam is constant in time.

An additional trick is used to modify the relative phases of the spectral component pairs (beatnotes), such that they no longer completely destructively interfere [56, 57]. The technique consists of splitting the UV laser beam at one location and recombine it at the ion. This essentially forms a Mach-Zehnder interferometer, where the relative length of paths A and B can be adjusted such that the total destructive interference between the beatnotes is removed. It should be noted, that the Mach-Zehnder technique arises naturally with the non-copopagating Raman beam geometry discussed earlier (Fig. 3.7), where both Raman beams are recombined at the ion with an angle of 90 degrees between them. Assuming a relative path length of Δx between arm A and B, the total field at the ion is

$$E_{UV} = \chi \frac{E_0^2}{4} e^{2i(kx-\omega t)} \sum_{n=-\infty}^{\infty} J_n(2\phi) e^{in[(\delta k)x - \omega_0' t/2]} \left\{ 1 + e^{i(2k+n\delta k)\Delta x} \right\} + c.c. \quad (3.37)$$

The resulting Rabi frequency in this case is

$$\Omega = 2\Omega_0 e^{i(\delta k)(2x + \Delta x)} \sum_{n=-\infty}^{\infty} J_n(2\phi) J_{n-2}(2\phi) cos\left[(2k + (n-1)\delta k)\Delta x\right]. \quad (3.38)$$

Here, for $\delta k \cdot \Delta x = (2m+1)\pi$, where m is an integer, the Rabi frequency can be as high as $0.48\Omega_0$ for a phase modulation of ϕ=0.764. The 0.48 prefactor multiplying the Rabi frequency can be interpreted as the efficiency factor for the Mach-Zehnder method with this particular arrangement. The optical wave vector k inside the cosine term requires the Mach-Zehnder setup to be interferometrically stable, which is very difficult to realize as the path lengths A and B are typically on the order of 1 meter. In order to eliminate this optical phase stability requirement, we introduce a frequency shift $\Delta\omega >> \Omega$ between each arm (A and B) of the Mach-Zehnder interferometer. To keep the frequency beatnotes resonant with the qubit, this shift is compensated by changing the modulation frequency of the EOM by $\pm\Delta\omega/2$, resulting in a Rabi frequency of

$$\Omega = \Omega_0 e^{i\beta} \sum_{n=-\infty}^{\infty} J_n(2\phi) J_{n-2}(2\phi) e^{in(\delta k)\Delta x} = \Omega_0 e^{i\beta} J_2\left(4\phi sin(\frac{\delta k \Delta x}{2})\right). \quad (3.39)$$

where $e^{i\beta} = e^{-i(k+2\delta k)\Delta x}$ is a phase that does not affect the magnitude of the Rabi frequency, and $\Delta\omega << \omega_0'$. Here, when the relative path length Δx is set to zero, the

Rabi frequency is zero as well, as expected since in this case the Raman frequency beatnotes do not acquire a relative phase shift. When the relative path length is instead set to $\delta k \Delta x = (2m+1)\pi$, the Rabi frequency can be as high as $0.244\Omega_0$ for a modulation index of ϕ=0.764. Fig. 3.11 shows measurements of the Rabi frequency obtained as the relative path length difference Δx is varied for two different value of the phase modulation index ϕ. The expected variations in the Rabi frequency over a path length of $\Delta x = 2\pi/\delta k$=4.13 cm is clearly visible [56]. We fit Ω to Eq. 3.39 in order to extract the modulation index ϕ for each curve. The extracted values of the modulation index ϕ is in good agreement with a direct measurement using a Fabry-Perot spectrum analyser.
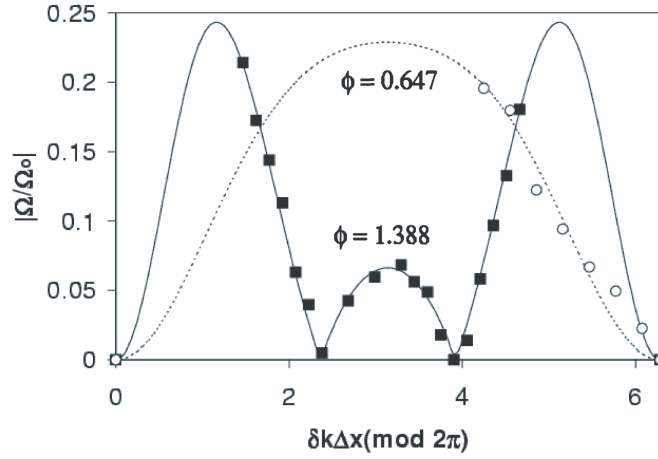
Figure 3.11: Rabi frequency vs Mach-Zehnder path length difference Δx for two different values of the modulation index ϕ. The line represent the theoretical prediction and the data are fitted to Eq. 3.39 using the vertical axis and modulation index as fitting parameters. The EOM modulation index ϕ is independently measured with a Fabry-Perot spectrum analyser, which agrees well with the fits. The vertical axis denotes the ratio to the Rabi frequency with the Mach-Zehnder setup vs the Rabi frequency if the same optical power is contained in two laser beams having a 14.5 GHz frequency beatnote. The vertical axis can be interpreted as the efficiency of the Mach-Zehnder setup.

Using this particular Raman laser beam setup yields a frequency spectrum of Raman laser-ion resonances. Typically, in order to locate the resonances, such as the carriers and the sidebands, the EOM comb spacing is kept fixed (resonant with the BBO cavity), while the AOM's located in each arms (A & B) of the Mach-Zehnder interferometer are used to change the Raman frequency beatnote to access the various resonances (discussed in section 4.2.2). Alternatively, it is also possible to observe the frequency spectrum by varying the EOM comb spacing while keeping the AOM's at a fixed frequency. This, however, is not the preferred method to observe the spectrum. As the frequency of the EOM is scanned across the various laser-ion resonances, the frequency comb spacing becomes increasingly detuned from the BBO cavity, introducing an unnecessary systematic in the data. Fig. 3.12 shows a Raman frequency spectrum obtained by varying the relative frequency of the Mach-Zehnder AOM's, while keeping the EOM drive frequency fixed. The Raman beams are applied for 8 μs between the initialization (prepared into $|\uparrow\rangle$) and detection steps. One AOM is driven at a fixed frequency of 212 MHz, while the frequency of the other (displayed on the plot's horizontal axis) is varied in order to excite the various resonances. Inspection of the Raman spectrum shows that there are twice as many resonances as one would initially guess; two carrier resonances, two first rsb resonances, etc. The reason for this stems from the relative frequency shift $\Delta\omega$ between the two arms of the Mach-Zehnder interferometer, which, as previously mentioned, was introduced in order to remove the constraint of interferometric stability of the Mach-Zehnder. For this data, the EOM is driven at a frequency of 7266.45 MHz, which gives UV spectral features that are about $2\times(1.2)$ MHz blue detuned from the qubit resonance ω_0[8]. In order to drive a carrier transition, the relative frequency of the Mach-Zehnder AOM's need to be set to $\Delta\omega=2\pi(2.4)$ MHz. Fig. 3.12 shows that when the drive frequency of the variable AOM is tune $\pm\Delta\omega=2.4$ MHz relative to the fixed AOM (212 MHz), a carrier transition is driven, in agreement with the previous statements. This frequency scan serves an important function, in that it gives the ability to preset the various rf generators to the appropriate frequencies needed to drive a particular

---

[8]Here, $\omega_0/2\pi$ denotes the Stark shifted resonance frequency of the qubit.

sequence of Raman transitions making up an experiment.

3.3.3 Sideband thermometry

The motional sideband transitions described above form the basis of many trapped ion quantum computing schemes [20, 4], where the ion motion can be viewed as an ancillary degree of freedom through which trapped ions are linked to one another, and hence entangled. An implicit requirement in these trapped ions quantum computing schemes is laser cooling of the ions motion to near the ground state, which is also based on the ability to perform motional sideband transitions. Here I present yet another common use of motional sideband transitions, which I refer to as "sideband thermometry". Essentially, this technique gives the ability to measure the average motional state population $\langle n \rangle$ for the particular case of a thermal distribution, which applies for Doppler cooling and most ground state cooling techniques since they leave the motion in a thermal state [39]. Essentially, the technique is based on the ability to observe the increased asymmetry in the k-th order blue and red sidebands as the mean motional state $\langle n \rangle$ decreases toward $|n = 0\rangle$. In the opposing limit of $n \to \infty$, the technique fails as the asymmetry in the blue and red sidebands disappears, an expected result in the classical regime. Below I give a brief description of the method.

The qubit is first prepared in $|\uparrow\rangle$, and then the k-th order blue (red) sideband is turned on for a varying time t, resulting in a population transfer between $|\uparrow, n'\rangle$ and $|\downarrow, n\rangle$. The population in the $|\downarrow\rangle$ ("bright") state is then measured, yielding

$$P_\downarrow^{rsb}(t) \;\; = \;\; \sum_{m=0}^{\infty} P_m sin^2\left(\frac{\Omega_{m,m+k}t}{2}\right) \tag{3.40}$$

$$P_\downarrow^{bsb}(t) \;\; = \;\; \sum_{m=0}^{\infty} P_m sin^2\left(\frac{\Omega_{m,m-k}t}{2}\right) \tag{3.41}$$

$$= \;\; \sum_{m'=0}^{\infty} \left(\frac{\langle n \rangle}{1 + \langle n \rangle}\right)^k P_{m'} sin^2\left(\frac{\Omega_{m',m'-k}t}{2}\right),$$

where $P_m = \left(\frac{\langle n \rangle}{1+\langle n \rangle}\right)^m \left(\frac{1}{1+\langle n \rangle}\right)$ is the occupation probability for a thermal state dis-
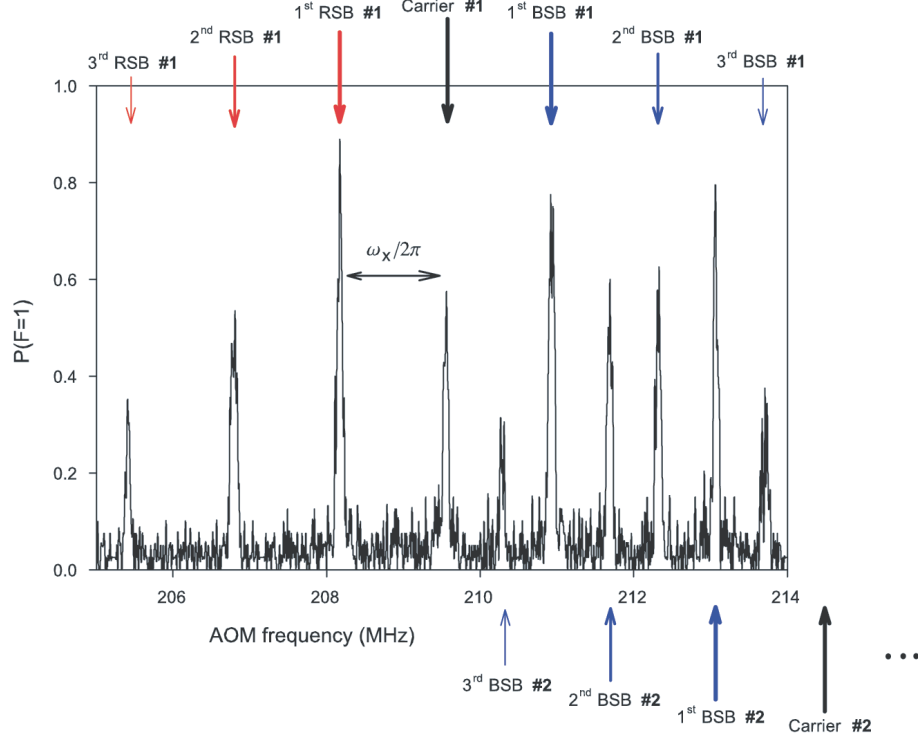
Figure 3.12: Plot of the Raman spectrum with a variable Mach-Zehnder AOM frequency. Initially, the motion is Doppler cooled and the qubit is prepared into $|\uparrow\rangle$. The Raman beams are then turned on for a fixed time duration of 8 μs with a variable beatnote frequency. The population in the bright state (F=1) is then detected and displayed on the vertical axis. The EOM is driven at a fixed frequency of 7266.45 GHz, yielding UV spectral features that are 2.4 MHz blue detuned from the qubit's Stark shifted resonance. In order to drive the two possible carrier transitions, the frequency of the variable AOM (horizontal axis of the plot) is set ± 2.4 MHz detuned from that of the fixed AOM (212 MHz). The various sidebands shown in the plot are spaced by a frequency of 1.38 MHz, corresponding to the trap frequency $\omega_x/2\pi$. The purpose of this scan is to give the ability to preset the various rf generators to the appropriate frequencies needed to drive a particular sequence of Raman transitions making up an experiment.

tribution. Using the equivalence $\Omega_{m+k,m} = \Omega_{m,m+k}$, Eq. 3.41 can be rewritten as

$$r \equiv \frac{P_\downarrow^{bsb}(t)}{P_\downarrow^{rsb}(t)} = \left(\frac{\langle n \rangle}{1 + \langle n \rangle}\right)^k. \tag{3.42}$$

The measurable asymmetry or ratio r in these probabilities is independent of the Raman application time t, carrier Rabi frequency Ω, or Lamb-Dicke parameter η [26].

Typically, the ratio r is extracted from Rabi flopping curves over each sidebands while keeping the light intensity constant and directly yields the mean occupation

$$\langle n \rangle = \frac{r^{1/k}}{1 - r^{1/k}} \tag{3.43}$$

of the thermal motional state. While Eq. 3.42 predicts a greater sensitivity when using high order sidebands ($k > 1$), the reduced strength of the high order sidebands typically leads to prohibitively noisy signals. Hence, the first order sidebands are typically chosen for the task. The sideband thermometry method presented here is one of the main tool in this experiment, as it allows us to determine the particular parameter settings required to reach the ground state of motion (chapter 6), and gives the ability to study motional decoherence from fluctuating background electric fields (chapter 7).

CHAPTER 4

Experimental setup

In this chapter I will describe the apparatus used to carry out the experiments described in this thesis. First, I will describe the different laser systems used to manipulate the motional and internal states of the trapped ion. Each laser system is characterized by an output wavelength in the deep UV - near 215nm and 229nm corresponding to the $S_{1/2} - P_{3/2}$ transition of the ^{111}Cd$^+$ ion and the $^1S_0 - ^1P_1$ transition of the neutral Cd atom, respectively. Primarily due to the deep UV requirement, each laser system is quite extensive. Hence I will present detailed schematics of how the particular laser output is generated and delivered to the trapped ion. Next, I will describe the UV imaging system used for photon counting during detection of the electronic state of the ion and also used for imaging the trapped ion. Then I will describe the experimental control and data aquisition part of the experiment.

4.1 Laser systems

In this section I describe three different laser systems used to (1) optically pump, Doppler cool, and detect the qubit state of the ^{111}Cd$^+$ ion; (2) drive stimulated Raman transitions between $|\uparrow\rangle$ and $|\downarrow\rangle$; and (3) photoionize the neutral Cd atoms via resonant coupling to their $^1S_0$-$^1P_0$ transition at a wavelength of 228.9 nm.

4.1.1 Resonant laser setup

The laser source used for the task of optical pumping, Doppler cooling, and qubit

state detection must meet several stringent requirements. It must be a tunable continuous wave (cw) laser with a center wavelength of 214.5 nm, and it must output a few mW of optical power with a linewidth under 1 MHz. The laser used for the task is depicted in Fig. 4.1. Below I give a brief description of each optical subsystems (shown in Fig. 4.1) located between the pump laser (532nm) and the three laser outputs at 214.5 nm.
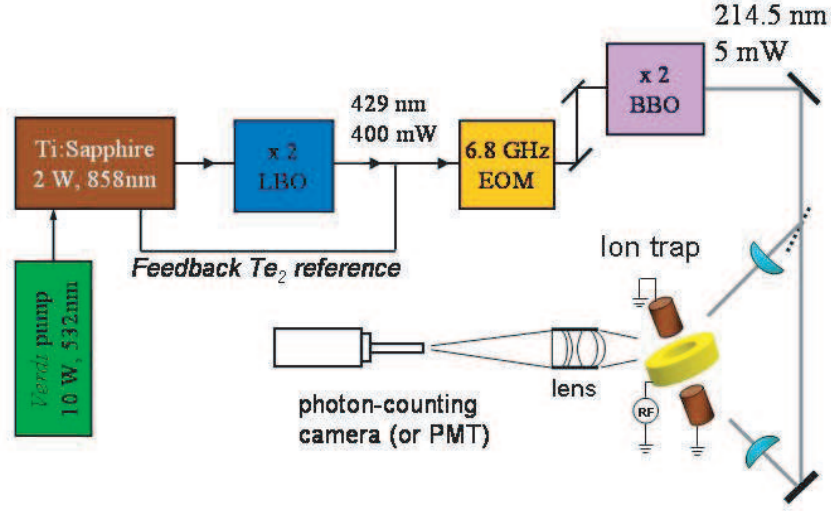
Figure 4.1: Schematic of the laser setup used to resonantly excite the $^2S_{1/2}$-$^2P_{3/2}$ cycling transition of the $^{111}Cd^+$ ion. A Ti:Sapphire laser pumped by a 10W Nd:YVO4 laser produces 1.6W of tunable infrared radiation at a wavelength of 858 nm. The infrared is frequency doubled by an LBO crystal placed inside a build-up cavity and frequency doubled once more by a BBO crystal placed inside another cavity. The tunable UV output with an optical power of 5 mW is used to drive various resonant $^2S_{1/2}$-$^2P_{3/2}$ transisitions. The output of the Ti:Sapphire laser is locked to a Te$_2$ resonance (13 MHz linewidth) producing a linewidth under 1 MHz.

The source of infrared laser light is a Coherent MBR-110 cw Ti:Sapphire laser pumped by a 10W Nd:YVO4 (Coherent) laser at 532 nm. The Ti:Sapphire produces

a $\sim$1.6 W tunable output centered at a wavelength of 214.5 nm. The tunability is obtained with two intra-cavity elements (birefringent filter and etalon) and an external reference cavity. The birefringent filter (BRF) selects optical frequencies over a 1 THz range; whereas the etalon selects optical frequencies over a smaller range ($\sim$40 GHz) with a resolution of approximately 100 MHz. The infrared output of the Ti:Sapphire is partially reflected and coupled into a temperature controlled Fabry-Perot reference cavity. The reference cavity can be tuned directly from the front panel or controlled by an external scan signal, providing tunability with a resolution of a few MHz. When the laser is locked, the reference cavity generates an error signal which is fed back to the internal laser cavity via a piezo mounted on one of the mirrors. When locked, the linewidth of the MBR-110 is well under 1 MHz which corresponds to 4 MHz in the UV. Additional Doppler-free saturated absorption spectroscopy on Te$_2$ molecules provides feedback for the reference cavity and locks the MBR-110 to within a 1 MHz bandwidth (at 214.5 nm). This small bandwidth requirement originates from the need for the various resonant lasers to remain well within the linewidth of the $^2S_{1/2}$-$^2P_{3/2}$ transition, which is $\gamma_0/2\pi = 60$ MHz.

An additional benefit of using Doppler-free saturated absorption spectroscopy as a frequency reference is that, unlike the MBR-110 reference cavity, it does not suffer from long term drifts due to temperature or mechanical vibrations. The Tellurium molecular reference (Te$_2$) is a convenient choice since it contains a strong resonance at 429 nm (13 MHz linewidth), which when frequency doubled lays approximately 3.5 GHz below the $^2S_{1/2}$-$^2P_{3/2}$ cycling transtion in the $^{111}Cd^+$ ion. At 429 nm, which is the wavelength of the Te$_2$ setup, this frequency offset corresponds to a 1.75 GHz shift, which is easily obtained with the use of a double pass 875 MHz AOM. Essentially, this setup uses the frequency dependent laser absorption within the Te$_2$ Doppler-free[1] linewidth of 13 MHz to generate an error signal which is fedback to the MBR-110, thus providing a stable reference over time scales longer than the bandwidth of the lock ($\sim$1 sec).

---

[1] In order to remove the Doppler shifts due to the high temperature vapor cell (500°C), an appropriate pump-probe beam arrangement is used.

The fine tuning of the detection laser frequency ($\leq 1MHz$) is obtained with the use of a "lock-box". The lock-box generates a variable voltage output (via a user controlled potentiometer) which is superposed onto the Te$_2$ setup error signal. The external scan input (MBR-110) accepts this error signal, which scans the cavity within a range corresponding to a scan bandwidth (typically set to 10 GHz) in the Ti:Sapphire laser.

The cw output of the Ti:Sapphire laser must be efficiently quadrupled from a wavelength of 858 nm to 214.5 nm. In order to achieve this, two Wavetrain doubling cavities (Spectra-Physics) are placed back-to-back, as shown in Fig. 4.1. The first doubling cavity converts the infrared output of the Ti:Sapphire laser to 429 nm blue light using a LBO (Lithium Triborate, LiB$_3$O$_5$) nonlinear crystal placed inside a build-up cavity. The build-up cavity is characterized by a free spectral range of 1.72 GHz and a linewidth of approximately 15 MHz, giving a finesse of ~120. The LBO cavity outputs 400 mW with an infrared input power of 1.6 W, corresponding to a conversion efficiency of ~20%. The 400 mW of blue light is sent to the next doubler, which is identical to the previous one except for the use of a BBO (beta-BaB$_2$O$_4$) nonlinear crystal instead of LBO[2], yielding an output of ~5 mW at 214.5 nm. Due to the fact that BBO crystals are hydrophilic, dry air is forced into the build-up cavity, thus preventing water vapor from being absorbed by the crystal. Additionally, the BBO crystal can be damaged (locally) by blue and UV light, requiring the crystal to be translated across the intra-cavity laser beam. Typically, the BBO crystal would require this procedure once a week[3].

When the Te$_2$ lock is engaged, the UV output of the BBO doubling cavity is set 215 MHz red detuned from the ^{2}S$_{1/2}$-^{2}P$_{3/2}$ cycling transition in the ^{111}Cd$^+$ ion. From there, three different laser beams are generated using frequency shifters (AOM's), as depicted in Fig. 4.2. The AOM's used in this experiment were purchased from Brimrose Co., each with a center frequency between 210 MHz and 400 MHz and a

---

[2]The free spectral range of the cavity had to be modified from its original setting in order to accomodate the repumper sidebands which are spaced by $4\omega_{fsr}$=(14.53-0.8)/2 GHz.

[3]There were instances where the crystal's condition remained stable for weeks.
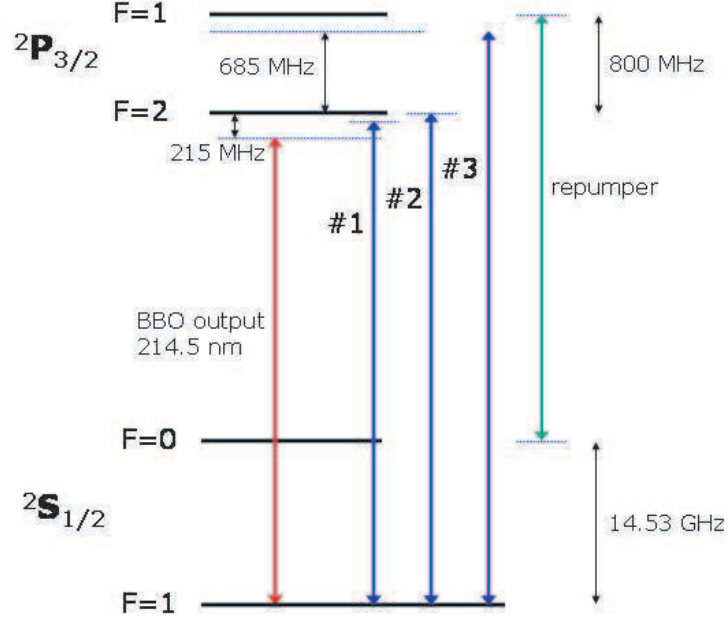
Figure 4.2: Schematic of the various laser beams used to resonantly excite the $^2S_{1/2}$-$^2P_{3/2}$ cycling transition of $^{111}Cd^+$ (detection laser). The output of the BBO doubling cavity is detuned 215 MHz below the $^2S_{1/2}$-$^2P_{3/2}$ transition. This laser beam is then subsequently split and frequency shifted in order to produce the Doppler beam (#1), Detection beam (#2), and optical pumping beam (#3). The large frequency shift of (14.5-0.8)/2 GHz required for the repumper is realized with the use of an EOM placed in front of the BBO doubling cavity.

bandwidth(3dB) of 40 MHz. The detection beam (beam #2) is obtained by frequency up-shifting the output of the BBO cavity by 215 MHz, resulting in a beam resonant with the cycling transition. The optical pumping beam (beam #3) is obtained by upshifting the output of the BBO cavity by 900 MHz. This large frequency upshift is realized by using a 450 MHz AOM in a double-pass configuration. The Doppler beam (beam #1) is a little more complex as it requires two beams with a frequency difference of 13.7 GHz (section 3.2.2): a beam red-detuned from the $^2\mathrm{S}_{1/2}$-$^2\mathrm{P}_{3/2}$ cycling transition by $\gamma_0/2 = 2\pi(30)$ MHz and a repumper beam resonant with the $^2\mathrm{S}_{1/2}|0,0\rangle \rightarrow ^2\mathrm{P}_{3/2}|1,1\rangle$ transition. In order to bridge this very large frequency spacing, the BBO doubling cavity converts the output of an EOM driven at $(13.7)/2$ GHz, resulting in a UV comb with spectral features separated by $(13.7)/2$ GHz (see section 3.3.2). Only one of these features is used as a repumper. The near resonant part of the Doppler beam is generated with the same AOM used for the detection beam, except that it is now upshifted by 185 MHz, bringing the beam at the optimal detuning for Doppler cooling.

4.1.2 Raman laser setup

The laser system used to drive the stimulated Raman transitions is nearly identical to the setup described in the previous section (Fig. 4.1). The output of a cw tunable Ti:Sapphire laser ($\sim$1.5 W) at 858.11 nm is frequency quadrupled yielding 5 mW of optical power, 150 GHz red detuned from the $^2\mathrm{S}_{1/2} - ^2\mathrm{P}_{3/2}$ transition. As previously mentioned in section 3.3.2, the large frequency beatnote between the two Raman beams required to bridge the hyperfine splitting of the $^{111}\mathrm{Cd}^+$ ion (14.5 GHz) is generated by an EOM placed in front of the BBO doubling cavity. The free spectral range of the BBO doubling cavity is tuned such that every spectral features emerging from the EOM are resonant with the Fabry-Perot build-up cavity (section 3.3.2). Fig. 4.3 shows the Mach-Zehnder interferometer consisting of two Raman beams traveling along different paths (A & B), each with a typical length of 1.5 meter. The first diffracted order of AOM 1 is directed along path A. This AOM is driven at a **fixed**
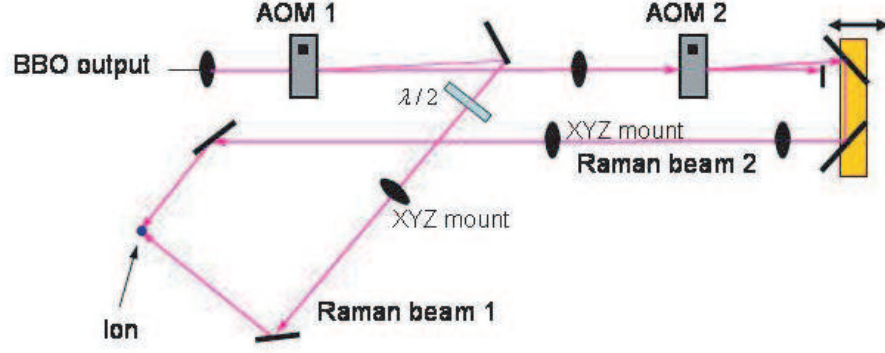
Figure 4.3: Schematic of the Mach-Zehnder interferometric setup used to carry out the motion sensitive stimulated Raman transitions. The UV output of the BBO doubling cavity passes throught two AOM's. The first diffracted order of AOM 1 is sent along path A into the trap, while the zeroth order is sent to AOM 2 with its first diffracted order also directed into the trap at an angle of 90° with respect to the other Raman beam. The first AOM is driven at a fixed frequency of 212 MHz while the second one is driven at a variable frequency near 212 MHz, allowing the Raman frequency beatnote to be tuned across the various transitions, as shown in Fig. 3.12. The UV output of the BBO cavity is typically 5 mW, giving approximately 1 mW in each Raman beam as they enter the vacuum chamber. Both Raman beams are focused onto the ion using a 10 cm focal length lens, producing a beam waist of approximately 15 μm.

rf frequency of 212 MHz, thus upshifting the frequency of the Raman beam along path A. The zeroth order output of AOM 1 is sent along path B to AOM 2 and is similarly upshifted by a variable frequency near 212 MHz, where the exact value selects a particular Raman transition, as shown in Fig. 3.12. Both Raman beams intersect the trapped ion at an angle of 90° with respect to one another. As shown on the right hand side of Fig. 4.3, the differential path length (Δx) of the Mach-Zehnder interferometer is varied by translating a retroreflector made from two 90° mirrors. This effective "corner cube" gives the ability to change Δx while keeping the Raman beams focused on the ion. The Raman beams are aligned onto the ion with collimating lenses mounted on stable XYZ mounts (LineTools), and focused onto the ion with a 10 cm lens producing a Raman beam waist of approximately 15 μm.

4.1.3   Photoionization pulsed laser setup

In this section I give a detailed description of the femtosecond pulsed laser used to photoionize the Cd atoms through an intermediate atomic resonance (discussed in chapter 5). The mode-locked Ti:Sapphire pulsed laser is characterized by an output wavelength of 916 nm with a $\leq$10 nm bandwidth[4] and 86 MHz repetition rate. The infrared pulses are frequency quadrupled to a wavelength of 228.9 nm, corresponding to the intermediate resonance of the Cd neutral atom. In order to keep the cost to a minimum, the pulsed laser was hand-built using various off-the-shelf components. The design of the oscillator is largely based on the "standard cavity" first described in [58]. However, tuning the cavity to an infrared wavelength of 916 nm requires some important and non intuitive modifications to the standard setup. Below I give a detailed description of the various components making up the long-wavelength fsec pulsed laser, shown in Fig. 4.4.

The Ti:S crystal is pumped with 5W of green light from the output of a Spectra Physics Millenia and is focused into the crystal with a 12.5 cm focal length lens (New-

---

[4]As described in chapter 5, the photoionization scheme is more efficient for longer pulse duration and thus, smaller bandwidth.
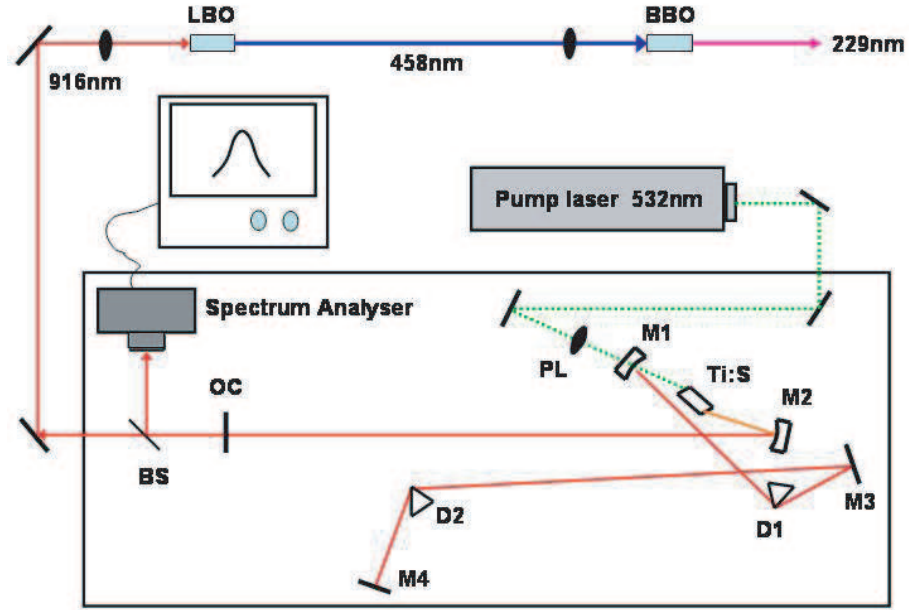
Figure 4.4: Schematic of the long-wavelength mode-locked Ti:S pulsed laser setup. The Ti:S crystal is pumped by 5W of green light (532nm) which is focused into the crystal with a 12.5 cm lens. The cavity contains five mirrors: M1 and M2 are 1/2 inch diameter curved mirrors both having a 10 cm radius of curvature and a reflectivity of $\geq 99.8\%$ (916 nm); M3 and M4 are flat 1 in. diameter mirrors with a $\geq 99\%$ reflectivity (at 916nm); and the output coupler (OC) with a 95% reflectivity at 916 nm. The fused silica prism pair are Brewster cut with an apex angle of 69.1°. In order to compensate for the dispersion aquired in passing through the crystal and both prisms, the distance separating the prisms is set to 64 cm. A small portion of the infrared output is sent to a spectrum analyser with a 1 nm resolution, giving easy measurement of the pulse bandwidth (typically 10 nm). The infrared is first frequency doubled through a 7 mm long LBO nonlinear crystal and further doubled in a 5 mm long BBO nonlinear crystal - typically yielding 10 mW at the excitation wavelength of 228.9 nm. Each nonlinear crystal is critically phased matched (angled tuned) at their corresponding wavelengths.

port Corp.). The laser has two flat end mirrors (OC and M4), two curved mirrors with 10 cm focal length (M1 and M2), and two fused silica prisms used to compensate for the group velocity dispersion (GVD). The asymmetric cavity arrangement gives a total length of 184 cm, with 65 cm in one arm of the cavity, and 119 cm in the arm containing the dispersion prism pair. The Ti:S crystal, purchased from Crystal Systems, is 5 mm long (i.e. 3x3x5mm) and has a gain coefficent of α=4.44. The 1/2 inch diameter output coupler is characterized by a 5% transmission and a reflective GVD of $-20 fs^2$ per pass at 916nm. This low transmission loss of 5% is a requirement stemming from the lower gain of the Ti:S crystal when operating at 916nm. A transmission of 20% is typically used when operating at 800nm. Both 1/2 inch diameter curved mirrors have a $\geq$ 99.8% reflection and a reflective GVD of $-50 fs^2$ at 916nm. The OC and both (M1, M2) were purchased from LayerTec in Germany with part numbers: OC (101907), M1&M2 (101241). The fused silica prism pair are Brewster cut with an apex angle of 69.1° and give a transmissive GVD of $\sim 290 fs^2/cm$. In order to compensate for the dispersion aquired in passing throught the crystal and both prisms, the distance separating the prisms is set to 64 cm. Both 1 inch diameter flat mirrors (M3 and M4) have reflectivities of $\geq$ 99% and reflective GVD of $\sim -20 fs^2$. The fused silica prisms and both flat mirrors (M1 & M2) were puchased from Newport corp. with part number: fused silica prism pair (06SB10), and M3-M4(10B20UF.20).

A typical average output power of 550 mW at 916nm is first frequency doubled throught a 7 mm long LBO nonlinear crystal and further doubled in a 5 mm long BBO nonlinear crystal - typically yielding 10 mW at the excitation wavelength of 228.8 nm. Each nonlinear crystal is critically phased matched (angled tuned) at their corresponding wavelengths. As shown in Fig. 4.4, a small portion of the infrared output is sent to a spectrum analyser with a resolution of $\sim$1nm, which allows the pulsed bandwidth, and thus pulse duration, to be determined (assuming transform-limited pulses).

As far as operating the laser, an excellent description for this type of cavity operating at 800 nm is provided in [58]. However, when operating at a far-infrared

wavelength, there are a few additional requirements. For instance, when the laser oscillates above 900nm, we observe that heating of the crystal from the pump laser prevents the laser from mode-locking. This behavior does not occur below an operating wavelength of 900nm. We find that by providing good thermal contact between the crystal and its metallic housing and water cooling the Ti:S crystal assembly completely eliminates the problem. Another important issue is that of proper choice of optical coating. It is known that care must be taken in making sure that cavity mirrors have matched coatings - both curved mirrors are especially sensitive to this requirement [59]. In fact it is very common that even if all mirrors are from the same coating run, one of them may somehow prevent mode-locking to occur - the reason for this is not well understood but nevertheless, mode-locking can be recovered by simply removing the "faulty" optics [59]. Although this last requirement is true at all wavelengths, it becomes increasingly important as the laser is tuned to the far-infrared part of the spectrum where the gain is significantly lower.

4.2   UV imaging optics

The ion fluorescence is the means by which we can (i) detect the presence of ions in the trap and (ii) measure the state of the qubit ($\alpha|\uparrow\rangle + \beta|\downarrow\rangle$) following a particular sequence of engineered laser interactions. The UV imaging system used for the task is depicted in Fig. 4.5. Simply put, the imaging system consists of two lenses with an aperture between them, with photon detection carried out with a UV sensitive imager or a photomultiplier tube (PMT). The first optical element (L1) is an objective lens (CVI, # UVO-20.0-10.0-193-248) with $f/2.1$ and focal length of 14.8 mm. An aperture with a 400 μm diameter hole is placed at the ion image produced by L1, and is used to filter out any scattered UV light that is not directly from the ion. This image is typically located at a distance of 2.6 cm in front of the second lens L2, which consists of two plano-convex singlet lenses, both having a 5 cm focal length. Lens L2 images the ion+pinhole onto the imager or PMT, typically placed $\sim$60 cm away. The magnification of the whole imaging system was usually kept near

M=250 and the diffraction efficiency typically gave a resolution of $\sim$1 μm in the ion's plane, which is small enough to distinguish two trapped ions, typically spaced by 1-3 μm for trap frequencies of 1-5 MHz [5]. The diffraction efficiency of the imaging system is strongly dependent on the distance between the ion and the objective lens L1. In fact simulations[6] show that the object distance must remain within $\pm 1/10$ mm of the optimal placement in order to have at least 85% of the optical power contained in the central spot of the Airy diffraction pattern. This optimal object distance is determined by the particular thickness of the viewport used (6.35 mm in this experiment), which is located between the ion (vacuum) and lens L1 (air) (Fig. 4.5). A reduction in the viewport thickness tends to reduce the optimal object distance. The total object distance is composed of three lengths: (A) ion-viewport distance, (B) viewport thickness, and (C) viewport-lens L1 distance. Fig. 4.6(a) shows the result of an imaging simulation for a typical arrangement with (A) 8.5 mm, (B) 6.35 mm, and (C) 2.2 mm., which yields a diffraction limited spot size at the image plane (pinhole). Fig. 4.6(b) shows the simulation results for a non-ideal arrangement of the object distances. In this case, the viewport-lens L1 distance is increased by 0.3 mm, resulting in large spherical abberations.

Two types of UV cameras were used in this experiment. The first is a single-photon imaging detector system (model 2601B) from Quantar Technology Inc., which has photon-counting capability *and* x-y position sensitivity. The camera has a circular active area of 23 mm with quantum efficiency of $\sim$1% at a wavelength of 215 nm. Over the course of several months of usage, "bleaching" spots appeared on the active area causing localized reduction in the quantum efficiency. The other imager is a Princeton instrument PI-MAX intensified CCD camera, with a 512x512 pixel array and total quantum efficiency of $\sim$20%. The PI-MAX camera was used for the majority of the work described in this thesis.

The camera is invaluable as it gives the ability to align the imaging system with

---

[5] The distance s between two trapped ions at a particular trap frequency $\omega_x/2\pi$ is given by $s = (e^2/4\pi\epsilon_0 m\omega_x^2)^{1/3}$, where e and m are the ion's electric charge and mass, respectively.

[6] The simulations are carried out in the optical design software Oslo

respect to the trap electrodes and thereby allows one to "see" the loaded ions. We used a Hamamatsu H6240-01 PMT with a quantum efficiency of ∼20%. The output of the PMT consists of TTL pulses with a 35 ns resolution. When the ion's fluorescence is saturated, giving a scattering rate of $\gamma_0/2 = 2\pi(30MHz)$, the overall detection efficiency of the system (∼0.3%) gives a photon count rate of 650 KHz.
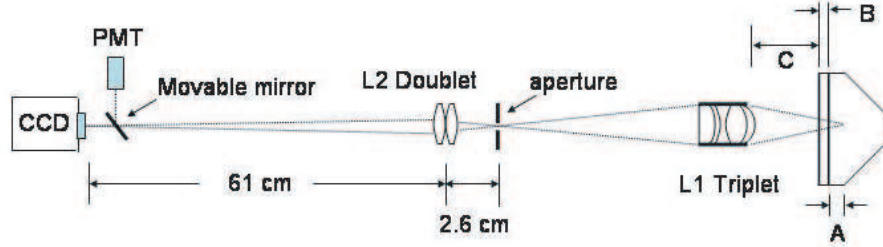
Figure 4.5: Schematic of the UV imaging system. The objective lens L1 is a triplet (CVI) with $f/2.1$ and focal distance of 14.8 mm. Lens L2 is a doublet made from two plano-convex lenses, both with a 5 cm focal lengths. The overall magnification of the system was typically kept near $M = 250$. The object distance of the objective lens L1 is composed of three lenghts: (A) ion-viewport distance, (B) viewport thickness (6.35 mm), and (C) viewport-L1 distance. To achieve a diffraction limited image, the total object distance has to be 17±0.1 mm.

4.3   Experimental control and data aquisition

In the course of a particular experiment with typical time duration of a few msec, a series of up to a hundred TTL pulses are sent to various RF switches which, depending on their logic state, turn on(off) various laser interactions by allowing(blocking) rf signals from driving certain optical modulators (AOM's and EOM's). A computer running a LabView program is used to control the whole experiment. It gives the ability to initialize the output frequencies of each rf generators, store a particular sequence of TTL pulses making up a particular experiment, execute and deliver the
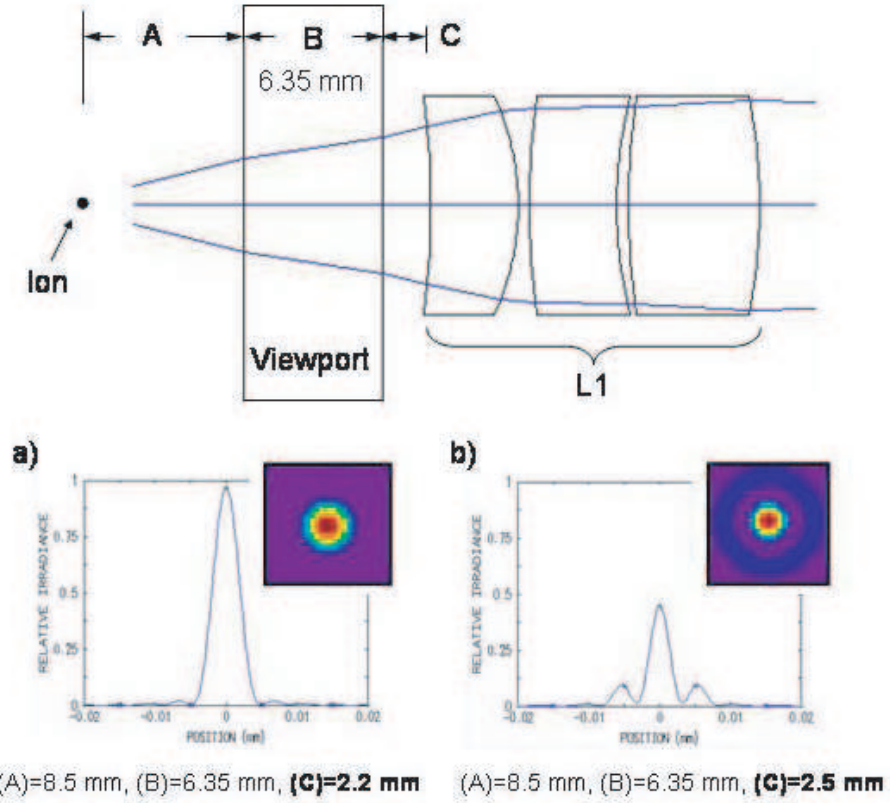
Figure 4.6: Imaging simulations of the objective lens L1 showing the image spot size with (a) an optimal object distance of 17 mm, and (b) an increased object distance of 17.3 mm. The result in (b) clearly shows the severe spherical abberations that distort the otherwise diffraction limited spot size shown in (a). In order to have at least 85% of the optical power in the central spot, the object distance must be 17±0.1 mm. For a smaller viewport thickness, the object distance must be reduced in order to maintain a diffraction limited spot size.

sequence of TTL pulses according to a preset schedule, collect and store data coming from the experimental apparatus (i.e. photon counts), and finally display the experimental results through a graphical interface.

Specifically, a National Instrument PCI "pulser" card (6534) is the source of the TTL pulses, and its 32-bit TTL signal output is the logical control sent to the various rf switches. Each rf switch typically connects a single rf generator to a particular optical modulator in the experiment. However, several optical modulators such as the detection AOM and the variable Mach-Zehnder AOM require fast switching between several rf input signals having different frequencies. In this case, the rf switches are used as de-multiplexers, where the TTL logic signal determines which rf input is sent to the particular AOM. The rf switches (Mini Circuit ZFSWA-2-46) with an in-out rf isolation of 30 dB (Typ.), did not lead to any observed optical power leakage through the AOM's when the rf input is off. In order to drive the various AOM's, each rf switch output was typically amplified to ∼1 W (and 2W for some AOMs).

A National Instrument 6602 PCI counter card is used to gather the photon counts from the PMT during the qubit state detection procedure. During the detection time, a gate pulse from the pulser card (6534) is used to arm/disarm the PCI counter in order to filter out the photon counts that occured outside of the detection window. In order to avoid dead time from downloading the counter card (photon counts) at each detection event, the photon counts are stored in a buffer on the counter card. When the data is ready to be analyzed, the content of the counter card is downloaded by the LabView software. The photon count data is first converted into a histogram, and then properties such as average photon counts and standard deviation are displayed in various forms.

Before each experiment, the particular sequence of pulses is preset and stored in the memory of the 6534 pulser card. Each experiment is composed of various "chapters", whose lengths can be scanned or delayed appropriately. At the start of every chapter, a specific set of 32-bit signals is sent out allowing several AOM's and EOM's to be turned on simultaneously. For example, in the Doppler cooling chapter, the repumper EOM and the detection AOM are turned on simultaneously. Typically,
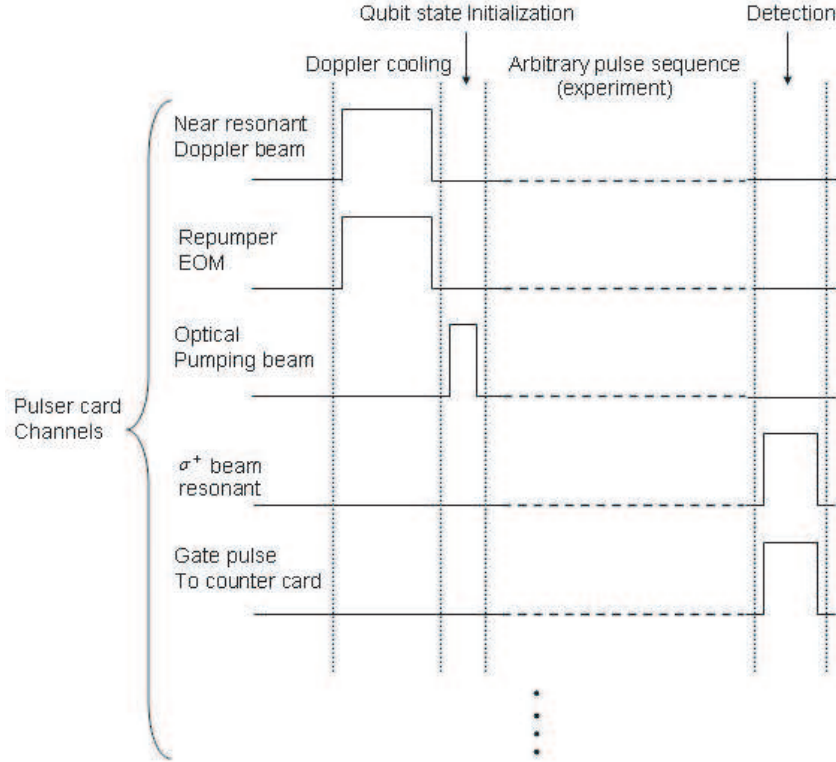
Figure 4.7: Pulser card output for a typical experiment. The pulse sequence reads from left to right. First the motion of the ion is Doppler cooled for 1 msec and then the qubit is prepared in $|\uparrow\rangle$ by applying the optical pumping beam (π-beam) for 5 μs. The "experiment" is composed of a pulse sequence tailored for a specific outcome (i.e. Raman laser cooling). The last pulse always involves the qubit detection, typically on for 200 μs. Each line show the TTL pulses that are used to control the state of the rf switches.

each experiment consisted of four distinct parts: (i) Doppler cooling pulse is turned on for 1 msec, (ii) qubit state initialization where the optical pumping beam is turned on for ∼5 μs, (iii) particular set of chapters making up a specific experiment (i.e. Raman cooling), and (iv) qubit state detection step where the detection beam and photon counter are pulsed for 200 μs. Fig. 4.7 depicts the timing for a general pulse sequence. Here, for simplicity, only 5 channels out of the 32-bit signal are shown. Each channel carries timed TTL pulses to turn on/off the rf switches to which they are assigned. Each vertical dotted line denotes the start of a new chapter, which as previously mentioned, can be delayed or scanned appropriately.

In taking data, the experiment is usually repeated many times while a particular parameter is progressively changed. The experiment thus consists of two time scales: a msec time scale where all parameters in each chapters are fixed as the sequence of pulses is executed **once**, and a ∼500 msec time scale corresponding to the number of times the pulse sequence is repeated (typically 100 times[7]). Repeating the experiment many times in succession is important as it reduces the fundamental and technical noises associated with the data. For example, while performing a frequency scan as shown in Fig. 3.12, the frequency of the variable Mach-Zehnder AOM is initially set to 205 MHz. Using this fixed AOM frequency for the Raman chapter, along with the particular settings of the other chapters, the experiment is repeated 100 times, lasting approximately 500 msec. The photon counts are analysed and displayed as a single point on the AOM frequency scan shown in Fig. 3.12. The computer then increases the AOM frequency, via a GPIB controlled SRS function generator, by a user-specified step size of, say, 5 kHz. Following the frequency increase of the AOM (now at 205.005 MHz), the experiment is again repeated 100 times. Again, the photon counts are analysed and displayed on the plot, and so on. The total time required to gather the frequency scan in Fig. 3.12 is approximately 30 sec. This scan time varies as the number of repetition and frequency step size are changed. The data contained in the entire frequency scan is typically saved for later analysis. It should

---

[7]For laser beam alignment, the number of repetitions is typically reduced to ∼30, yielding faster scan times.

be noted, that changing the ouput frequencies of the various sythesizers through GPIB connections can only occur on a time scale of a few msec($\sim$15 msec). Here, since the frequency is changed after 100 repetition of the experiment ($\sim$500 msec), this GPIB reset time did not significantly affect the duty cycle of the experiment.

Before taking data, the real-time feedback provided by the LabView plots (photon counts) is used to precisely align all laser beams onto the ion. For instance, before taking the frequency scan shown in Fig. 3.12, the waist of each focused Raman beams is aligned by inserting a long pulse time in the Raman chapter (typically 10 msec which is hundreds of time longer than a coherent carrier π-pulse). When the Raman beams are aligned on the ion, there is some population that appears in the bright state (F=1). This increased bright state population is caused by spontaneous Raman scattering, optically pumping the population in the ^{2}S$_{1/2}(F = 1)$ levels (see Fig. 3.10). Obtaining the spontaneous emission signature requires careful alignement of the Raman beams onto the ion, which can sometime take as long as 10 minutes. As for the alignement of the detection beam, it is carried out by maximizing the averaged photon counts received during the detection time (200 μs). The π-beam on the other hand is aligned by optimizing the optical pumping efficiency from the bright state (F=1) to the dark state (initialization, section 3.2.1). In order to increase the sensitivity of the π-beam alignment, the pulse length is typically reduced to $\sim$200 nsec. At the completion of the alignment, the length of the π-beam is returned to its saturation value of 5 μs.

The experiment involves many rf generators at different frequencies which can be divided into two classes: (1) the rf generators that are phased-locked to a common 10 MHz stable clock signal (Raman setup), and (2) the ones that are not (i.e. detection AOM, repumper EOM, etc.). When a sequence of Raman pulses are applied to the ion (i.e. Ramsey experiment), the phases of each Raman pulse with respect to the first one determine the final state of the qubit, hence the requirement of phase stability in the Raman setup. However, for the experiments reported here, phase stability between Raman pulses was not required between pulses[8]. Here I describe

---

[8]For instance, Raman laser cooling and motional heating do not require multiple pulses to be

the various sythesizers used in the Raman setup. In order for the various Raman synthesizers to have a resolution of the order of 1 Hz, each rf synthesizers in the Raman setup are phased-locked to a stable 10 MHz SRS-DS345 arbitrary waveform generator. The Raman EOM is driven by an HP8672A synthesizer which is modified to be phase-locked to the external 10 MHz clock signal[9]. The variable Mach-Zehnder AOM is driven by the octupled output of a SRS-DS345 synthesizer. The octupler, with a center wavelength of 26 MHz and bandwidth of ± 1 MHz, takes the phase-locked output of various SRS-DS345 frequency synthesizers oscillating near 26 MHz and converts them to a stable signal around 208 MHz. The fixed Raman AOM is driven by an HP8660C, which is also phase-locked to the 10 MHz clock signal. The other AOMs such as the one used for the detection beam, are driven, for the most part, by HP8640B's.

coherent with respect to the others.

[9]In fact, in order to have phase-locked signals for the microwave horn (14.5 GHz) and the Raman EOM (7.266 GHz), both signals are derived from the same HP8672A

CHAPTER 5

Photoionization-loading of trapped Cd$^+$ ions with ultrafast pulses

An important practical aspect of operating an ion trap is the efficient and con-
trolled loading of ions into the trap. The standard method for producing positively
charged trapped ions is electron bombardment (discussed in section 2.3.1), usually
from electron beams having energies (i.e. ~ 100 eV) comfortably above the ionization
threshold. However, electron-beam loading of ions can adversely impact ion trap per-
formance by degrading vacuum quality, charging nearby insulators, and corrupting
the surface quality of the trap electrodes. Photoionization-loading of ion traps is an
attractive alternative, as it avoids the use of electron filaments and can be much more
efficient than electron bombardment.

Several groups have enjoyed the benefits of photonionization-loading with particu-
lar atomic ions, including Mg$^+$ [60] and Ca$^+$ [61, 62]. Loading of ions is fairly efficient
in these systems, with the photoionizing lasers tuned to an intermediate atomic reso-
nance en route to ionization. Furthermore, the use of narrowband photoionizing lasers
allows isotopic selectivity, as the optical isotope shift in the intermediate resonance
is typically larger than the resonant linewidth of the atom.

In this chapter I describe a technique which uses ultrafast laser pulses to photo-
nionize and load cadmium ions in a variety of rf trap geometries. The laser center
frequency is tuned to an intermediate resonance in neutral cadmium, and the same
pulse then has enough energy to promote the electron to the continuum, or alter-
natively a continuous-wave laser beam used for laser-cooling the ion can itself ionize
the neutral from the intermediate resonance. Owing to the large bandwidth of the

laser, all velocity classes of a room-temperature cadmium vapor can be ionized, resulting in an extremely efficient method for producing trapped cadmium ions. Also, due to this high loading efficiency, the atomic flux aimed at the center of the rf trap can be reduced to a level where negligible coating of the electrodes occurs. The resulting operation of clean ion traps may help in quenching the suspected electrode contamination-driven heating of trapped ions [36, 18, 26].

5.1 Photoionization scheme

The relevant energy levels of the neutral cadmium atom are shown in Fig. 5.1(a). The output of a quadrupled Ti-Sapphire (Ti:S) mode-locked pulsed laser with wavelength at 228.8nm is resonant with the $5s^2$ $^1S_0 \rightarrow 5s5p$ $^1P_1$ transition ($\gamma/2\pi = 84.4MHz$). The same laser then promotes the intermediate $^1P_1$ state population to the continuum 3.6 eV above the ionization threshold. Fig. 5.1(b) shows the energy levels of a singly ionized even isotope[1] of cadmium (CdI). In order to crystalize and detect the presence of the newly trapped ion, the output of a quadrupled cw Ti:Sapphire laser (Doppler beam) is red-detuned from the $5s^2S_{1/2} \rightarrow 5p$ $^2P_{3/2}$ transition of the particular Cd$^+$ ion isotope loaded (Fig. 3.1). The photons in the Doppler beam also have enough energy to ionize from the intermediate $^1P_1$ state, but as we will show below, its relative importance in the photoionization process is dependent on the ratio of the average optical power of the pulsed laser and Doppler beam.

Other typical trapped ion species such as Be, Mg, Ca, Ba, Hg , Yb, and Sr can also utilize the same two-photon process described here - they all have an intermediate excited $^1P_1$ state further in energy than halfway toward the continuum (Table 5.1). However, some species may require a different laser setup than what is used in this experiment by virtue of the fact that their particular $^1S_0 \rightarrow ^1P_1$ transition wavelengths may be significantly different from that of Cd. The 2-photon ionization path described

---

[1]Energy levels for both odd isotopes of singly ionized Cd (^{111}Cd$^+$ and ^{113}Cd$^+$) have the same structure (shown in Fig. 3.2). In this experiment, however, the hyperfine structure of the odd isotopes plays no role since the repumper beam is always turned on (section 3.2.2).
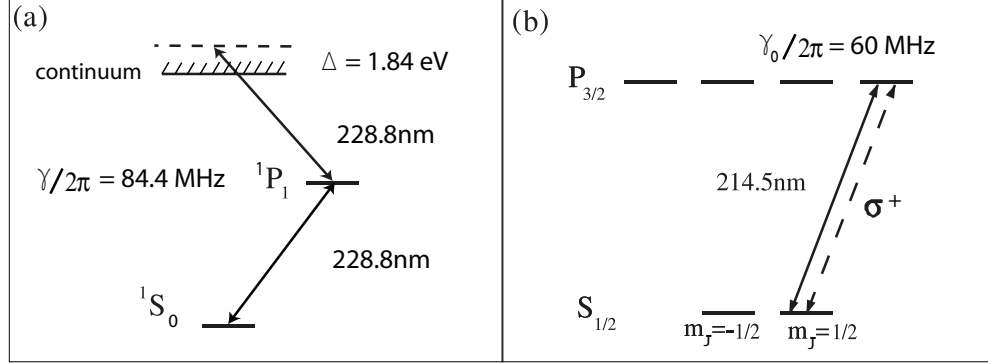
Figure 5.1: (a) Relevant energy levels for the neutral Cd atom. The intermediate excited $^1P_1$ state ($\gamma = 84.4MHz$) is located 1.8 eV above the midpoint of the energy difference between the $5s^2$ $^1S_0$ ground state and the continuum, which places the second transition ($5s5p$ $^1P_1 \to \infty$) comfortably above the continuum treshold. (b) Energy levels for a singly ionized even isotope of Cd with zero nuclear spin ($I = 0$). The hyperfine structure of the odd isotopes (^{111}Cd$^+$ and ^{113}Cd$^+$, shown in Fig. 3.2) plays no role in this experiment, since the repumper beams are always turned on (section 3.2.2). The output of a continuous wave Ti:S laser having σ^+ polarization (Doppler beam) is tuned near the resonance of the $5s$ $^2S_{1/2} \to 5p$ $^2P_{3/2}$ cycling transition ($\lambda = 214.5nm$). The excited $5p$ $^2P_{3/2}$ state has a natural linewidth of $\gamma_o/2\pi = 60MHz$. The laser Doppler cools the motion of the newly formed ions - crystalizing them at the center of the rf trap. Typically, the average optical intensity of the Doppler beam at the center of the trap is on the order of $50I_{sat}$.

Atoms	Cd	Be	Ca	Sr	Ba	Mg	Hg	Yb	Zn
$^1S_0 \rightarrow {}^1P_1$, λ (nm)	228.5	235.5	272.2	293	350.2	285.3	185	398	213.8
$^1S_0 \rightarrow \infty$, λ (nm)	139	133	202.8	217.7	237.9	162	119	198	132

Table 5.1: Typical atomic species used in ion trapping experiments along with their relevant transition wavelengths. For each atom, the chosen intermediate excited $^1P_1$ state is the first that lies above the midpoint in the energy separating the ground state and the continuum - thus making a 2-photon ionizing process feasible. The laser setup used in this experiment can be directly applied to all atomic species listed in the table - with the exception of Hg which requires a laser output with prohibitively low wavelength (185nm). Two ions in particular can use a direct 1-photon ionization scheme with realistic laser wavelengths, namely Sr (217.7nm) and Ba (237.9nm).

here can be viewed as a special case of all possible n-step photoionization processes. Hence in general, one question arises: what are the considerations in determining the optimal number of transition steps in the photoionization process? For instance, in most circumstances a single photon process will be the most efficient path toward the continuum. However, for most trapped ion species the wavelength of this direct process is prohibitively low (<205nm, optical absorption), hence making it impractical with current technology. Notable exceptions are Sr (217.7nm) and Ba (237.9nm) - where a direct 1-photon ionization process may then be the favoured scheme (Table 5.1).

The loading rate of ions is expected to depend strongly on the particular ion trap geometry being used. The loading rate dependence on trap parameters such as loading volume, trap depth, and secular frequency, which often characterize a particular trap geometry, is investigated. As such, pulsed laser photoionization loading is carried out in several types of ion trap: an asymmetric quadrupole ring-and-fork trap (section 2.2.1[2]), a symmetric quadrupole two-needle trap (section 2.2.1), a three-layer linear trap (section 2.2.2), a four-rod linear trap (section 2.2.2[3]), and a microfabricated GaAs linear trap (basic schematic shown in Fig. 5.2). Their relevant operational characteristics, such as trap depth, loading volume, secular and drive frequencies are listed in Table 5.2. The characteristic trapping volume for all traps extends over a wide range, from a linear dimension of 45 μm for the two-needle trap up to a dimension of 750 μm for the ring-and-fork trap. The trap depth ranges from values near room temperature (1/40 eV) in the cases of the needle and microfabricated GaAs ion traps, while at the other extreme, the three-layer linear trap has a trap depth sometimes exceeding 5 eV. Below I discuss how different values of these parameters are observed to impact the loading rate.

---

[2]The asymmetric quadrupole trap used here is a scaled up version of the one described in section 2.2.1

[3]The four-rod linear trap used here is similar to the one depicted in Fig. 2.3, except that the endcaps, providing the static confinement, are replaced by needle-like electrodes positioned on each side of the trap center and aligned in a direction parallel to the rods.

Traps	Depth (eV)	Trap size (μm)	$\omega_1, \omega_2, \omega_3$ (MHz)	Ω_{rf} (MHz)
4-rod	0.35-1.8	700	(0.25-0.7,0.8,0.81)	36
Ring-and-fork	0.8	750	(0.5,0.75,1.25)	50
3-layer	0.2-5	200	(0.6-4,8.1,8.3)	47
GaAs chip trap	0.08-0.125	60	(0.8-1,3.3,4.3)	16
Two-needle trap	0.02-5	46-600	(0.25-5,0.25-5,0.5-10)	29

Table 5.2: Ion trap geometries where ions are loaded using ultrafast laser pulses along with the operational range of relevant trap parameters.

5.2   Theoretical ion production rate

In this section, we calculate the expected photoionization rate for a 2-photon process. The resulting expression highlights the dependence of the loading rate on controlled experimental parameters such as pulse energy, pulse time duration, loading volume, and neutral atom density. As such, we solve the optical Bloch equations for the photoionization rate of a single atom excited to an intermediate resonance following Fig. 5.1(a). We assume the pulsed laser peak intensity to be in the weak perturbative regime [63], so that no other electronic states are involved in this process, and that the applied laser radiation does not couple to quasi-bound resonances above the ionization threshold.

The laser pulse train consists of individual pulses of duration (τ) $0.1 - 1.0$ psec and peak intensity I, separated by a pulse period of $T = 12.5$ nsec. The pulsed laser resonantly couples the initial ground $5s^2\,{}^1S_0$ electronic state to the intermediate exited $5s5p\,{}^1P_1$ state, with Rabi rotation angle $\theta = g\tau$, where the Rabi frequency $g = \gamma\sqrt{I/2I_{sat}}$, and γ and I_{sat} are the ${}^1P_1 \rightarrow^1 S_0$ decay rate and saturation intensity, respectively. The same laser pulse is capable of sequentially ionizing the atom. The photoionization rate from the ${}^1P_1$ state is $\Gamma = I\sigma/\hbar\omega$, where σ is the ${}^1P_1$ photoionization cross-section and ω is the laser frequency. A continuous-wave laser with intensity I_{cw} used for laser-coooling of the eventual ion can also ionize the neutral atom once

in the $^1P_1$ state with rate $\Gamma_{cw} = I_{cw}\sigma_{cw}/\hbar\omega_{cw} \ll \gamma$, where the cw laser parameters are defined analogously to the pulsed laser.

When the $^1P_1$ spontaneous emission lifetime is much shorter than the laser pulse period ($\gamma T \gg 1$), the neutral atom returns to the ground $^1S_0$ state before the next pulse (unless it has ionized). We therefore consider the net probability of ionization per laser pulse period T, including the effect of the cw laser, by integrating the optical Bloch equations in time:

$$P_{ion} = 1 - e^{-\Gamma\tau/2}\left(1 + \frac{\Gamma\tau}{2}\frac{sin\theta}{\theta}\right) + e^{-\Gamma\tau/2}\left(\frac{\Gamma_{cw}}{2\gamma}\right)(1 - cos\theta) \qquad (5.1)$$

In this expression, we have assumed that the photoionization rate from the $^1P_1$ state is much weaker than the coherent coupling between the $^1S_0$ and $^1P_1$ states in the atom, or $\Gamma \ll g$. This is valid for typical atomic systems considered here and for typical (perturbative) laser intensities, presuming no above-threshold resonances.

The first two terms in the equation arise from photoionization from the pulsed laser exclusively, while the last term describes the contribution from the cw laser. For similar average intensities of the cw and pulsed lasers ($I_{cw} \approx \overline{I} = I\tau/T$) and assuming that the photoionization cross section from the $^1P_1$ state is similar for the two processes, we find that photoionization probability from the pulsed laser alone is roughly γT times larger than the photoionization from the cw laser. In the cadmium system considered here ($1/\gamma \approx 2$ nsec and a $1/T = 80$ MHz laser repetition rate), this amounts to the pulsed laser ionizing the atom about 6 times more effectively than the cw laser with the same average laser powers. Below, we assume that the cw and pulsed lasers have equivalent average laser intensity and therefore neglect the effect of the cw laser on photoionization.

For $\Gamma\tau/2 \ll 1$, the ionization probability from the pulsed laser alone simplifies to

$$P_{ion} \simeq \frac{\Gamma\tau}{2}\left(1 - \frac{sin\theta}{\theta}\right) \qquad (5.2)$$

$$\simeq \frac{\theta^2\Gamma\tau}{16} \qquad (5.3)$$

with the last approximation accurate to within 25% for $0 < \theta \leq \pi$.

Since the ionization cross section from the cadmium $^1P_1$ state is not known precisely, we use as guides previous measurements in atomic magnesium [64], calcium [62] and barium [65], since the electronic structure of these two-electron systems are similar. These experiments reported photoionization cross sections from their respective $^1P_1$ states using laser radiation well above the ionization theshold by similar amounts of energy to that considered here. We estimate to an order of magnitude that the cadmium cross section is $\sigma \sim 10^{-16}$ cm^2 for light at 229 nm. Expressed in terms of average laser pulse power $\overline{P}$ for an 80 MHz laser repetition rate and focused down to a waist of $w \sim 10\mu$m, we find $P_{ion} \sim 5 \cdot 10^{-5}\tau\overline{P}^2$, with τ in psec and $\overline{P}$ in mW.

We now solve for the experimental quantity of interest - the loading rate of ions R_{ion} into the trap. The following calculation gives a lower estimate, as it assumes that the source of Cd atoms is from the background vapor pressure of Cd at room temperature (10^{-11}torr). The rms velocity of cadmium atoms in a vapor is roughly $v_{th} \sim 150$ m/s in a given direction, so a typical atom travels $v_{th}T \sim 2\mu$m in the time between successive laser pulses. We can therefore estimate the total rate of ions produced in the loading volume V formed by the intersection of the trapping region and the laser beam by

$$R_{ion} = \frac{1}{4}[1 - (1 - P_{ion})^M]nAv_{th} \tag{5.4}$$

where $M = \frac{4R/3}{v_{th}T}$ is the number of laser pulses an atom moving with velocity v_{th} will experience traversing a trap volume (assumed spherical with radius R), n is the density of cadmium atoms in the vapor, and $A = \pi R^2$ is the transverse cross-sectional area of the loading volume. For $P_{ion} \ll 1$, we find $R_{ion} = P_{ion}nV/(4T)$. This can be compared to the total rate of atoms traversing the same region $R_0 = nAv_{th}/4$ by defining the efficiency parameter $\eta = R_{ion}/R_0 = 4RP_{ion}/3v_{th}T$. The vapor pressure of cadmium metal at room temperature is roughly 10^{-11} torr [66, 67], giving a density of $n \sim 3 \times 10^5$ atoms/cm^3. For an 80 MHz laser repetition rate focused down to a waist of $\rho \sim 10\mu$m, we find $R_{ion} \sim 1.27\tau\overline{P}^2$ and $\eta \simeq 0.0004\tau\overline{P}^2$, with τ in psec and $\overline{P}$ in mW. For 2 psec pulses at an average power of $\overline{P} = 10$ mW, the efficiency is $\eta \simeq 8\%$, and for $\overline{P} \equiv 100$ mW the efficiency is expected to be near unity.

5.3   Laser system and experimental setup

Three lasers are used in this experiment: two photoinization pulsed lasers ($\lambda =$ 228.9) and a cw laser ($\lambda = 214.5nm$) used to crystalize the ions and image them onto an intensified CCD camera (Doppler beam). Two different time scales are investigated in the photoionization process - one pulsed laser provides excitation on the picosecond time scale (psec laser) while the other provides excitation on the femtosecond time scale (fsec laser). The psec excitation pulses at a repetition rate of 80 MHz are generated by a mode-locked Ti:S pulsed laser from Spectra-Physics (Tsunami). A typical average output power of 1W at 916 nm is first frequency doubled throught a 12mm long LBO nonlinear crystal and further doubled in a 10mm long BBO nonlinear crystal - typically yielding 1mW at the excitation wavelength of 228.8 nm. Both nonlinear crystals are critically phased matched (angled tuned) at their corresponding wavelengths. The fsec laser, which is also used in other experiments presented in this thesis, is described in section 4.1.3. It is characterized by an average output power of 550mW ($\lambda = 916nm$) with a repetition rate of 86 MHz. It is first frequency doubled through a 7mm long LBO nonlinear crystal and then further doubled through a 5mm long BBO nonlinear crystal - typically yielding an output of 10mW at 228.8 nm. Again, both nonlinear crystals are critically phase matched. A spectrum analyser with a resolution of $\sim$1 nm is used to determine the pulse bandwith and time duration.

The layout of the experiment is depicted in Fig. 5.2. Both lasers enter the trapping region at an oblique angle of 45° with respect to the principle axis of the rf Paul trap allowing the cw Doppler cooling beam to cool all three directions of the ion's motion. The scattered light from the ions is captured by an f/2.1 imaging system and is sent onto the intensified CCD camera. Most ion traps, with the exception of the microfabricated GaAs trap [68], did not require the use of a Cd oven for the loading of ions. The large vapor pressure of Cd at room temperature (10^{-11} torr) resulted in just the right amount of background neutral Cd atoms - large enough for practical loading rates ($R_{ions} \geq 1sec^{-1}$) while still small enough to not compromise the lifetime of the ions in the rf traps through collisions. However, even in the case where the oven

is heated to increase the flux of neutral Cd atoms in the trapping region, the velocity-induced Doppler shifts are negligible compared to the laser bandwidth (>1THz). This removes the requirement of having the atomic beam from the oven directed at a 90 degree angle with respect to the photoionization laser beam in order to be insensitive to Doppler broadening.
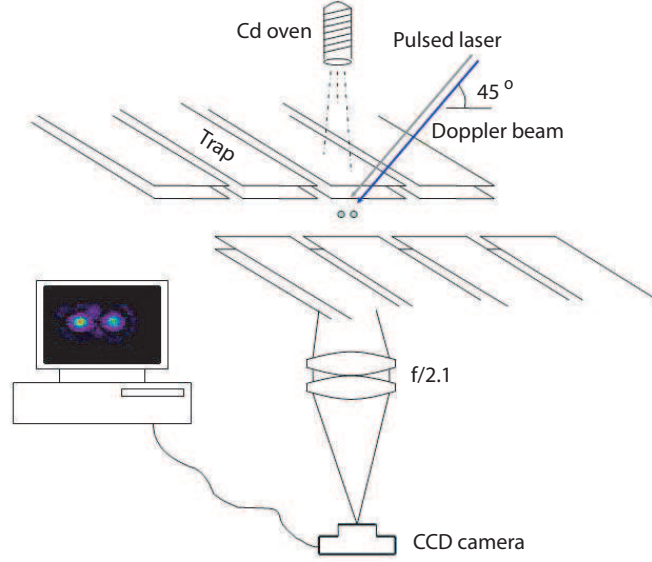
Figure 5.2: Schematic for the layout of the photoionization experiment. The Doppler and pulsed laser beams typically enter the trapping region at an oblique angle of 45° with respect to the principle axis of the rf Paul trap. The scattered light from the ion is captured by an f/2.1 imaging system and is sent onto the intensified CCD camera (section 4.2). Most ion traps, with the exception of the microfabricated GaAs chip trap, did not require the use of a Cd oven for the loading of ions. However, when used, the atomic beam from the oven is directed toward the center of the trap where it intersects the Doppler and pulsed laser beams. The ion trap depicted in the figure is the GaAs chip trap (Table II).

5.4 Experimental results

In this section I present two experimental results: (i) the loading rate of ions vs

average optical power of the photoionization beam, and (ii) the loading rate of ions vs pulsed laser detuning from the intermediate $^1P_1$ state. These results are aquired by recording the loading rate of a *single* ion as a function of the parameter to be varied (average optical power or detuning of the photoionization laser). I will conclude this section with some qualitative observations regarding the dependence of the loading rate on several ion trap parameters, such as loading volume, trap depth, etc.

A plot of the loading rate of ions vs average optical power of the photoionization beam is shown in Fig. 5.3. The loading rate is monitored as the average optical power in the photoionization beam is increased. These data are taken in the three-layer linear trap (Table II) using the fsec pulsed laser. The probability of occupying the intermediate $^1P_1$ state is expected to reach a value of 1.5% when the average optical power is at its maximum value of 4mW (with a beam waist of 10 μm) - well within the perturbative regime. As previously mentioned (Eq. 5.2), this regime is characterized by a quadratic dependence of the photoionization rate (loading rate) on the average optical power of the pulsed laser. Fig. 5.3 indicates this nonlinear behavior.

The steps involved in aquiring a single data point are as follows: the photoionization beam, focused at the center of the ion trap with a waist of $\sim$10 μm, is turned ON for a duration of 5 or 10 sec, which corresponds to a slightly shorter time interval than what is required to load a single ion. Then the Doppler cooling beam ($I \sim 50I_{sat}$) is turned ON, initially red-detuned from the cycling transition of every Cd^+ isotope (i.e. $\sim$300 MHz red detuned from the $^{111}Cd^+$ cycling transition). In order to determine if an ion has been loaded, the wavelength of the Doppler beam is then progressively tuned toward the resonance of each isotope, where the resulting strong fluorescence is the unmistakable signal indicating the presence of a trapped ion. Finally, in order to prepare for the next loading sequence, the ion trap is "dumped" (rf voltage turned off and on) which ejects any Cd^+ ion that had just been loaded. For each average optical power of the photoionization pulsed laser, these loading steps are repeated ~ 8 times, giving the loading rates displayed in Fig. 5.3. The main factor which limits this sample size is the slowly fluctuating beam-steering noise of the photoionization

pulsed laser. Observations indicate that loading rate fluctuations caused by this beam steering noise occur on a time scale of 20-30 minutes, which limits the number of times a single ion can be loaded.

Fig. 5.4 shows the loading rate of ions vs pulsed laser detuning from the intermediate excited $^1P_1$ state. The loading rate of ions is monitored as the center wavelength of the excitation pulsed laser is progressively detuned from the intermediate $^1P_1$ state. This is done using the same sequence of steps described previously. The data for this curve is taken in the asymmetric quadrupole "ring and fork" ion trap (Table II) using the psec pulsed laser. The photoionization pulsed laser is focused at the center of the trap to a $\sim$10 μm waist and has an average optical power of 1 mW. By examining Fig. 5.4, the process is seen to be resonant in the sense that the loading rate is maximized when the photoionization laser is on resonance with the intermediate $^1P_1$ state. The width of the photoionization curve corresponds to the bandwidth of the excitation laser (bandwidth $\sim$ 1THz). This large bandwidth can be beneficial insofar as Doppler shifted levels from all velocity classes are simultaneously resonant with the pulsed laser, thus allowing for the possibility to photoionize each atom passing through the loading region.

The loading rate is observed to depend on several trap parameters. Here we list a few intuitive, albeit qualitative, observations. A large loading volume as well as a large trap depth consistently display a higher loading rate. This observation was best exampified when comparing the behavior of the large 4-rod linear trap and the microfabricated GaAs trap (see Table II for trap parameters). For instance, the 4-rod linear trap shows loading rates on the order of 1 sec^{-1} while using background vapor pressure of Cd (@300K), where on the other hand, the microfabricated GaAs trap can only load by significantly increasing the number density of Cd atoms in the loading region by heating a Cd oven. Similarly, the same behavior is observed in the two needle trap, where, as the trap size is varied from 46 to $300\mu m$, the loading rate is seen to increase dramatically. As previously mentioned, the Doppler beam, with an average optical power comparable to the pulsed laser, should not significantly contribute in the photoionization process. In order to test this assertion, we compared
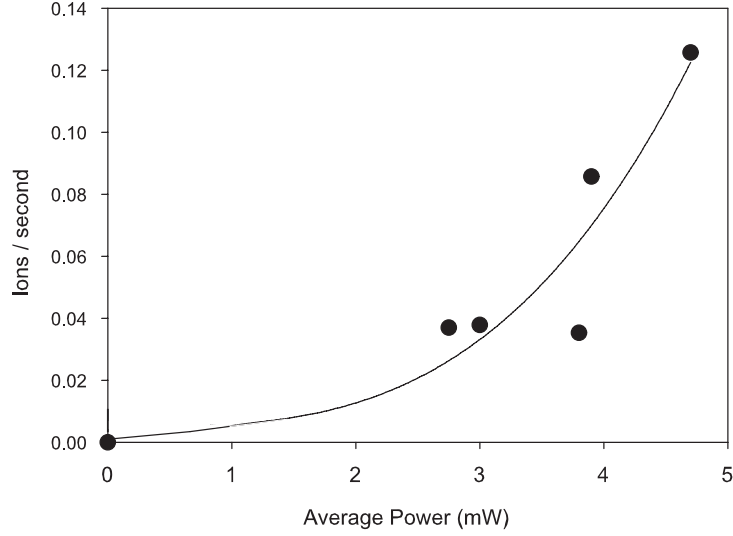
Figure 5.3: Loading rate vs optical power in the photoionization pulsed laser. The data for this curve is taken in the three layer linear trap (Table II) using the fsec pulsed laser. The source of neutral Cd atoms is from the background Cd vapor pressure in the vacuum system, corresponding to a number density of $3 \times 10^5/\text{cm}^3$ of at room temperature. The photoionization pulsed laser is focused at the center of the trap to a $\sim 10~\mu m$ waist. For each detuning, the loading is aquired by: (1) turning ON the pulsed laser at the center of the ion trap for a fixed time interval of either 5 or 10 seconds (slightly shorter than the time to load multiple ions); (2) turning ON the Doppler beam in order to detect the presence of a trapped ion; (3) and then "dumping" the ion trap (rf voltage is turned off and on) which ejects any Cd^+ ions that have just been loaded. For each value of the average optical power in the pulsed laser, these loading steps are repeated ~ 8 times. The perturbative regime, where the population in the intermediate state is much smaller than unity, is characterized by a quadratic dependence on the optical power of the pulsed laser (Eq. 5.2). The curve clearly shows the nonlinear increase in the loading rate as the average optical power of the pulsed laser is increased. The solid line is a quadratic fit to the data.

the loading rate *with* and *without* having both Doppler and pulsed laser beams turned ON at the same time. We observed that the loading rate does not seem to be affected by the added presence of the Doppler beam. This was tested in the large 4-rod linear trap and the small GaAs linear trap.

In summary, we have demonstrated efficient photoionization loading of trapped cadmium ions using frequency-quadrupled Ti:S mode-locked pulsed lasers. The laser pulses resonantly promote neutral cadmium atoms to an intermediate excited state that subsequently photoionizes. Observed loading rates of about 1 ion/sec are consistent with a simple model of the photoionization process. Because the pulses are broadband, all velocity classes of atoms can be photoionized, leading to a very efficient loading technique. With reasonable intensities, we expect that ultrafast laser pulses can successfully load every atom that traverses the laser beam within the trapping volume. This may allow ion trap electrodes to be cleaner than in previous systems, and lower pressures in the trapping region.
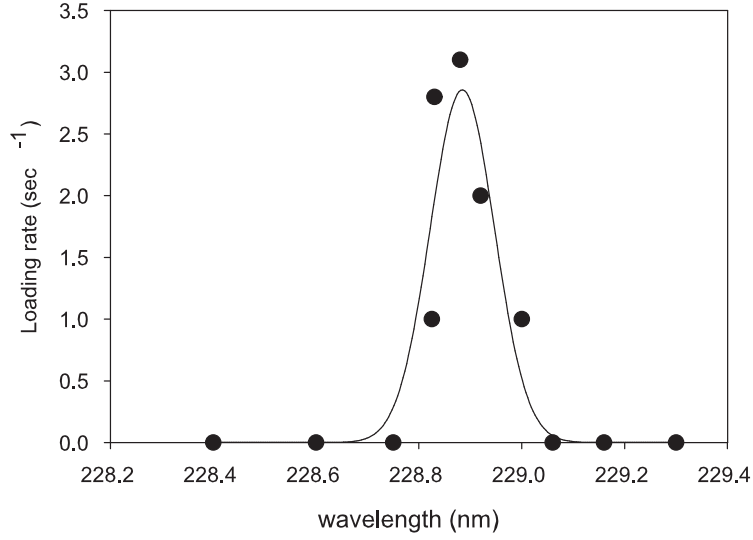
Figure 5.4: Loading rate vs detuning of the photoionization laser from the intermediate $^1P_1$ state. The data for this curve is taken in the asymmetric quadrupole "ring and fork" ion trap (Table II) using the psec pulsed laser. The source of neutral Cd atoms is from the background Cd vapor pressure in the vacuum system, corresponding to a number density of $3 \times 10^5/\text{cm}^3$ at room temperature. The photoionization pulsed laser is focused at the center of the trap to a ~ 10 μm waist and has an average optical power of 1 mW. For each detuning, the loading is aquired by: (1) turning ON the pulsed laser at the center of the ion trap for a fixed time interval which is slightly shorter than the time to load multiple ions, (2) turning ON the Doppler beam in order to detect the presence of a trapped ion, and (3) "dumping"the ion trap (rf voltage turned off and on), ejecting any Cd$^+$ ion that had just been loaded. For each value of the pulsed laser detuning, these loading steps are repeated ~ 8 times. The data clearly shows the resonant nature of the photoionization process, where the loading rate is significant only when the pulsed laser bandwidth overlaps with the intermediate $^1P_1$ state. In this case, the bandwidth of the laser used is 1 THz, which matches with the width of the curve. The solid line is a a guide to the eye showing the pulsed laser bandwidth.

CHAPTER 6

Laser cooling of trapped ^{111}Cd$^+$ ions

For most experiments that require entangling ions through their collective motion, it is a prerequisite that the secular motion of the ion be cooled to near its ground state $\langle \hat{n} \rangle \sim 0$. Immediately after loading the ion into the trap the kinetic energy is on the order of the trap depth (0.05-10 eV, see chapter 5), which, for typical trap frequencies of a few MHz, corresponds to a thermal distribution of motional levels having a mean of $\langle \hat{n} \rangle \sim 10^6$. The ground state is reached with the help of two successive cooling stages. Doppler cooling first takes the ion's motion from room temperature down to a temperature of ~ 1 mK, but the corresponding mean number of motional quanta in the harmonic well depends on the trap stiffness. For typical trap frequencies in this experiment of 2 MHz, the average number of quanta that results from a Doppler cooling stage is $\langle \hat{n}_D \rangle \sim 13$. The remaining excess energy is removed with a stage of resolved sideband stimulated Raman cooling, which takes the motion down to near the motional ground state.

While these two cooling techniques are a ubiquitous feature in all experiments involving trapped ions, they are only useful at the beginning of such experiments. The removal of entropy, necessary in all cooling processes, relies on spontaneous emission of the ion being cooled. This of course, precludes the use of these techniques if the electronic level coherence is to be preserved. An alternative is to sympathetically cool the motion of an ion (qubit) by directly cooling a neighboring "'refrigerator" ion. The motional coupling between the ion to be cooled (qubit) and the cold reservoir (ancillary ion) is provided by their coulomb coupled motion.

I will first describe the underlying mechanisms of these two cooling stages and then present experimental data showing their implementation in the Cd^+ system. I will then conclude the chapter by describing the experimental demonstration of sympathetic cooling of a probe ion ($^{112}Cd^+$) through direct Doppler cooling of a neighboring refrigerator ion ($^{114}Cd^+$).

6.1   Doppler cooling

The concept of Doppler cooling the motion of atoms was first proposed jointly by two research groups: Wineland and Dehmelt [11] for harmonically bound atoms and by Hänsch and Schawlow in the case of free neutral atoms [12]. The proposed cooling technique was first demonstrated three years later in the work of Wineland and Dehmelt [13] and Neuhauser et al. [14]. The relative simplicity of this cooling technique makes remarkable the wealth of scientific discoveries it would later enable. Nowadays, it is assumed that a Doppler cooling stage is the starting point of any experiment involving the motion of a trapped atom.

There are two regimes to distinguish in the motion of a trapped ion: the weak-binding limit ($\omega_x \ll \gamma_o$) and the resolved sideband or strong-binding limit ($\omega_x \gg \gamma_o$). The concept of Doppler cooling only applies to the weak binding case, where, due to the short lifetime of the excited state, the ion position does not change significantly during each photon scattering event. This allows an intuitive picture to be developed. For simplicity we assume that the motion of the ion is along a single direction and that the laser beam used for Doppler cooling is directed along the same axis of motion. The Doppler beam is tuned below resonance of the strongly allowed dipole transition used to scatter photons, as shown in Fig 3.2. When the ion travels in a direction opposing the $\vec{k}$-vector of the Doppler beam, the laser appears blue shifted toward resonance in the frame of the moving ion, hence increasing the photon scattering rate. Here we are assuming that the Doppler shift $\delta\omega_D = \vec{k} \cdot \vec{v}$ is much smaller than the natural linewidth of the cycling transition. Each time the ion absorbs a photon, it recoils in a direction opposing its motion, so as to reduce its kinetic energy. Of course every absorption

is accompanied by a spontaneously re-emitted photon. However, since the emission occurs symmetrically, the net recoil following many scattering events averages to zero. On the other hand, when the ion is moving in the opposite direction (away from the Doppler beam), the laser now appears further red shifted with respect to resonance, resulting in a lower photon scattering rate. This imbalance in the photon scattering rate has the net effect of reducing the ion's motional kinetic energy.

In order to Doppler cool all three directions of motion, the wave-vector of the Doppler beam is directed at an oblique angle with respect to the trap's principle axes. In the case where two trap frequencies are degenerate, there is always a mode that is uncoupled to the Doppler beam. This mode is therefore not laser cooled, however its motion is heated due to the recoil from the spontaneously emitted photons. Every traps described here possessed some inherent asymmetry which prevented this from occurring.

In general, the limiting kinetic energy associated with this laser cooling technique is $\langle E_D \rangle = \hbar\gamma_0/2 = \hbar\omega_x \langle \hat{n} \rangle$ [48]. However, this cooling limit is only approximate as it does not account for the non-isotropic radiation pattern that is associated with the spontaneously emitted photons. Including this and the fact that the Doppler beam has a 45° angle with respect to the principle axis of interest (x-axis), the Doppler cooling limit is reduced to $\langle E_D \rangle = 17\hbar\gamma_0/40$. For a typical trap frequency of 2 MHz, this corresponds to a thermal distribution having a mean of $\langle \hat{n}_D \rangle = 13$. This cooling limit can be understood in terms of the ion undergoing a random walk in momentum space with discrete steps of $\hbar\vec{k}$, where each step corresponds to the recoil from a spontaneously emitted photon. The random walk model predicts a net momentum gain of zero $\langle \Delta\vec{p} \rangle = 0$, however the residual kinetic energy due to the random momentum kicks is nonzero since it is proportional to the square of the momentum ($E_D \sim \langle (\Delta\vec{p})^2 \rangle \neq 0$). When the Doppler cooling rate comes to equilibrium with this residual heating mechanism, steady-state is reached, leaving the motion in a thermal distribution [39] with a probability of occupying the vibrational state n expressed as

$$P(n) = \left(\frac{\langle \hat{n} \rangle}{1 + \langle \hat{n} \rangle} \right)^n \left(\frac{1}{1 + \langle \hat{n} \rangle} \right). \tag{6.1}$$

The first step in Doppler cooling the ion's motion is to cancel background static fields and minimize micromotion, as shown in Fig. 6.1. Once micromotion is cancelled, a Doppler beam with an intensity at the ion of $I \approx I_{sat}/10$ is turned on for a duration of 1 msec, providing for $\sim$1000 photon scattering events (the Doppler pulse time of 1 msec was determined to be the shortest time duration yielding the Doppler cooling limit). In order to measure the temperature using the thermometry technique described in chapter 2, the population is initialized into the $|\uparrow\rangle$ state. The first red or blue sideband is turned on for a variable time, which maps the motional information onto the spin degree of freedom. We then measure the population in the bright state (F=1) with the detection beam. Fig. 6.2 shows Rabi flopping on the first (a) red and (b) blue sidebands, taken immediately following Doppler cooling stages. The data is taken in the needle trap described in chapter 7, where the secular trap frequency was 3.48 MHz ($\eta_x \simeq 0.15$). The red and blue sideband asymmetry indicates a thermal distribution with average population of $\langle \hat{n}_D \rangle \simeq 6.5(2)$. In order to cool the motion below the Doppler limit, we use a resolved sideband cooling technique, which I discuss in the next section.

6.2 Resolved sideband laser cooling

6.2.1 Single-photon resolved sideband cooling

The thermal distribution resulting from a Doppler cooling stage with typical average population $\langle \hat{n}_D \rangle \geq 1$ requires an additional cooling stage in order to reach the ground state of motion. It is interesting to note that if the secular trap frequency was larger than the natural linewidth of the excited P state (strong binding limit, $\omega_x \gg \gamma_o$), the implementation of Doppler cooling described above would, with proper laser detuning from the excited P state, become the implementation of resolved sideband cooling. Single-photon resolved sideband cooling is relatively easy to implement and is a very efficient laser cooling technique. Unfortunately, the secular frequency
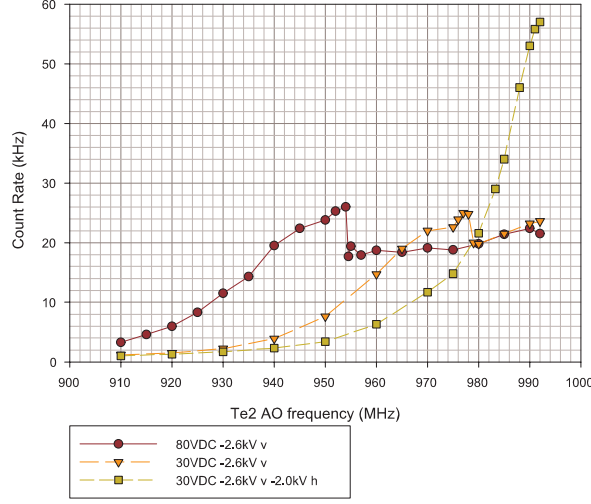
Figure 6.1: Plots of cycling transition lineshapes showing residual micromotion in the ring and fork trap. The detection laser is tuned below resonance of the cycling transition and the fluorescence count rate is displayed on the vertical axis. Due to the micromotion at the drive frequency ($\Omega_{rf}/2\pi$ =48 MHz), the detection laser aquires micromotion sidebands which smear the otherwise natural lineshape of $\gamma_0/2\pi$= 60 MHz. The laser is on resonance at 992 MHz and the actual UV frequency shift is 4 times the scale on the axis. The square boxes show the case of minimized micromotion and have a FWHM linewidth of 72 MHz. The lineshapes with triangles and circles correspond to increased levels of micromotion with different static offsets, as shown in the legend. Typically, the reduced slope in the atomic line shape used for Doppler cooling results in significantly hotter Doppler cooled distributions. The resulting thermal distributions are unable to be Raman cooled, as discussed in Fig. 6.5 and Fig. 6.6. This can be overcome by applying static voltages which offset the background field, as in the lineshape corresponding to square boxes.
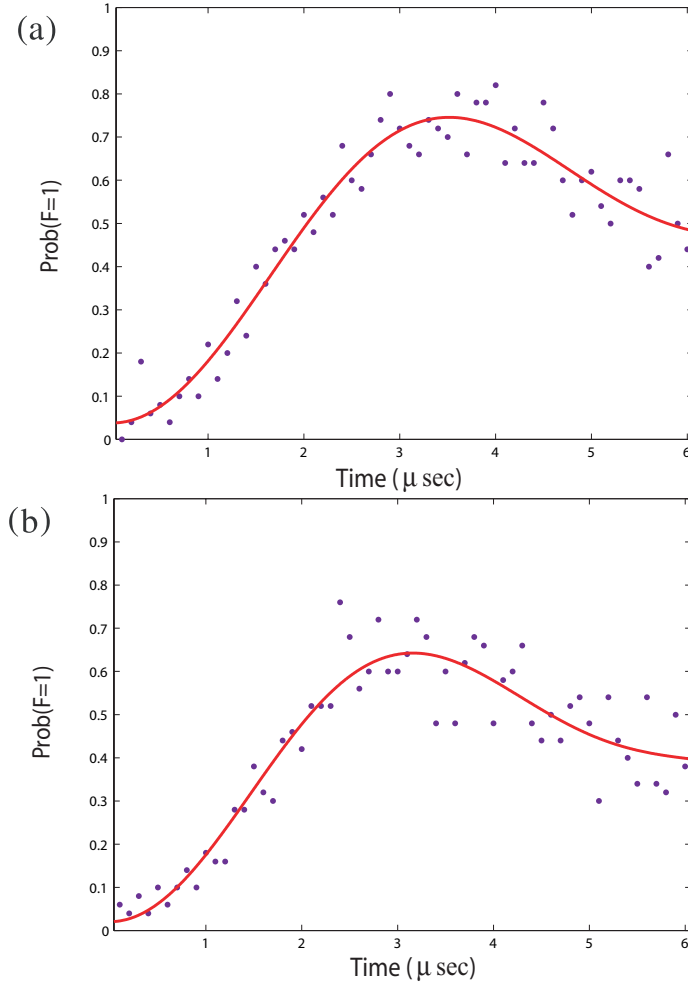
Figure 6.2: Rabi flopping on the (a) first red sideband and (b) first blue sideband, showing the ground state occupation probability P(F=1) vs the application time of the Raman beams. The trap frequency in the x-direction is 3.48 MHz, giving a Lamb-Dicke parameter of η=0.15. The data is taken following a Doppler cooling stage which leaves the ion's motion in a thermal distribution with an expected mean of $\langle n_D \rangle$=7.3. By considering the asymmetric ratios between the blue and red sidebands, we obtain a measured value of $\langle n_D \rangle \simeq 6.5(2)$. The different rabi frequencies in a) and b) stems from beam-steering of the Raman laser beams as the AOM is frequency shifted to access a particular resonance. Each point is averaged over 50 experiments, and the solid red lines are fits to the data.

of the trapped ion is usually constrained to be well within the weak binding limit - the excited P state linewidth is usually on the order of tens of MHz for most atomic species (i.e. $\gamma_{Be^+} = 19$MHz, $\gamma_{Cd^+} = 59$MHz, $\gamma_{Ca^+} = 23$MHz) and the secular frequency is typically well below 10 MHz. Notable exceptions are situations where a weaker electric quadrupole transition is available. The linewidth of such transition being in the Hz range places it comfortably within the strong binding limit. In fact, the first demonstration of laser cooling of a bound atom to its ground state of motion was done using such a narrow transition. In 1989, a NIST research group led by Diedrich *et al.* used the narrow $S_{1/2} - D_{5/2}$ electric quadrupole transition in ^{199}Hg$^+$ to cool its motion to $\langle \hat{n} \rangle \sim 0$ [15]. Although this seems easy to implement, the use of such narrow transitions requires a correspondingly narrow linewidth laser to excite the transition, making the method much less attractive.

The single-photon resolved sideband cooling technique was not used in the work described in this thesis, however plans were made to use such cooling technique with the two-needle trap apparatus (chapter 1 and 6), but time constraints prevented its implementation. The strong binding limit was going to be reached by increasing the secular trap frequency above the $^2S_{1/2} -^2 P_{3/2}$ cycling transition linewidth ($\gamma_0/2\pi$=60 MHz) used for Doppler cooling. In order to keep the motion of the ion stable (see secular approximation, section 1.2.2), this very large trap frequency (> 60MHz) required the building of a very high frequency bifilar helical coil resonator (≥ 250MHz).

The underlying mechanism of the single-photon resolved sideband cooling technique is very simple and yet quite revealing, it can be explained as follows: for simplicity we again assume that the motion of the trapped ion is along a single direction (x-axis), with a trap frequency ω_x. We further assume that the laser beam used for cooling is directed along the direction of motion and is tuned near resonance of the $S_{1/2} - P_{3/2}$ cycling transition. In the required strong binding limit ($\omega_x \gg \gamma_o$), the ion undergoes several oscillations before it absorbs a photon from the laser. The oscillating ion thus develops well resolved absorption sidebands composed of a central "carrier" at frequency ω_0 surrounded by resolved sidebands spaced by multiples of the trap frequency ω_x (i.e. $\omega_0 + n\omega_x$, where n is an integer). This can be understood

by considering how the laser beam appears in the frame of the ion as it oscillates back in forth in the trap. The laser beam appears to be frequency modulated at the trap frequency ω_x, thus yielding the discrete sideband spectrum described above. At this point, laser cooling occurs if the laser is tuned to the first red sideband at a frequency $\omega = \omega_0 - \omega_x$. Simply put, the ion absorbs a photon with energy $\hbar(\omega_0 - \omega_x)$, and spontaneously emitted photons with energy $\hbar(\omega_0 - \omega_R)$ return the ion to the electronic ground state, where $\hbar\omega_R \equiv (\hbar k)^2/2m$ is the recoil energy associated a spontaneously emitted photon. For each absorption-emission cycle, the kinetic energy of the ion's oscillation is damped by $\hbar\omega_x$, assuming $\omega_R \ll \omega_x$. The recoil energy associated with the $^2\mathrm{S}_{1/2}{\rightarrow}^2P_{3/2}$ transition in the Cd^+ ion ($\omega_R/2\pi = 39$ kHz) is much smaller than typical trap frequencies of a few MHz, which justifies the last assumption. In this case the motional state changes with probability $\eta^2(n + 1/2)$, where η is the Lamb-Dicke parameter given by $\eta = kx_0$. Considering the case of small vibrational quantum number n and $\eta^2 \equiv \omega_R/\omega_x \ll 1$, the probability of changing the motional state upon recoil is negligible. For this type of cooling, the expression for the limiting temperature is very similar to the one for Doppler cooling, and is given by $\langle \hat{n}_{min} \rangle \approx (\gamma_0/2\omega_x)^2$. However, this time, since $\gamma_0 \ll \omega_x$, the final mean vibrational number is much smaller than unity (i.e. $\langle \hat{n}_{min} \rangle \ll 1$).

6.2.2   Two-photon resolved sideband cooling

As previously mentioned, the combination of a natural linewidth $\gamma_0/2\pi$=60 MHz for the $^2S_{1/2}{\rightarrow}^2P_{3/2}$ transition in Cd^+ and typical trap frequencies of a few MHz, does not easily lend itself to laser cooling the motion to its ground state using a single-photon resolved sideband cooling technique. Instead, we use a two-photon stimulated Raman transition process (discussed in chapter 2). The single-photon technique has the advantage of simplicity over the two-photon technique. However, since the frequency beatnote required for Raman cooling is generated by a stable rf synthesizer, the relative phase of the two Raman beams can be controlled with rf accuracy, and not too high demands are put on the absolute stability of the laser.
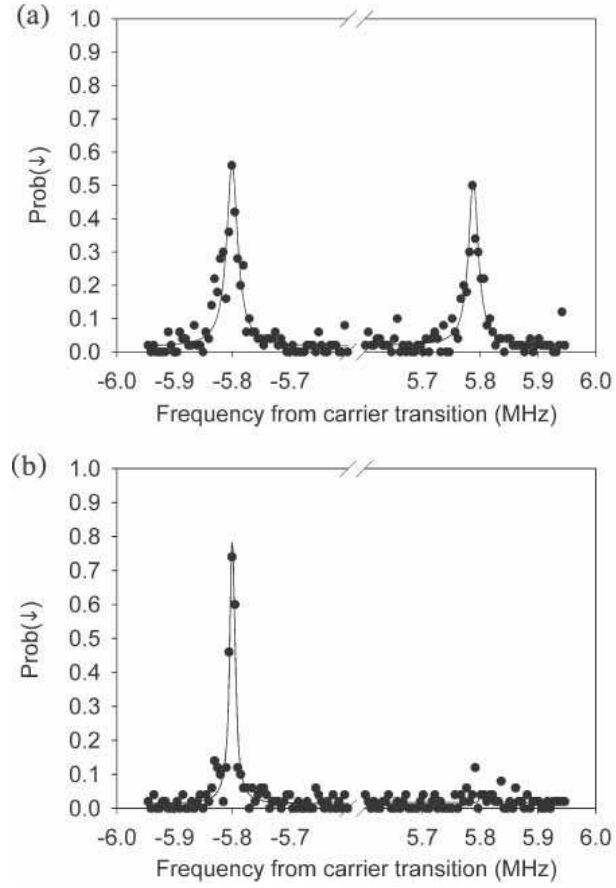
Figure 6.3: Raman spectra for an ion in the quadrupole trap with a secular frequency of $\omega_x/2\pi$=5.8 MHz. Both plots show probability for population transfer to the "bright state" $P(|\downarrow\rangle = |F = 1, M_F = 0\rangle)$ vs δ or frequency of the beatnote from a carrier transition. Both lower(left) and upper(right) sidebands are displayed following (a) Doppler cooling to $\bar{n} \simeq 5(3)$, and (b) subsequent Raman cooling to $\bar{n} \simeq 0.03(2)$ where the upper sideband vanishes. The strength of the transitions are $\Omega_0/2\pi = 100$ kHz and $\Omega_{0,1}/2\pi = 10$ kHz. The Raman probe pulse is exposed for 80 μsec. The lines are a Lorentzian fit to the data points

The steps involved for sideband laser cooling using stimulated Raman transitions are illustrated in Fig. 6.4. The initial overall quantum state consists of having the motion Doppler cooled in a thermal state and internal level initialized to the $|\uparrow\rangle$ state. In order to reduce the vibrational energy, a first blue sideband drives the $|\uparrow, n\rangle \rightarrow |\downarrow, n-1\rangle$ transitions. Then by applying the optical pumping beam, the electronic state population is recycled back into the $|\uparrow\rangle$ state. During this recycling process, the recoil energy associated with the spontaneously emitted photon is assumed to have negligible effect on the motion for $\eta^2 n \ll 1$. This, as previously mentioned in the case of single-photon sideband cooling, is usually a good assumption since the recoil frequency $\omega_R/2\pi$=39 kHz associated with the recycling step is much smaller than typical trap frequencies of a few MHz. This cycle is repeated many times until the mean vibrational state n=0 is reached. The cooling limit for this technique is typically limited to off resonant coupling to neighboring motional levels and by spontaneous emission from the small population in the excited state $|e\rangle$ (section 3.3.2).

In order to efficiently bring the motional state distribution to the ground state, the blue sideband cooling pulse lengths are typically adjusted in order to accommodate the variation in its coupling strength as a function of the vibrational state n. To illustrate, if n corresponds to the largest vibrational state we want to cool, then the first cooling cycle will involve a π-pulse on the $|\uparrow, n\rangle \rightarrow |\downarrow, n-1\rangle$ transition, with a time duration $t_{n \rightarrow n-1} = \pi/\Omega_{n,n-1}$. In the second cooling cycle, the π-pulse which couples the $|\uparrow, n-1\rangle \rightarrow |\downarrow, n-2\rangle$ transition is then applied for a time $t_{n-1 \rightarrow n-2} = \pi/\Omega_{n-1,n-2}$, and so on until the ground state is reached. This type of cooling schedule sequentially empties one motional level at a time.

Before the experiment starts, the cooling schedule is preset in Labview. By using the trap frequency and the π-pulse time for the $|\uparrow, 1\rangle \rightarrow |\downarrow, 0\rangle$ transition as parameters, the subroutine calculates the appropriate application times of the Raman pulses in the sequence. The simple expression for the blue sideband Rabi frequency $\Omega_{n,n-1} = \Omega\eta\sqrt{n}$ is not valid outside the Lamb-Dicke limit, which typically corresponds to the tail end of the Doppler thermal distribution we are trying to cool. For this reason, the exact expression for the blue sideband Rabi frequencies involving Laguerre polynomials (Eq.
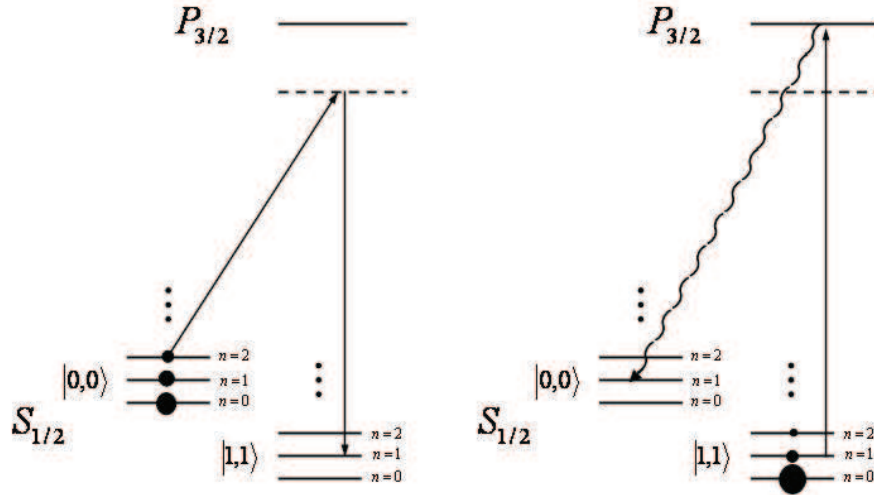
Figure 6.4: Schematic diagram depicting a single Raman cooling cycle. The Doppler-cooled thermal state is initialized to $|\uparrow\rangle$. Then a blue sideband resonant with the $|\uparrow, n\rangle \to |\downarrow, n-1\rangle$ transition reduces the motional kinetic energy by $\hbar\omega_x$. The internal state population is recycled to the $|\uparrow\rangle$ state by applying the optical pumping beam for ~ 5 μs. This process is repeated many times until the motional ground state $|n = 0\rangle$ is reached.
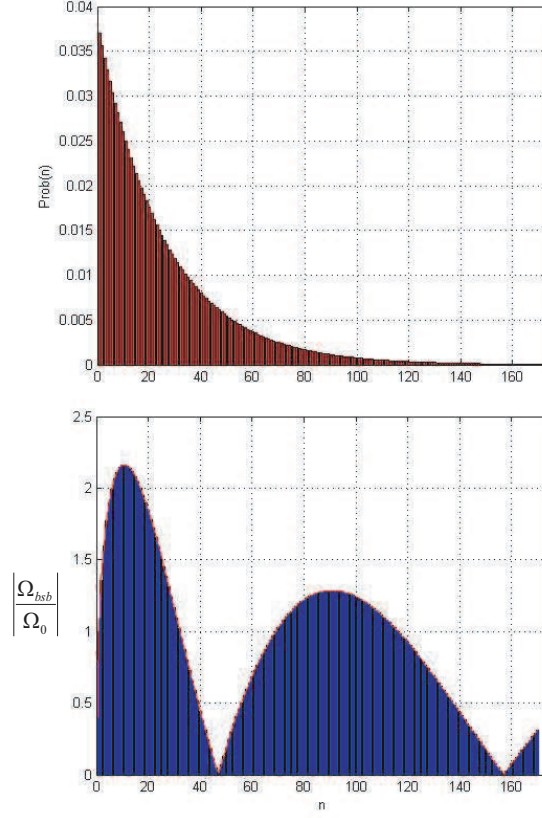
Figure 6.5: Plot of (a) the thermal distribution of motional levels with $\langle n_D \rangle$=30 following a Doppler cooling stage, and (b) the normalized first blue sideband strength (relative to the copropagating carrier Ω_0). These plots were calculated with $\omega_x/2\pi$ =1 MHz and η =0.28. Note that the strength of the blue sideband nearly vanishes at $n \simeq 46$, which results in ineffective Raman cooling for thermal distributions having significant population above $n \sim 46$.

Figure 6.6: Simulation results for Raman cooling to near the ground state of a large thermal distribution with $\langle n_D \rangle =30$ (as in Fig. 6.5). An adaptive Raman pulse sequence initially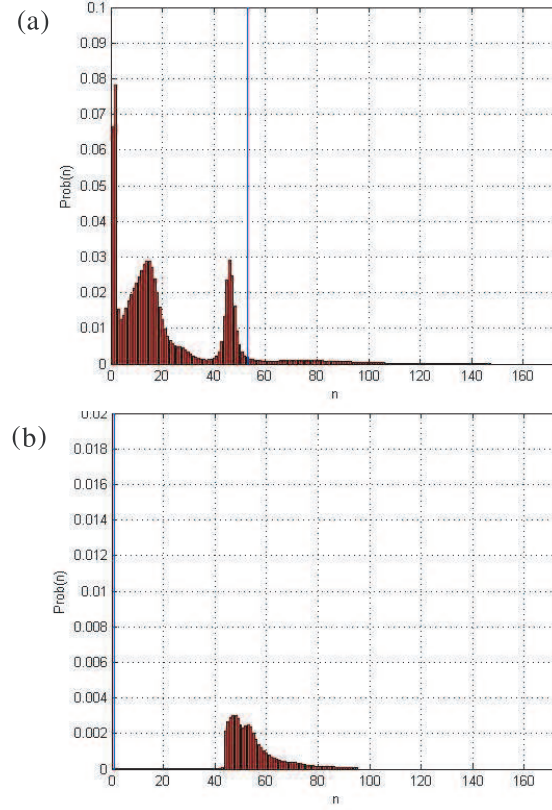 sets the blue sideband pulse length to correspond to a π-pulse for $n=75$ and subsequently adapts the length for lower n as the cooling process evolves. The simulation takes into account the effect of recoils from spontaneous emission and assumes a motional heating rate of .05 quanta/ms. The thermal distribution is shown in (a) after 24 Raman cooling cycles (starting at $n=75$). Note the peak in the population at $n \simeq 46$, which corresponds to the null in the blue sideband strength as shown in Fig. 6.5. The thermal distribution after 75 cooling cycles, a near-complete cooling process, is shown in (b). The population which could not be cooled past $n \simeq 46$ remains, though this is small compared to the >99% ground state population.

3.33) is used to calculate the Raman pulse times. Here, there is a little inconsistency in having the ground state Rabi frequency as an input parameter for the Raman cooling schedule. Typically, we get around this by making an initial guess for the π-pulse time of the blue sideband in the ground state, and iteratively we change the value until the cooling is optimal. In the laboratory we observe that for larger thermal distributions corresponding to trap frequencies below $\sim$1.3 MHz, ground state Raman cooling fails [18]. This is presumably due to nulls in the first blue sideband and recoils from spontaneous emission, as discussed in Fig. 6.6.

Fig. 6.3 shows a Raman spectra for the red and blue sidebands for both the (a) Doppler cooling and with subsequent (b) Raman cooling in the ring-and-fork trap with $\omega_x/2\pi = 5.8 MHz$ ($\eta_x \simeq 0.12$). The change in the sideband asymmetries indicates cooling from approximately $\langle \hat{n}_D \rangle \simeq 5(3)$ to $\langle \hat{n}_{Raman} \rangle \simeq 0.03(2)$, corresponding to a probability $P_0 \simeq 97\%$ of ground state occupation. No further cooling is observed when more than about 40 Raman cooling cycles are used, and the results were found to be largely independent of the details of the Raman cooling schedule. For instance, a uniform setting for the Raman cooling sideband pulse works nearly as well as the adaptive pulse schedule. Similar results are observed in both the quadrupole and the linear traps for various frequencies between 1.3 MHz to 5.8 MHz. For instance, in the linear trap with $\omega_x/2\pi = 2.69$ MHz ($\eta_x \simeq 0.17$), we reach a probability $P_0 \simeq 83\%$ of ground state occupation, requiring no more than 90 Raman cooling cycles.

6.3   Sympathetic cooling

This section describes the demonstration of sympathetic cooling on a small ion crystal. The need for sympathetic cooling stems from the fact that direct laser cooling of the qubit ions is not generally possible without disturbing/destroying the internal qubit coherence. An illustrative example where the use of sympathetic cooling is necessary is when ions are non adiabatically shuttled between different trapping regions [38, 27] as proposed in most large-scale quantum computing schemes [36, 69, 26, 70], their motion must then be re-cooled for subsequent logic operations. Furthermore,

sympathetic cooling of the motion of the ion crystal (quantum data bus) during computation can help to eliminate decoherence due to motional heating of the ion crytal caused by noisy background electric fields [26, 18].

As mentioned above, in order to preserve the internal qubit state coherence, it is generally not possible to directly laser cool the motion of the qubit ions. Instead additional "refrigerator" ions in the crystal can be directly laser cooled, with the qubit ions cooled in sympathy by virtue of their Coulomb-coupled motion [71]. The laser cooling of the refrigerator ions can quench unwanted motion of the ion crystal, while preserving the internal electronic coherence of the qubit ions [36, 72, 73]. Before our demonstration of sympathetic cooling in 2001, this cooling scheme had been observed in several systems: large ensembles of ions in Penning traps [71, 74], and small ion crystals consisting of a single species, where strong laser focusing was required to access a particular ion (refrigerator) without affecting the other (qubit) [75]. The experiment described in this thesis was the first demonstration of sympathetic cooling in a small ion crystal with two different species where both species are independently optically addressed. It should be noted that since then, an experiment was performed by the group at NIST where they also demonstrated the cooling of a two species ion crystal, but this time, consisting of two different atomic species: a ^{9}Be$^+$ and a ^{24}Mg$^+$ ion [76]. The advantage of using different atomic species for the qubit (^{9}Be$^+$) and the refrigerator (^{24}Mg$^+$) ion has the obvious advantage of completely isolating the qubit ion from the cooling laser only resonant with the refrigerator ions. The disadvantage however, comes in the added laser system needed to directly cool the ^{24}Mg$^+$. The Cadmium ion offers a distinct advantage with the many isotopes that are readily available (section 2.1). For instance when using the ^{111}Cd$^+$ ion as the qubit and ^{116}Cd$^+$ ion as the refrigerator ion, the isotope shift between these two species is $\Delta/2\pi \simeq 5.2$ GHz. It is large enough to neglect qubit decoherence from spontaneous emission and AC stark shifts of the qubit ion originating from the cooling laser applied to the refrigerator ion (^{116}Cd$^+$), yet the isotope shift is small enough so that optical modulators can provide the cooling radiation without the need for additional laser sources.

In the experiment presented here, we sympathetically cool the motion of a ^{112}Cd$^+$ ion by directly laser cooling a refrigerator ion (^{114}Cd$^+$) – both isotopes have zero nuclear spin. Specifically, the refrigerator ion is continuously Doppler-cooled by a laser beam red detuned from its D2 line ($S_{1/2} - P_{3/2}$), while the other isotope (the qubit or probe ion) is either Doppler cooled or Doppler heated by another beam, whose frequency is scanned around its D2 resonance line. The effect of sympathetic cooling is to enable measuring fluorescence on the blue side of the probe ion's resonance. Ordinarily, when the probe laser beam is tuned to the blue of the probe ion's resonance, the ion ceases fluorescing due to Doppler heating, but the sympathetic cooling from the refrigerator ion keeps the probe ion cold and fluorescing regardless of the probe tuning. The respective D2 lines of these two neighboring isotopes are separated by 680 MHz (section 2.1), with the heavier ion at a lower absolute frequency, and the natural linewidth of each ion's excited $P_{3/2}$ state is $\gamma_0/2\pi \simeq 59$MHz.

6.3.1 Experimental apparatus

The experimental apparatus is schematically shown in Fig. 6.7. The resonant light with the Cd$^+$ D2 line near 214.5 nm is generated by a quadrupled narrowband Ti:Sapphire laser. The quadrupled UV output is split into two parts; one part is upshifted by ~ 420 MHz, while the other is downshifted by ~ 400MHz using acousto-optical frequency shifters. The two beams are then directed into the ion trap through separate viewports. both beams uniformly illuminate the ion crystal into the trap. The upshifted UV beam (probe beam) is scanned in frequency around the ^{112}Cd$^+$ ion's D2 line, while the downshifted UV beam (refrigerator ion) frequency is always kept to the red of the ^{114}Cd$^+$ ion's D2 line. The UV fluorescence from the ion is collected by an f/5.6 lens and imaged onto a microchannel plate detector. the fluorescence counts are integrated for 10 s for each data point in a frequency scan.

The experiment is carried out in the very first ion trap constructed in the Monroe lab - a standard 3D rf-quadrupole ring-and-fork Paul trap (trap 1 in section 1.2). The trap's rf drive frequency is $\Omega/2\pi \simeq 38.8$ MHz, and the secular frequency is $\omega_x/2\pi \simeq 2.8$

MHz, corresponding to an rf voltage amplitude of about 200 V. We set the trap's compensating electrode voltages such that the ^{112}Cd$^+$ (probe) ion is near the rf null of the trap to minimize its micromotion and thus avoid the influence of the micromotion on the line shape [77].

To study sympathetic cooling, we load a ^{112}Cd$^+$ ion and a ^{114}Cd$^+$ ion into the trap by directing ~ 1 mW of UV radiation focused to under 20 μm onto the trap electrodes, which have been previously coated with neutral cadmium. Presumably, the UV radiation ablates cadmium from the electrodes in ionic form. Due to the high abundance of isotopes 112 and 114 in neutral cadmium (24% and 29%, respectively), loading the proper two isotopes is not unlikely. This loading method now appears somewhat primitive in comparison to the photoionization loading scheme described in chapter 4 of this thesis.

6.3.2 Experimental results

In Fig. 6.8 the fluorescence of the ^{112}Cd$^+$ ion is plotted against the probe beam frequency. In Fig. 6.8(a) both the probe and the refrigerator laser beams are on, while for the data in Fig. 6.8(b) the refrigerator beam is turned off. Note the telltale drop in fluorescence as the probe beam is tuned to the blue side of the ^{112}Cd$^+$ resonance line in Fig. 6.8(b) is caused by Doppler heating. On the other hand, the fluorescence curve in Fig. 6.8(a) is symmetric, demonstrating that the ^{112}Cd$^+$ ion is sympathetically cooled by the ^{114}Cd$^+$ ion even as the probe beam is tuned to the blue of the resonance.

Images of the two ions at different lighting conditions are shown in Fig. 6.9; the probe ion (^{112}Cd$^+$) is on the left, while the refrigerator ion (^{114}Cd$^+$) is to the right. Both the probe and the refrigerator beams are turned on for Fig. 6.9(a). In Fig. 6.9(b) only the probe beam is turned on, while in Fig. 6.9(c) only the refrigerator beam is on. Note the very faint images of the ^{114}Cd$^+$ ion in Fig. 6.9(b) and the ^{112}Cd$^+$ ion in Fig. 6.9(c). These images originate from the residual fluorescence from the far-detuned beams.

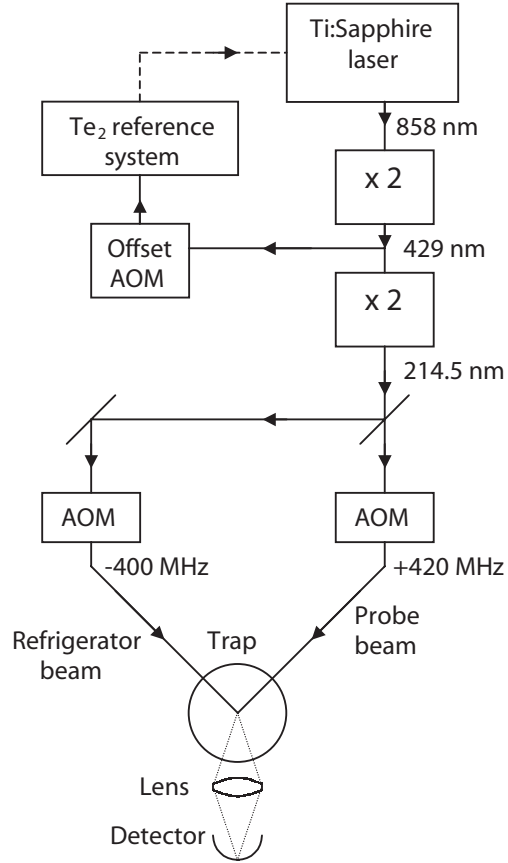**Figure 6.7**: Schematic diagram of the sympathetic cooling experiment. The 858 nm light from the Ti:Sapphire laser is frequency quadrupled to a wavelength of 214.5 nm with a typical optical power of ~15 mW. The UV beam is then split into two parts, each of which is frequency shifted by AOMs and directed into the trap. Note that the laser setup is described in greater detail in chapter 3 of this thesis.
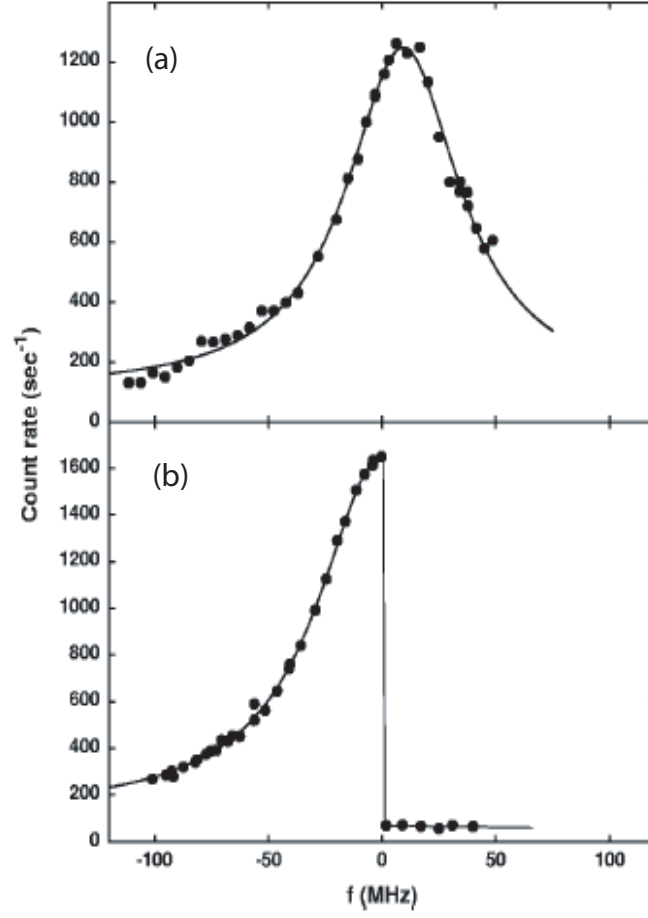
Figure 6.8: UV fluorescence count rate from the ^{112}Cd$^+$ probe ion (a) with and (b) without sympathetic cooling, plotted against the probe beam frequency detuning from resonance. Solid lines represent fits to the data using (a) a Voigt profile and (b) a Voigt shape for the below-resonance part of the data and a straight line for the above-resonance part of the data. The resonance is shifted about 10 MHz blue with respect to the resonance without. This shift is consistent with the expected ac stark shift of the ^{112}Cd$^+$ levels due to the off-resonant ^{114}Cd$^+$ cooling radiation.

For the data shown in Figs. 6.8 and 6.9, the probe beam intensity is $I_{probe}=0.35I_{sat}$, while the refrigerator beam intensity is $I_{ref}=12I_{sat}$, where the saturation intensity $I_{sat} \simeq 0.6\text{W/cm}^2$. Such high refrigerator beam intensity is necessary because of the large amount of refrigerator ion micromotion; recall that only the probe ion ($^{112}\text{Cd}^+$) is located at the rf null of the trap. The effect of micromotion is a broadening of the line shape of the refrigerator ion, which reduces the efficiency of Doppler cooling [28]. The shift of the probe ion resonance line in Fig. 6.8(a) by about 10 MHz compared to Fig. 6.8(b) is consistent with the ac Stark shift induced by the off resonant refrigerator beam.

To demonstrate that the cooling seen in Fig. 6.8(a) is not caused by directly Doppler cooling the $^{112}\text{Cd}^+$ probe ion by the refrigerator beam (which indeed is red detuned from the $^{112}\text{Cd}^+$ ion's D2 line) we load a single $^{112}\text{Cd}^+$ ion into the trap, while shining both the refrigerator and the probe beams onto the ion. The curve in Fig. 6.10 shows the resulting fluorescence as a function of the probe laser frequency. When tuned to the blue of the resonance, the ion's fluorescence quickly drops to zero, indicating that the ion is heated by the probe beam; the direct Doppler cooling by the far-detuned refrigerator beam is not sufficient to keep the ion cold.

In conclusion, we have sympathetically cooled a single trapped $^{112}\text{Cd}^+$ ion via Doppler cooling of a neighboring $^{114}\text{Cd}^+$ ion. This, at the time, was the first demonstration of optically addressing a single trapped ion being sympathetically cooled by an ion of a different species. The sympathetic cooling of multiple ion species is an important step toward scaling the trapped ion quantum information processor, as it can reduce decoherence associated with unwanted motion of trapped ions, while preserving the internal qubit coherence. The Cd^+ system is convenient, as the sympathetic cooling can be accomplished without extra lasers and without strong focusing.
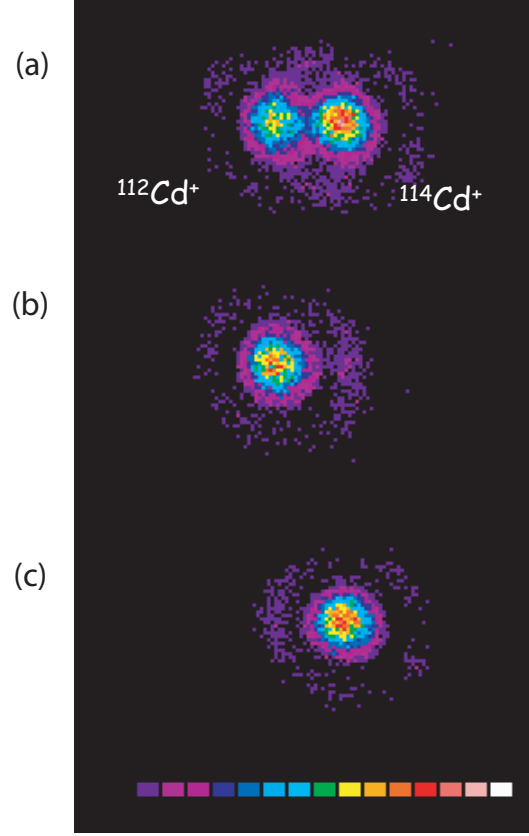
Figure 6.9: Images of the ^{112}Cd$^+$ and ^{114}Cd$^+$ ions while illuminated by (a) both the refrigerator and the probe beam, (b) only the probe beam, and (c) only the refrigerator beam. The ^{112}Cd$^+$ ion is on the left, while the ^{114}Cd$^+$ ion is on the right. The 2 ions are separated by 2$\sim\mu$m. Note very faint images of the ^{114}Cd$^+$ ion in (b) and the ^{112}Cd$^+$ ion in (c) from the residual fluorescence from far detuned beams, partially obscured in this picture by the Airy rings. The scale below is linear in the integrated photon counts. The exposure time is 10 sec. for each picture.

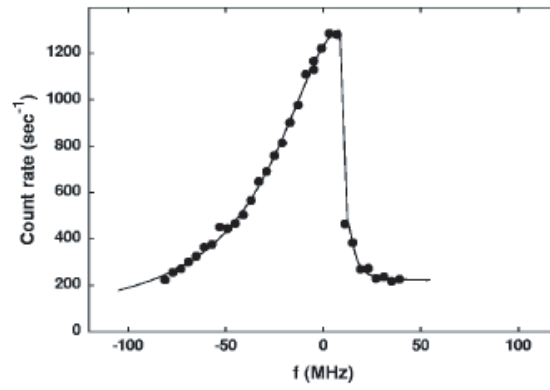**Figure 6.10**: UV fluorescence from a single ^{112}Cd$^+$ ion while illuminated by both the refrigerator and the probe beam, plotted against the probe beam detuning from the resonance. The solid line is a Voigt fit to the data below the resonance and a hand-drawn curve above the resonance.

CHAPTER 7

Investigation of motional heating in ion traps

An important source of decoherence in the trapped ion system is the heating of trapped ion motion, arising from noisy electrical potentials of unknown origin on the trap electrode surfaces [36, 26, 18]. This decoherence is expected to become even more critical as ion traps become weaker in order to support larger ion crystals [20], and allow shuttling of ions through complex and microscale electrode structures [70, 78, 27, 38, 68]. In a more general view, the anomalous heating of trapped ions from electrode surface noise may also be related to parasitic electrical noise observed in many condensed-matter quantum systems such as Cooper-pair boxes [79] and Josephson junctions [80].

In this chapter, I first summarize the motional heating measurements that have been made so far by several trapped ion groups worldwide. The various heating measurements in the Cd^+ ion system are also presented along with the technique used to quantify this heating. Then I discuss two models for the source of motional heating: namely, thermal (Johnson) noise and "patch" potential noise. Finally, I present the results of a controlled study of the character of trapped ion motional decoherence in a novel trapping geometry (two-needle) that permits the electrode spacing to be adjusted *in situ*. Measurements of motional decoherence at varying distances between the ion and the electrodes allow some characterization of the spatial extent of noisy patch potentials [81] on the electrodes. In addition, the electrodes in this apparatus can be cooled through contact with a liquid nitrogen reservoir. When the temperature of the electrodes is reduced from 300 K to about 150 K, the anomalous heating rate of trapped ion motion drops by an order of magnitude or more, but is still higher

than that expected from thermal (Johnson) noise in the electrical circuit feeding the electrodes. This provides direct evidence that anomalous heating indeed originates from the electrode surfaces and can be significantly suppressed by modest cooling of the electrodes.

7.1   History of heating measurements in ion traps

The first observation of anomalous motional heating occurred in 1989 by the NIST research group [15]. This was the first time a trapped ion was cooled to its motional ground state, which is one of the main requirements of the thermometry technique discussed in section 3.3.3[1]. The heating rate was measured to be orders of magnitude above what is expected from thermal noise which originates from resistances in the trap electrodes (discussed in more detail in the next section). In fact, the time for the motion to increase by one quanta was expected to be 95 hours, which is orders of magnitude from the measured heating rate of 6 quanta/sec. The next heating measurement was made in 1995, again in the NIST group with Be^+, where they observed a larger heating rate of 1 quanta/msec. This increase in the heating rate as compared to the 1989 Hg^+ ion experiment was the first observation of the strong dependence of the heating rate on the ion-electrode distance. From there on, every ion trap having the capability to laser cool the motion to its ground state produced a new heating data point. A plot of the various heating measurements vs ion-electrode distance are shown in Fig. 7.1. These include other ion species such as $^{137}Ba^+$ [40], $^{40}Ca^+$ [17, 78], and $^{111}Cd^+$ [18]. Included in the Be^+ data are 3 data points from an experiment reported in 2002 [27] which observed a correlation between electrode surface purity and smoothness and the ion heating rate. Trap electrodes that were electroplated with gold were observed to have a lower heating rate than electrodes that were coated with gold evaporation. The heating rate was also observed to increase within the first few weeks of operation, indicating that the surface layer of Be (from

---

[1] The sensitivity of this technique is at a maximum for $\bar{n} \sim 1$ and quickly diminishes as $\bar{n}$ approaches ~ 10.

firing the Be oven) coating the electrodes caused the heating. In the ^{137}Ba$^+$ [40] experiments a gradual degradation of trap stability as the electrodes became coated with Ba was also observed.
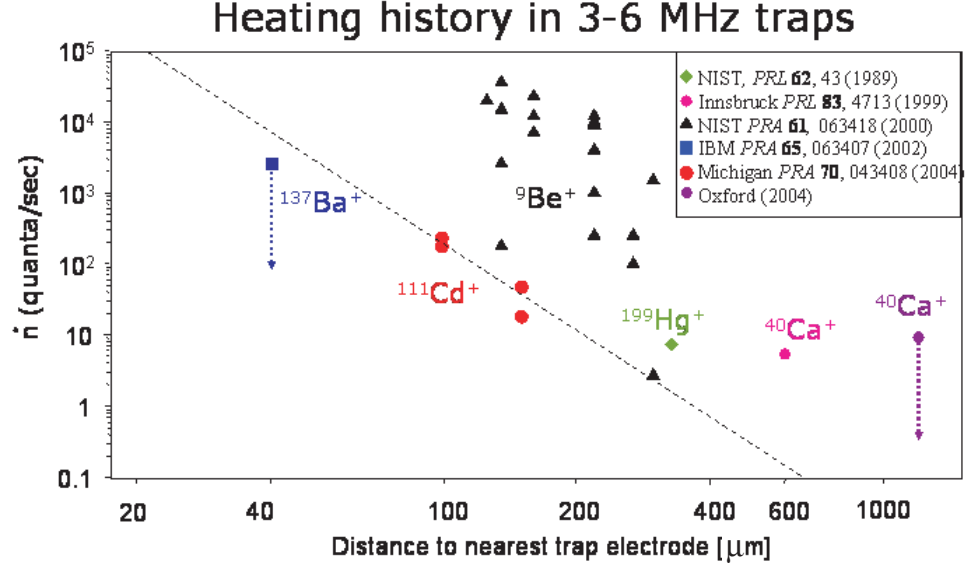

Figure 7.1: Observed heating rate $\dot{n}$ vs ion-electrode distance d observed by research groups worldwide. The heating measurements shown here are for trap frequencies between 2.9 MHz and 6.0 MHz. The dashed line is a guide to the eye for the $1/d^4$ scaling of the heating rate predicted by a model of microscopic potential fluctuations [26].

The results for ^{111}Cd$^+$ (red points on the graph) were taken from experiments performed in both the ring-and-fork trap and also the three-layer linear trap (sections 2.2.1 and 2.2.2). The measured heating rates were observed to be slightly lower than what is expected from the trend in Fig. 7.1, but still much higher than what is expected from thermal noise. The heating rates were measured using the previously mentioned sideband thermometry technique with different delay times (with no laser interaction) between the ground state cooling and the temperature measurement. These measurements of $\bar{n}$ are repeated with increasing time delay until a heating rate can be extracted. An example of data from the quadrupole trap ($\omega_x/2\pi = 5.8$ MHz) is shown in Fig. 7.2, where a linear fit of the data ($\bar{n}$ vs time delay) yields a heating

rate of $\dot{\bar{n}}$= 0.0248(3) quanta/msec. Fig. 7.3 displays a series of measured heating rates in the two traps as a function of the trap frequency ω_x. In the quadrupole trap, ω_x is varied by changing the rf voltage V_0 and/or the static voltage U_0, whereas in the linear trap, ω_x is varied by adjusting only the static potentials on the electrodes.
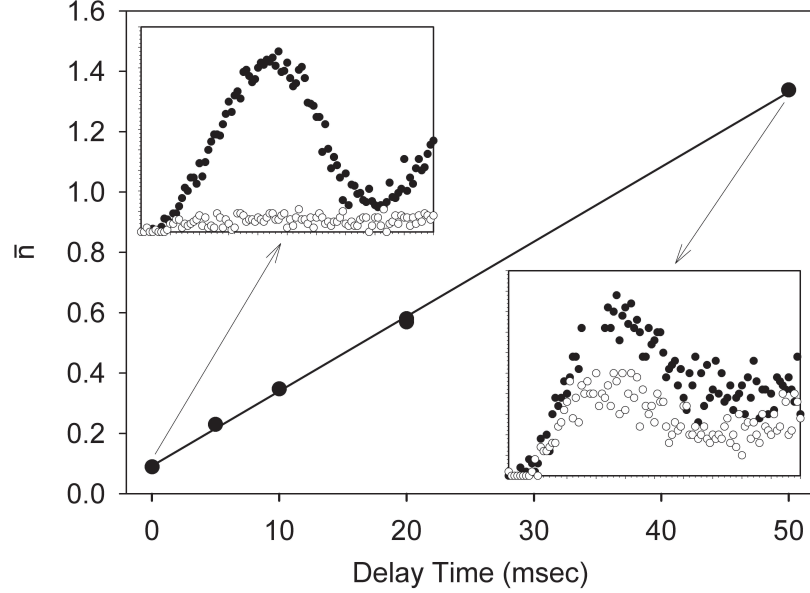

Figure 7.2: An example of heating data taken in the quadrupole trap, with a trap frequency of $\omega_x/2\pi$=5.8 MHz. Mean motional quanta $\bar{n}$ is plotted vs time delay. The insets show sideband Rabi oscillations from which $\bar{n}$ is inferred; the black points represent the first red sideband and the open points represent the first blue sideband. The solid line is a linear fit to the data from which a heating rate of $\dot{\bar{n}} \approx 0.0248(3)$ quanta/msec is obtained.

The experiments listed in Fig. 7.1 allow us to make some weak conclusions about the characteristics of the anomalously large heating rates observed in all trapped ion systems. First, according to Fig. 7.1, the heating rate has a stronger scaling with ion-electrode distance than what is expected from thermal (Johnson) noise, which should scale as $1/d^2$ (explained in detail in the next section). In addition, the source of the noise seems to be located at the electrodes, and not electric field noise from outside laboratory sources. It should be clear, however, that the main cause of this heating is still not well understood. This lack of understanding is the

motivation for our experiments with the needle trap which allows to vary the ion-electrode distance and electrode temperature *in situ*. This is the first experiment to allow the controlled-adjustment of the trap dimensions and temperature. These experiments will be presented in the next sections, following a theoretical discussion of the models of thermal and patch potential noise.
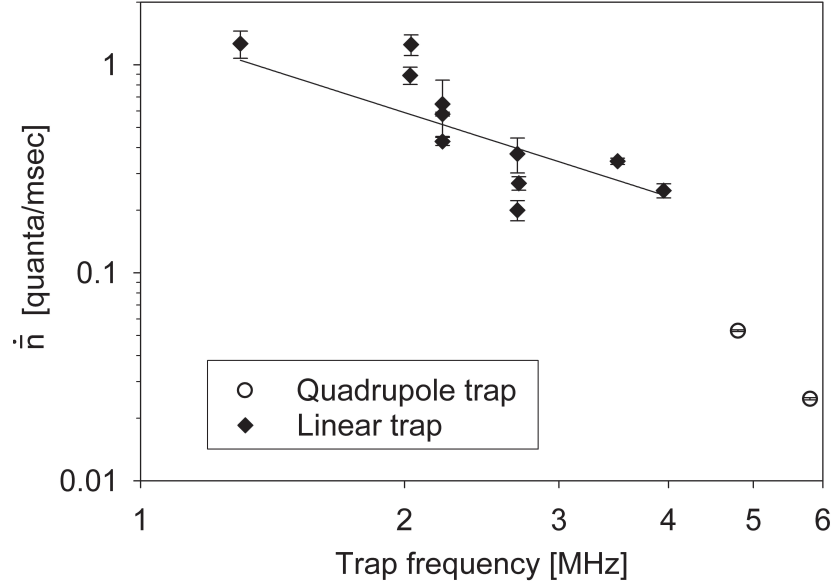
Figure 7.3: Observed heating rates $\dot{\bar{n}}$ vs trap frequency in the ^{111}Cd$^+$ ion system. The solid line is a fit to the heating rates in the linear trap where the rf electrode voltage V_0 is constant. The fit to the data in this trap shows a trap frequency scaling of $\omega_x^{-1.4}$, yielding a frequency dependence for the spectral density of electric field noise of $S_E(\omega) \propto \omega^{-0.4}$. The error bars represent the statistical noise in the linear regression from which a heating rate is inferred (as shown in Fig. 7.2). The heating measurements were taken over a period of five months in the quadrupole trap and two months in the linear trap.

7.2 Sources of motional decoherence

A single trapped ion is heated when noisy electric fields at the ion's position couple to its charge. These fluctuating forces are particularly effective at imparting energy when the frequency of the noise corresponds to the trap secular frequency or its micromotion sidebands. For the origin of the motional heating, we distinguish between two sources of noise: thermal (Johnson) noise and patch potential noise. The motion can also be heated through various other mechanism, such as electronic voltage noise from lab equipment, ion collisions with background atoms, and field emitter points on trap electrodes, to name a few. The research group at NIST did an extensive study which ruled out all of these as significant sources of noise [36, 26], justifying the focus on thermal and patch potential noise.

In order to determine the heating rate arising from electric field fluctuations at the trapped ion's position, consider the Hamiltonian for an ion confined in a harmonic well subjected to the noisy field $E(t)$, given by

$$\hat{H}(t) = \frac{\hat{p}_x^2}{2m} + \frac{1}{2}m\omega_x^2\hat{x}^2 - eE(t)\hat{x}. \tag{7.1}$$

Here $E(t)$ represents the x-component of the fluctuating electric field at the center of the trap. From first-order perturbation theory [52], the average rate at which an ion initially in the state $|n, t = 0\rangle$ makes a transition to the state $|m \neq n\rangle$ in a time T is expressed as

$$\Gamma_{m\leftarrow n} = \frac{1}{T}\left[\frac{-i}{\hbar}\int_0^T dt' \left\langle m\left|\hat{H}'(t')\right|n\right\rangle e^{i\omega_{mn}t'}\right]\left[\frac{i}{\hbar}\int_0^T dt'' \left\langle m\left|\hat{H}'(t'')\right|n\right\rangle e^{-i\omega_{mn}t''}\right]. \tag{7.2}$$

Inserting the expression for the perturbation $\hat{H}'(t) = -eE(t)\hat{x}$ in Eq. 7.2 and rearranging the integrals yields

$$\Gamma_{m\leftarrow n} = \frac{e}{\hbar^2 T}\left[\int_0^T\int_0^T dt'dt'' \left|\langle m\left|\hat{x}\right|n\rangle\right|^2 E(t')E(t'')e^{i\omega_{mn}(t'-t'')}\right] \tag{7.3}$$

$$= \frac{e^2}{\hbar^2}\left|\langle m\left|\hat{x}\right|n\rangle\right|^2 \int_{-\infty}^{\infty} d\tau e^{i\omega_{mn}\tau}\left\langle E(t)E(t+\tau)\right\rangle. \tag{7.4}$$

Here, we assumed that the time over which the motional state population varies is longer than the averaging time T, and that the correlation time of the fluctuating

electric field $E(t)$ is short compared to time T. This allows us to extend the limits of integration for the time delay τ to $\pm\infty$. We identify the expression for the spectral density of electric field noise as

$$S_E(\omega_x) \equiv 2 \int_{-\infty}^{\infty} d\tau e^{i\omega_x \tau} \langle E(t)E(t+\tau) \rangle, \tag{7.5}$$

with units of $(\mathrm{V/m})^2 \mathrm{Hz}^{-1}$. This expression is reminiscent of the relationship between the self coherence function of a light source, typically written as $\Gamma(\tau) = \langle E(t+\tau)E(t) \rangle$, and its power spectral density [82]. In the case of the Michelson interferometer, the time delay at which the interference fringe contrast at the output diminishes to half of its zero time delay value allows one to determine the power spectrum of the light source.

Since the heating rates are typically measured from the motional ground state, the transition rate from the ground state $|n=0\rangle$ to the first excited state $|n=1\rangle$ is

$$\Gamma_{1\leftarrow 0} = \frac{e^2}{2\hbar^2} |\langle 1 |\hat{x}| 0 \rangle|^2 S_E(\omega_x). \tag{7.6}$$

Inserting the matrix element $|\langle 1 |\hat{x}| 0 \rangle|^2 = x_0^2 = \hbar/2m\omega_x$ yields a simple form for the heating rate, given by

$$\dot{n} \equiv \Gamma_{1\leftarrow 0} = \frac{e^2 S_E(\omega_x)}{4m\hbar\omega_x}. \tag{7.7}$$

In general, for an ion confined in a combination of static and rf fields, the motion of the ion has additional components[2] at frequency $\omega_{rf} \pm \omega_x$. The electric field noise at these frequencies can also couple to the ion motion at frequency ω_x, and therefore contribute to the motional heating [36, 26]. Taking this into account, the generalized heating rate $\dot{n}$ reads

$$\dot{n} = \frac{e^2}{4m\hbar\omega_x} \left(S_E(\omega_x) + \frac{\omega_x^2}{2\Omega_{rf}^2} S_E(\Omega_{rf} \pm \omega_x) \right). \tag{7.8}$$

The coefficient in front of the second term in Eq. 7.8 ($\omega_x^2/2\Omega_{rf}^2 \sim 10^{-3}$) is often small enough to justify neglecting the rf heating contribution altogether. However, the presence of the resonator with a resonance frequency at Ω_{rf} and quality factor Q

---

[2]A notable exception is the longitudinal confinement in a linear trap, which originates from applied static fields (section 2.2.2).

can sometimes amplify this source of noise to an appreciable level. But again, in order to reduce the rf pick-up, the trap electrodes typically have low-pass filters attached to them which filter most of this rf noise. This was the situation for the two-needle trap (discussed below).

Thus, in order to calculate the expected heating rate $\dot{\bar{n}}$ for a ion confined in a trap with frequency ω_x, we need a knowledge of the fluctuating electric field, specifically the spectral density of electric field $S_E(\omega_x)$ at the ion position. In principle, if we could directly measure $S_E(\omega_x)$ with a probe, the expected ion heating rate could be calculated exactly. However, the best probe to measure this quantity (actually the only probe) is the ion itself. Thus, to calculate the expected heating rate, we need to consider a model for each source of electric field noise at the ion position. In the next two sections, I discuss the models for the thermal and patch potential noise and give expressions for the spectral density of electric field noise in each case.

7.2.1   Heating rate for thermal (Johnson) noise

Quantifying the spectral density of electric field noise at the center of the trap due to thermal (Johnson) noise is greatly simplified by the fact that the wavelengths associated with the thermal radiation (at typical trap secular or drive frequencies) are much larger than the resonator+trap electrodes setup. This allows one to describe the distributed electrode resistance, capacitance, and inductance by an equivalent RLC circuit with discrete elements [83, 84, 36]. The effective lumped-circuit resistance R gives rise to a voltage noise on the electrode given by $S_V(\omega_x) = 4k_B T R(\omega_x)$ [85, 26], where k_B is the boltzmann constant, and T is the temperature of the electrode (typically at 300K). The resulting spectral density of electric field noise at the trap center is given by

$$S_E(\omega_x) = \epsilon^2 \frac{4k_B T R(\omega_x)}{d^2},\tag{7.9}$$

where d is the distance from the ion to the trap electrode, and ϵ is a geometrical efficiency factor that relates a given potential difference across the noisy electrode and the grounded electrodes to the resulting electric field at the trap center. For

instance, a parallel plate capacitor has an efficiency factor $\epsilon=1$. Fig. 7.7 shows the results of a simulation for the efficiency factor in the needle trap, giving a value of $\epsilon = 70\%$ over the range of needle spacings used in the experiment.

As mentioned earlier, estimates of this heating consistently lead to values that are orders of magnitude lower than what is observed by all trapped ion research groups. In order for thermal noise to be the source of the anomalously large heating rates, an electrode temperature on the order of $\sim 10^6$ K would be required! The simplicity of Eq. 7.9 can be misleading. In general, to estimate the ion heating due to thermal noise, the trap electrode geometry, rf filtering characteristics, and resonator type must be included in the analysis. As an example, in the case of the ring-and-fork trap (section 2.2.1) with symmetrically aligned electrodes, a voltage noise at the fork or ring electrode results in a null electric field at the ion position, which further reduces the heating rate predicted by Eq. 7.9. Another good example of these considerations is provided below in the results section, where I describe the calculation of thermal noise estimation for the two-needle trap experiment.

7.2.2   Heating rate for uncorrelated fluctuating patch-potential noise

The term "patch-potential" noise is used to cover many different mechanisms, such as randomly oriented domains at the surface of the electrodes or adsorbed materials on the electrodes [26]. Static patch potentials are a well known source of noise in experiments sensitive to noisy static electric fields, such as Rydberg atoms in cavities [86] and charged particles in drift tubes [81, 87]. On the other hand, little is known about fluctuating patches in the MHz frequency range, which is required to account for this anomalous heating [88, 89, 81]. An observation supporting the model of localized voltage patches is that the heating rate as a function of ion-electrode distance d scales more strongly than what is expected from correlated voltage noise (i.e. thermal noise) across the whole electrode structure ($\sim 1/\mathrm{d}^2$).

The following is a derivation of the spectral density of electric field noise at the ion position caused by patch potentials. We define the x-component of the electric field

at the trap center from the n-th patch to be $E_n(s,t) = V_n(t)\xi_n(s)$, where $\xi_n(s)$ can be thought of as the electric field at the ion per unit voltage on the patch at a distance s away. Here the time dependence is associated with the patch voltage only. In order to get the total electric field at the ion position we must add the contributions from all patches, which gives $E_{Total} = \sum_{n=1}^{N(s)} V_n(t)\xi_n(s)$. Inserting this expression into Eq. 7.5 yields

$$S_E(\omega_x) = 2\int_{-\infty}^{\infty} d\tau e^{i\omega_x \tau} \left\langle \sum_{n=1}^{N(s)} V_n(t)\xi_n(s) \sum_{m=1}^{N(s)} V_m(t+\tau)\xi_m(s) \right\rangle \qquad (7.10)$$

$$= 2\sum_{n=1}^{N(s)}\sum_{m=1}^{N(s)} \int_{-\infty}^{\infty} d\tau e^{i\omega_x \tau} \xi_n(s)\xi_m(s) \left\langle V_n(t)V_m(t+\tau) \right\rangle \qquad (7.11)$$

Assuming the fluctuating voltage noise $V_n(t)$ for different patches is uncorrelated, a single sum remains, giving

$$S_E(\omega_x) = 2\sum_{n=1}^{N(s)} [\xi_n(s)]^2 \int_{-\infty}^{\infty} d\tau e^{i\omega_x \tau} \left\langle V_n(t)V_n(t+\tau) \right\rangle \qquad (7.12)$$

$$= 2\left(\sum_{n=1}^{N(s)} [\xi_n(s)]^2\right) S_V(\omega_x) \qquad (7.13)$$

where $S_V(\omega_x)$ is the spectral density of voltage noise on each patch.

The above expression is useful in that it shows how $S_E(\omega_x)$ can be separated into a product of a geometrical factor and $S_V(\omega_x)$. Solving for the geometrical factor typically requires a complicated calculation, and depends on the particular electrode geometry and the size and distribution of patches. However, useful insights can be gained by considering a few simple electrode geometries. For instance, following the derivation in Turchette *et.al.* [26], we can get an expression for $S_E(\omega_x)$ for the special case of a closed spherical electrode of radius d. Consider a patch of radius $r_p \ll d$ with spectral density of voltage noise $S_V(\omega_x)$ that is located on the inner surface of the sphere. The electric field noise per unit volt from the n-th patch is given by $\xi_n(d) = -3r_p^2 \cos\theta/4d^3$, where θ is the angle between the x-axis and the line joining the n-th patch to the ion at the center of the sphere. Assuming a patch coverage C, where $0 \le C \le 1$, the total number of patches $N(d)$ contributing to an electric field

noise at the trap center is $N(d) = 4Cd^2/r_p^2$. Inserting these expressions into Eq. 7.13 and averaging over the angle θ, we recover the result in [26] given by

$$S_E(\omega_x) = \frac{3Cr_p^2}{2}\frac{S_V(\omega_x)}{d^4}. \tag{7.14}$$

As previously mentioned, the introduction of localized voltage patches does result in a stronger heating rate dependence on the ion-electrode distance ($\dot{n} \propto 1/d^4$) than what is expected from thermal (Johnson) noise (i.e. $1/d^2$) [26]. When considering more realistic electrode geometries such as the two-needle trap, the geometrical factor in Eq. 7.13 is very difficult to calculate. However, the heating rate measurements described below for the two-needle trap yields an unambiguous scaling law.

7.3 Experimental apparatus

The two-needle trap electrode geometry, built for measuring motional heating, is depicted in Fig. 7.4. This cylindrically symmetric ($\alpha = 1/2$) rf Paul trap is formed by two opposing tungsten needle-tipped electrodes, mounted on independent translation stages allowing for the tip-to-tip electrode separation $2z_0$ to be controllably varied over a wide range $0 \leq 2z_0 \leq 1$ cm with micrometer resolution. The needles are also aligned to be co-axial with transverse translation stages, again with micrometer resolution. An electrical rf voltage $U_0 + V_0 cos(\Omega_{rf}t)$ is applied to each electrode with respect to a pair of recessed grounded sleeves surrounding the needles. The tungsten needle tip is approximately spherical with a 3 μm radius and it is supported by a conical shank with a half-angle of 4 degrees. The potential is delivered through a dual (bifilar) rf resonator (section 2.3.3), allowing the two electrodes to be independently biased with static voltages. This arrangement gives the ability to cancel static background electric fields pointing along the z-axis. Two additional electrodes (not shown in Fig. 7.4) are located a distance of $\sim$7 mm away from the trap center, allowing for the cancellation of stray electric fields along the transverse x-y directions.

Each sleeve electrode is machined from a single piece of aluminum. The sleeve's extremity consists of a hollow cylinder with a length of 1 cm, and a 3 mm inner
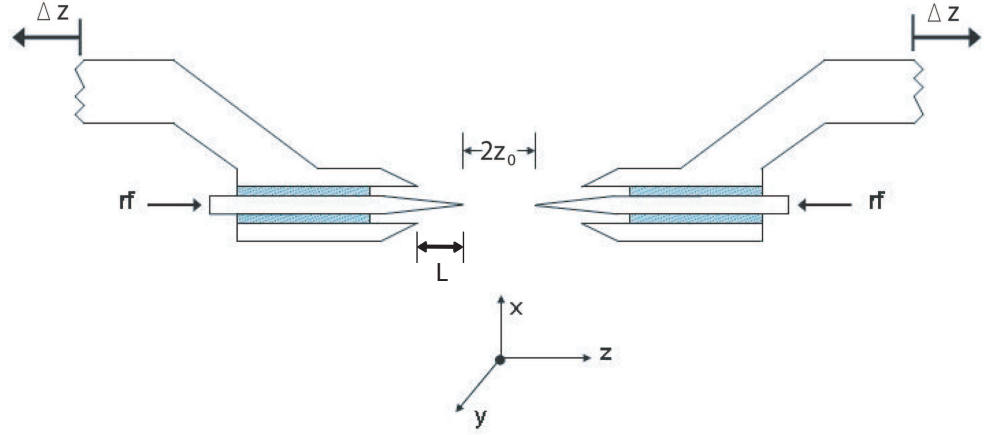
Figure 7.4: Schematic diagram for the electrodes of the needle trap. The needle trap is formed by two opposing tungsten needle-tip electrodes. The electrodes are mounted on independent translation stages, allowing the tip-to-tip electrode separation $2z_0$ to be controllably varied between $0 \leq 2z_0 \leq 1$ cm. An electrical potential $U_0 + V_0 \cos(\Omega_{rf} t)$ with frequency $\Omega_{rf}/2\pi$=29 MHz is applied to each electrode with respect to a pair of recessed grounded sleeves (aluminum) surrounding the needles. The sleeve and the needle electrodes are separated by a gap of 1 mm; the space is filled with an alumina tube, press-fit in place. An independent static voltage is applied to each needle, allowing for compensation of stray background $\vec{E}$-field along the z-axis. Compensation along the x-y directions is obtained by applying static voltages to two auxiliary electrodes (not shown in figure) positioned $\sim$7 mm away from the trap center. The tungsten needle tip is approximately spherical with a radius of $\sim$3 μm, and the needle shank recedes with a cone half-angle of approximately 4 degrees. The horizontal distance L from needle tip to the nearest rf ground (sleeve) is 2.3 mm.
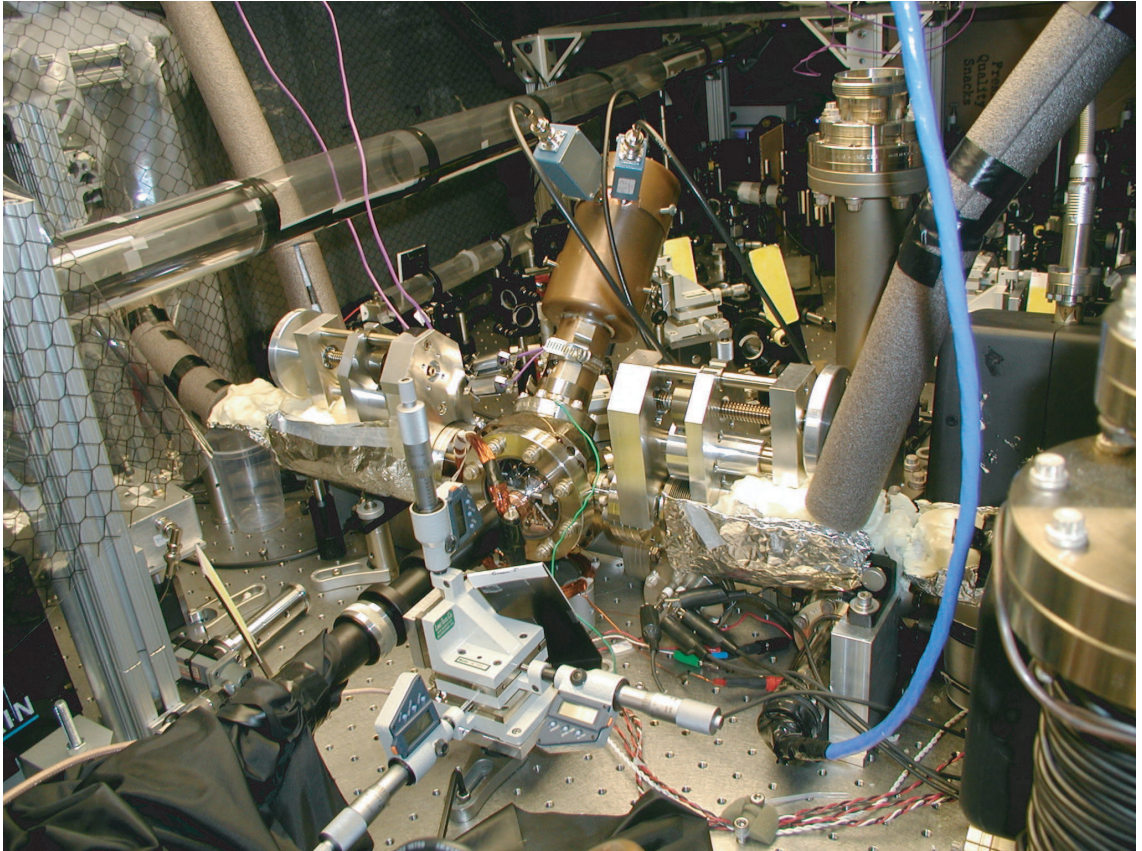
Figure 7.5: A picture of the experimental apparatus used to investigate motional heating.

and 5 mm outer diameter. The distance L between the sleeve's extremity and the needle tip is 2.4 mm. The space between the needle and the sleeve electrode is filled with an alumina tube, press-fit in place. The alumina tube serves two main purposes: to electrically insulate the sleeve from the needle electrode and to provide thermal contact between the sleeve and the needle. The trap apparatus also allows the temperature of both electrodes to be cooled down near liquid nitrogen (LN2) temperature (77 K). This is achieved by bringing a liquid nitrogen reservoir in thermal contact with the sleeve, which in turn, is in thermal contact with the needle via the alumina spacer. Fig. 7.6 describes in detail the LN2 setup.

The experiment conducted in the needle trap used a tip-to-tip needle distance $2z_0$ ranging from 75 μm to 500 μm, which required a large voltage efficiency factor ϵ in order to maintain a reasonable trap depth over this range. This along with other experimental constraints required running a substantial number of simulations in order to obtain the optimal sleeve and needle electrode configuration giving the maximum voltage efficiency factor ϵ. Most of these simulations were done using the 3-D electrostatic finite element analysis software *Maxwell*[3]. An electrostatic simulation may seem irrelevant when dealing with a radiofrequency Paul trap, but it turns out that in order to obtain the pseudo-potential seen by the trapped ion (Eq. 2.7), and hence the secular frequencies, only the instantaneous electric field is required. Fig. 7.8 shows the result of the simulation. Here the voltage efficiency factor ϵ is plotted versus the tip-to-tip electrode distance. The parameter ϵ is found to level off to a value of approximately 17$\pm$1% for trap sizes $2z_0 \geq 75\mu$m. As the needles are gradually brought closer to one another, the efficiency is seen to approach zero. This is not so surprising when one considers the fact that in the limit where the needle spacing is smaller than the tip diameter, the electrode pair looks like a parallel plate capacitor, which of course lacks the electric field gradient required for a ponderomotive force. In the opposite limit, as the needle spacing becomes much larger than the tip diameter, the efficiency factor presumably levels off. Due to computational requirements, simulations could not be run to confirm this assumption.

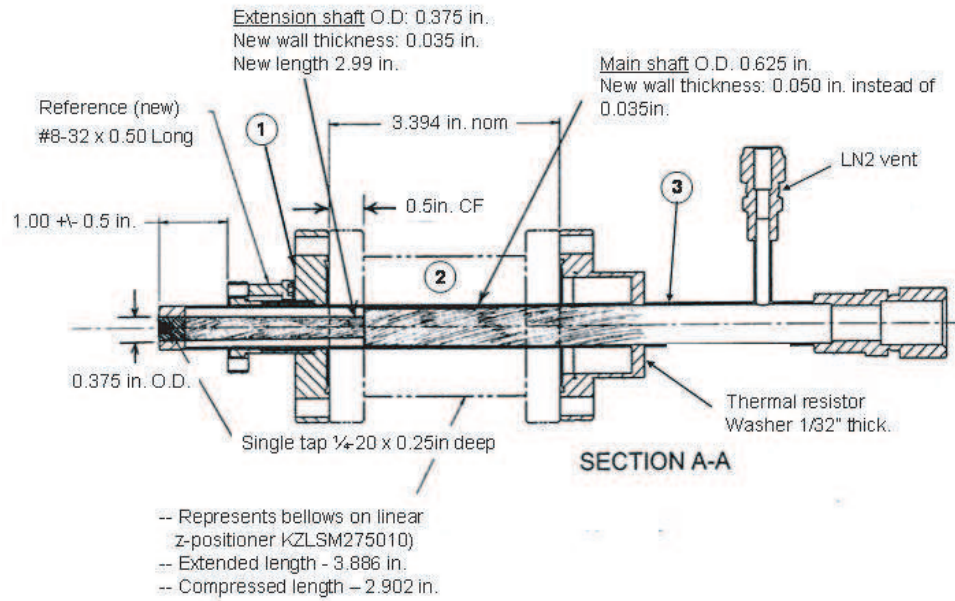[3]Maxwell (v10) - distributed by the Ansoft corporation.

LN2 Version 4

Extension shaft O.D: 0.375 in.
New wall thickness: 0.035 in.
New length 2.99 in.

Main shaft O.D. 0.625 in.
New wall thickness: 0.050 in. instead of 0.035in.

Reference (new)
#8-32 x 0.50 Long

3.394 in. nom

LN2 vent

1.00 +\- 0.5 in.

0.5in. CF

0.375 in. O.D.

Single tap ¼-20 x 0.25in deep

Thermal resistor
Washer 1/32" thick.

SECTION A-A

-- Represents bellows on linear
z-positioner KZLSM275010)
-- Extended length - 3.886 in.
-- Compressed length – 2.902 in.

Figure 7.6: A picture of the mainshaft assembly used to (1) hold each of the trap electrodes (needles), (2) translate the trap electrodes linearly with a resolution of $\pm 1\mu$m, and (3) provide thermal contact with a liquid nitrogen reservoir at 77 Kelvin. Part 1 is a reducing flange used to join the linear positioner (Part 2 on the right, CF 2 3/4) to the hemisphere (not shown on the left, CF 1 1/3). Part 2 is a linear positioner which allows the main shaft to be extracted (inserted) through and into the hemisphere. The only portion of the linear positioner shown in the drawing is the accordeon bellow allowing compression/extension over a range of 1 in. while keeping vacuum. Part 3 is the the main shaft ("cold finger") extending throughout the drawing. As depicted, this part is hollow allowing LN2 to be inserted. The thermal contact between the reservoir (LN2) and the trap electrode is at the end (left on drawing) of the main shaft. The trap electrode is mounted with a screw which fits into the end of the main shaft. All three parts were purchased from the Kurt J. Lesker Company.
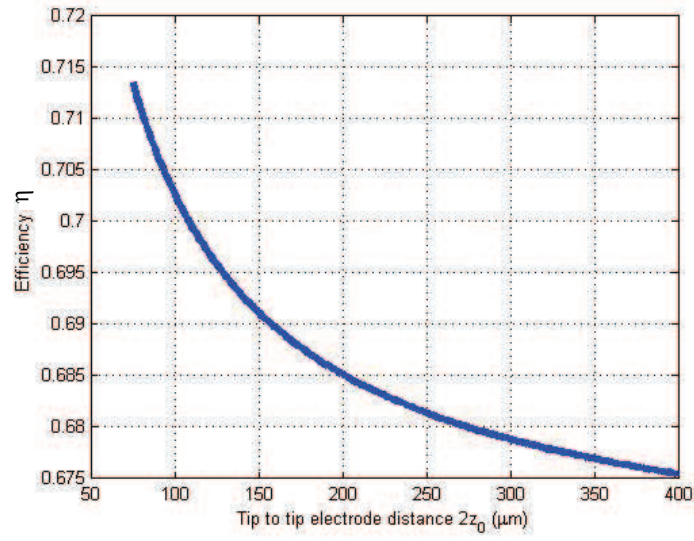
Figure 7.7: This plot shows the results of a simulation that calculates the geometrical efficiency factor η, which relates a given potential difference across the needle gap $2z_0$ to the resulting electric field at the ion position. This is useful for comparisons of heating rate to trap potential noise. The efficiency for the needle trap is 70% over the range of spacings used in the experiment.
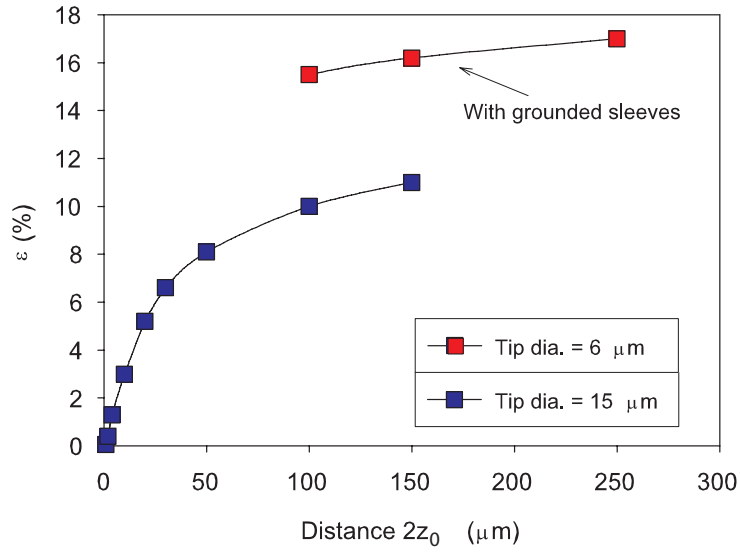
Figure 7.8: Voltage efficiency factor ϵ plotted versus the tip-to-tip electrode distance $(2z_0)$. Two different ion trap building iterations were necessary in order to find a two-needle design compatible with the controlled motional heating experiment. The lower graph (blue squares) shows the voltage efficiency factor ϵ vs the tip-to-tip distance $2z_0$ for the first two-needle trap, having a tip diameter of 15μm and conical shank of half-angle 4 degrees. This design did not have a nearby ground (no sleeves), resulting in a lower voltage efficiency. But most importantly, due to its susceptibility to slowly changing background electric fields from a lack of shielding, this open geometry was found to be inadequate for the motional heating experiment. The addition of nearby grounded sleeves in the second design iteration solved this problem. The needle tip diameter was reduced to 6μm while the conical shank half-angle remained 4 degrees. The voltage efficiency of the second design is shown (red squares) to be roughly constant over the distance interval of $75 \leq 2z_0 \leq 500\mu$m, with a value of $17\pm1\%$. This distance corresponds to the trap sizes used in the motional heating experiment. These results were simulated using a 3-D electrostatic simulation package (Maxwell v10).

7.4 Experimental results

Single cadmium ions are confined in the needle trap formed by two opposing electrodes in a vacuum chamber, as depicted in Fig. 7.9. A dual bifilar resonator is used to apply an electrical potential $U_0 + V_0 \cos(\Omega_{rf} t)$ with $\Omega_{rf}/2\pi = 29$ MHz to the needle electrodes, also shown in Fig. 7.9. In order to compensate for a uniform background electric field along the z direction, each electrode can be independently biased with a static potential difference δU_0. Ions are loaded into the trap by photoionizing a background vapor of Cd atoms at an estimated pressure of 10^{-11} Torr (chapter 5). The observed lifetime of an ion in the trap is typically several hours.

The axial secular oscillation frequency of an ion in the needle trap is given by

$$\omega_z = \sqrt{\frac{eU_0\epsilon}{mz_0^2} + \left(\frac{eV_0\epsilon}{\sqrt{2}m\Omega z_0^2}\right)^2} \tag{7.15}$$

under the pseudopotential approximation ($\omega_z \ll \Omega$) (chapter 2), where e is the charge and m the mass of the ion. The voltage efficiency factor η characterizes the reduction in trap confinement compared to the analogous quadrupole rf trap with hyperbolic electrodes of endcap spacing $2z_0$ and ring inner diameter $2\sqrt{2}z_0$ [35]. According to electrostatic simulations of the needle electrodes and grounded sleeves (Fig. 7.8), the voltage efficiency factor is $\epsilon = 0.17$ to within 5% over the range of ion-electrode distances $z_0 = 23 - 250\mu$m used in the experiment. Without the grounded sleeves, simulations predict that the voltage efficiency factor drops to $\epsilon \sim 0.06$, as the effective ground electrode is several cm removed from the needle tips. This is consistent with measurements of the trap frequency in an earlier (sleeveless) version of the trap. The axial secular oscillation frequency of a trapped ^{111}Cd$^+$ ion is measured to be $\omega_z/2\pi = 2.77$ MHz for $U_0 = 0$ V, $V_0 \sim 600$ V at $z_0 = 136\mu m$, consistent with simulations.

In order to measure the decoherence of ion motion in the trap, a single ^{111}Cd$^+$ ion is first laser-cooled to near the ground state of motion through stimulated-Raman sideband cooling, as described in chapter 6. Doppler pre-cooling prepares the ion in a thermal state with an average number of quanta $\bar{n} < 20$. Up to 60 cycles of
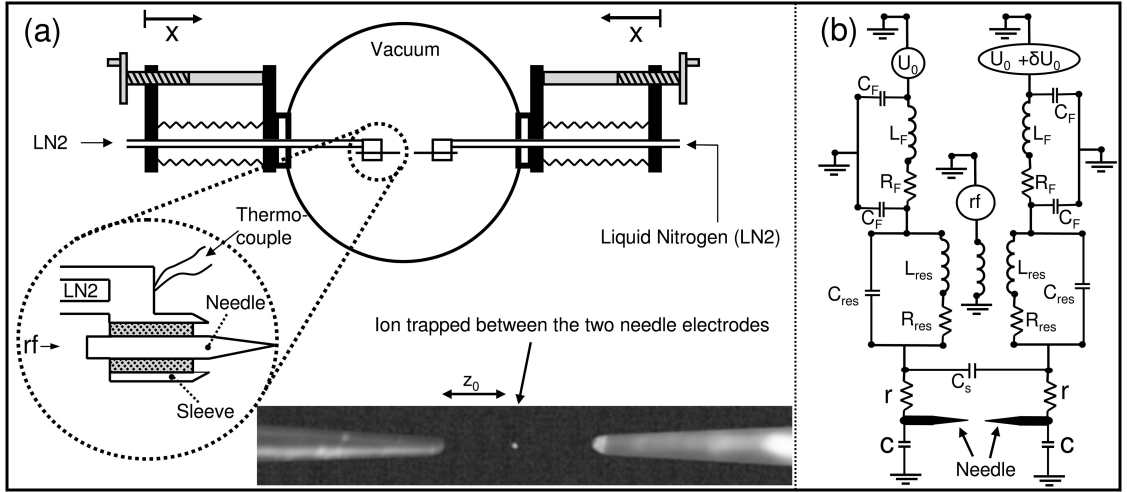
Figure 7.9: (a) A schematic of the ion trap used in this experiment. The tungsten electrodes are mounted on movable translation stages, allowing the distance between the electrodes $2z_0$ to be varied continuously from 0 to 1cm with a resolution of $\sim 1\mu$m. The electrodes can also be adjusted transversely with a resolution under $\sim 1\mu$m. As depicted in the inset, the rf voltage is directly applied to the needle electrode (part 1) while the sleeve (part 2) is held at 0 volts. The space between the sleeve and the needle is filled with alumina. The LN2 nitrogen used to cool the electrode is fed through the hollow stainless steel tube and is in thermal contact with the sleeve. A thermocouple used to monitor the temperature of the electrodes is attached to the sleeve. (b) A schematic of the resonator with the trap electrode circuit. V1 and V2 represent uncorrelated voltage noises (Johnson noises) originating in the series resistance in each filter box attached to each coil of the bifilar resonator. A shunt capacitor C_S is attached between the electrodes such that voltage noise from each coil can be applied symmetrically on both electrodes so as to reduce the voltage noise at the ion due to Johnson noise.

pulsed sideband cooling reduce the average occupation to $\bar{n} < 0.3$. As described previously, the value of $\bar{n}$ is determined by measuring an asymmetric ratio in the strength of the stimulated-Raman first-order blue and red sidebands, which is given by $\bar{n}/(1+\bar{n})$ for a thermal state of motion. We estimate that the systematic error in measuring $\bar{n}$ is no more than 10%, originating from effects such as ion fluorescence baseline drifts, Raman laser intensity imbalances on the sidebands, and non-thermal vibrational distributions. Motional decoherence is measured by inserting a delay time (up to $\tau = 50$ ms) after Raman cooling but before the sideband asymmetry probe. The decoherence or heating rate $\dot{\bar{n}}$ of trapped ion motion is then extracted from the slope of $\bar{n}(\tau)$, as shown in Fig. 7.10. The linear growth of $\bar{n}$ in time indicates that the time scale for the ion to reach equilibrium with the heat reservoir is much longer than the measurement time (e.g., for a reservoir at temperature 300K, it would take tens of years for the ion to reach equilibrium).
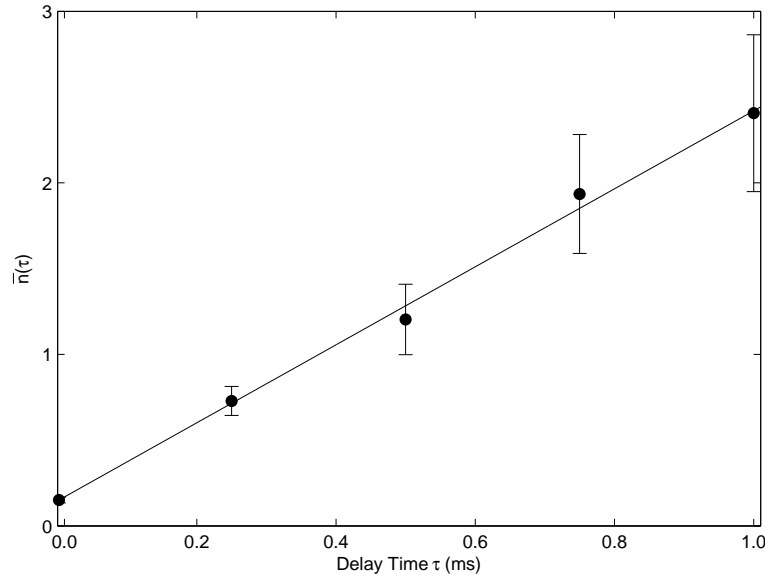

Figure 7.10: Average thermal occupation number $\bar{n}$ measured after various amounts of delay time τ. The axial trap frequency is $\omega_z/2\pi = 2.07$ MHz with an ion-electrode spacing of $z_0 = 64\mu$m. The linear growth in time indicates a motional decoherence or heating rate of $\dot{\bar{n}} = 2380 \pm 440$ quanta/sec.

Measurements of ion heating rates are presented in Fig. 7.11 at various trap frequencies ω_z for a fixed ion-electrode spacing of $z_0 = 103\mu$m. In this data set, the trap strength is varied by applying different static potentials U_0 while the rf potential amplitude is held constant at $V_0 \approx 600$ V, with an exception for the point at $\omega_z = 4.55$ MHz, where $V_0 \approx 700$ V. The data indicates that the heating rate decreases with trap frequency as $\dot{\bar{n}} \sim \omega_z^{-1.8\pm0.4}$, or equivalently that the electric field noise spectrum scales as $S_E(\omega) \sim \omega_z^{-0.8\pm0.4}$. Overall, these heating rates are similar to the previous measurements in other Cd^+ traps of similar size and strength (section 7.1), and anomalously higher than the level of heating expected from thermal electric field noise.
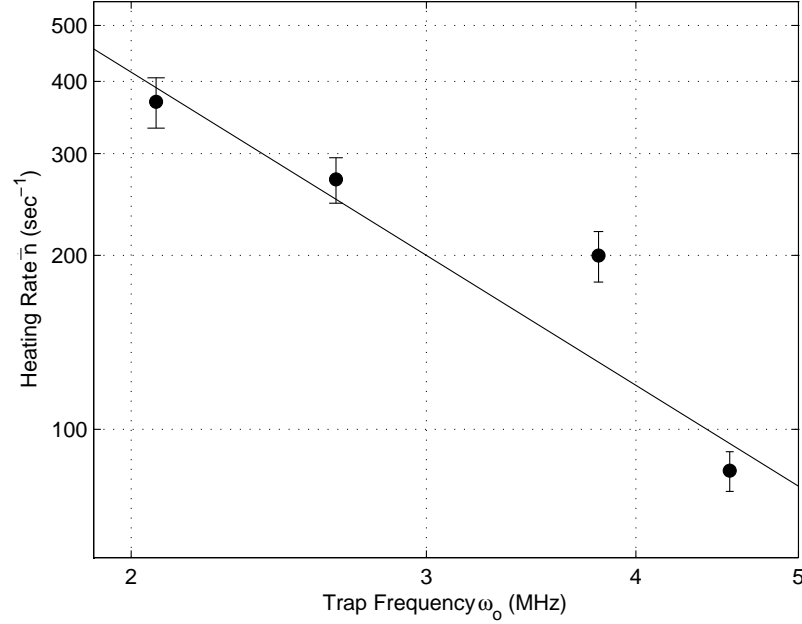

Figure 7.11: Measured axial heating rate $\dot{\bar{n}}$ as a function of axial motional trap frequency ω. For this data, the ion-electrode spacing is fixed at $z_0 = 103\mu$m and the trap strength is varied by changing only the static potential U_0 while fixing V_0, except for the highest frequency point where V_0 is 15% higher. The line is a fit to a power law, yielding $\dot{\bar{n}} \sim \omega^{-1.8\pm0.4}$, implying that the electric field noise spectral density varies roughly as $S_E(\omega) \sim \omega^{-0.8\pm0.4}$ over this frequency range.

The two needle electrodes are wired to independent but identical circuits (Fig. 7.9b), and the thermal (Johnson) noise from the resistive elements of the electrode circuits can be easily estimated. A circuit model with discrete elements is justified because the wavelength of the relevant time-varying fields is much larger than the trap structure. The net voltage noise across the needle electrodes is

$$S_V(\omega) = \frac{8k_B T R(\omega)}{1 + R(\omega)^2 C^2 \omega^2} + 8k_B T' r(\omega), \tag{7.16}$$

where k_B is Boltzmann's constant. The first term describes noise originating from a resistance $R(\omega)$ at temperature T attenuated by a capacitive low-pass filter, while the second term describes noise driven directly by resistance $r(\omega)$ at temperature T' after the capacitive filter. The net voltage noise $S_V(\omega)$ gives rise to an electric field noise at the ion of $S_E(\omega) = (\eta/2z_0)^2 S_V(\omega)$, where the geometrical efficiency factor $\eta \approx 0.7$ relates a given potential difference across the needle gap $2z_0$ to the resulting electric field at the ion position (see Fig. 7.7).

Thermal noise at frequency ω_z is driven by the series resistance of the needle electrode tips, estimated to be $\rho/(\pi r_0 tan\theta) \approx 0.1\Omega$, where ρ is the resistivity of the electrode material at 300 K, r_0 is the needle tip radius assumed to be much smaller than the skin depth multiplied by $tan\theta$, and θ is the half-cone angle of the conical shank. We expect a similar level of thermal noise from the upstream rf choke of resistance $R(\omega_z) = R_F \sim 3\Omega$, attenuated by filter capacitance $C_F + C_S = 0.2\mu F$ as shown in Fig. 7.9b. The thermal noise at the rf sideband frequencies $\Omega \pm \omega_z$ is dominated by the large effective resistance of the resonator circuit $R(\Omega \pm \omega_z) \approx (\Omega/2\omega_z)^2 R_{res}$ [36], where $R_{res} \sim 0.1~\Omega$ is the dc series resistance of the resonator. But this near-resonant enhancement is offset by the $(\omega_z/\Omega)^2$ term in Eq. 7.8, and because the resulting noise is strongly suppressed by the resonator shunt capacitor C_S, this source of thermal noise can be neglected compared to above. For "symmetric" trap designs where the rf electrodes symmetrically surround the ion and are wired together, the resulting common-mode thermal noise from the rf leads should vanish due to symmetry [36, 68] In summary, we expect a thermal heating rate of $\dot{n} \sim (200/z_0)^2(\omega_z/2\pi)^{-1}$ sec^{-1} at 300 K, where z_0 is expressed in μm and $\omega_z/2\pi$ in MHz.

At a temperature of 150 K, we expect a heating rate a factor of ~ 6 lower, including a factor of 3 reduction in the resistivity of tungsten.

Fig. 7.12 shows several measurements of heating rates at various values of the distance z_0 between the ion and the needle electrodes. In these measurements, the axial trap frequency is held to $\omega_z/2\pi = 2.07$ MHz by varying both the rf and static potentials V_0 and U_0 as the needle spacing is changed. Previous measurements of axial heating of trapped Cd^+ ions in the linear trap (section 7.1) show no correlation between the heating rate and the rf trapping voltage amplitude V_0. These earlier measurements were performed over similar ranges of rf voltages and trap frequencies as used for the current experiment. We therefore assume that the origin of anomalous heating measured for the needle trap is not directly influenced by the rf voltage amplitude. As seen in the figure (solid points), the heating rate fits well to a power law, scaling as $\dot{\bar{n}} \sim z_0^{-3.47 \pm 0.16}$. Again, the measured heating is much higher than that predicted from thermal fields and is in rough agreement with previous heating measurements [26, 18]. The observed anomalous heating is thought to originate from fluctuating patch potentials on the electrode surfaces, and the scaling of this heating with electrode proximity provides valuable information regarding the spatial size of presumed patches. For patches that are much smaller than the electrode tip, the electric field noise is expected to scale as z_0^{-4}. The electric field from a single patch on a planar or concave conducting surface is expected to scale in the far field as z^{-3}, from the dipole field originating from the patch and its image [26]. However, for a convex surface such as the needle electrodes in this work, the image does not balance the original patch, and the electric field scales as z_0^{-2}, as if from a free charge. The electric field noise power scales as the square of these expressions. For uniformly distributed microscopic patches on the needle electrodes, the electric field noise is expected to scale between z^{-2} and z^{-4}, depending on the details of the geometry and the patch density. On the other hand, correlated voltage noise across the entire electrode structure (e.g., from thermal Johnson noise or applied voltage noise) is expected to scale as z^{-2}. The observed intermediate $z^{-3.5}$ scaling indicates that anomalous ion heating indeed originates from very small patch potentials.
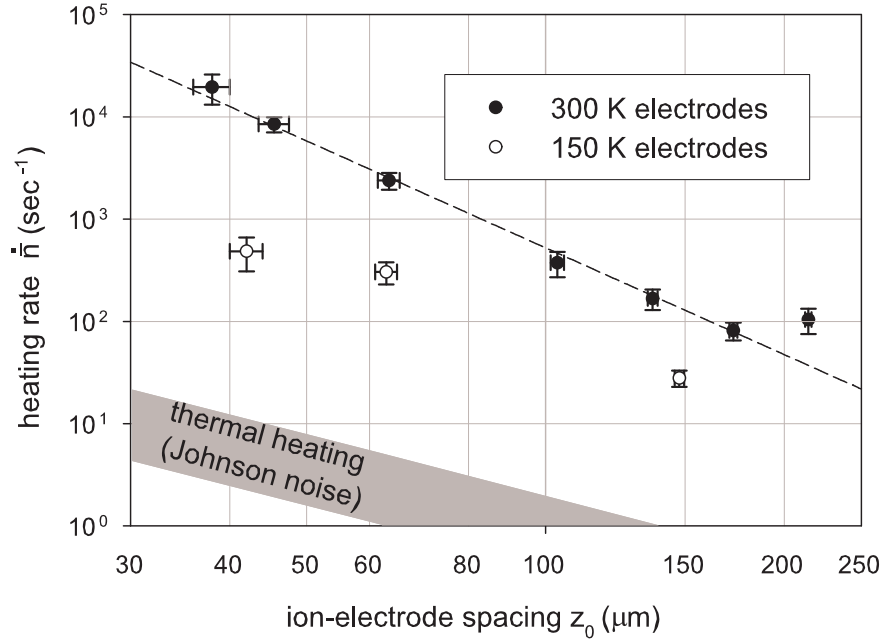
Figure 7.12: Axial heating rate $\dot{\bar{n}}$ as a function of distance z_0 from trapped ion to each needle electrode, for warm and cold electrodes. All of the data corresponds to a trap frequency of $\omega_z/2\pi = 2.07$ MHz, as the rf and static trapping potentials are increased as the trap is made larger. The measurements fit well to a scaling of heating rate with trap dimension of $\dot{\bar{n}} \sim z_0^{-3.47\pm0.16}$ (dashed line). The lower set of measurements (hollow points) are acquired with the needle electrodes cooled to approximately 150K through contact with a liquid nitrogen reservoir. These three points were measured using one and the same trapped atomic ion. (The 42μm cold measurement was performed at $\omega_z/2\pi = 4.9$ MHz and has been scaled upward by a factor of ~ 3 to the expected heating rate at $\omega_z/2\pi = 2.07$ MHz.) The shaded band at bottom, scaling as z_0^{-2}, is the expected range of heating from thermal noise from the trap circuitry.

We repeat the measurement of axial motional heating rate of a trapped ion at various values of z_0, but this time with the needle electrodes cooled via contact with a liquid nitrogen reservoir. While the electrode mount is measured to be 80 ± 5 K with a vacuum thermocouple, the needle tip is significantly hotter due to absorption of blackbody radiation at 300 K and the limited heat conduction from the very narrow needle electrode to the mount. We measure the shank of the needle to be 120 K, and we estimate that the needle tips are cooled to a temperature of 150 ± 20 K. The measured heating rates for cold trap electrodes is plotted in the lower set of data in Fig. 7.12. The three measurements were performed on one and the same atomic cadmium ion, over a 6-hour period. The measured heating rate with cold electrodes is still higher than the expected thermal noise by about two orders of magnitude, as shown in the figure. However, the nonlinear dependence of observed ion heating with electrode temperature is clear. The ion heating rate is reduced by a factor of ten or more for a decrease in electrode temperature by only a factor of two, suggesting that the anomalous heating observed in ion traps may be thermally driven and activated at a threshold temperature, and that further cooling to 77 K or lower may even quench this anomalous heating completely.

In summary, we present a series of controlled measurements of trapped ion motional decoherence, varying both the proximity of the ion to the electrodes and the temperature of the electrodes. These measurements are performed in a novel movable ion trap structure that confines laser-cooled ions closer to the electrodes than any previous ion trap. The measurements of heating in this system provide some information regarding the spatial size of presumed fluctuating surface patch potentials in ion traps, while also showing that the heating is strongly suppressed through modest cooling of the electrodes. While the mechanism of heating remains unclear, by comparing the heating data obtained from the needle trap side by side with historical data from other ion systems as shown in Fig. 7.13 and Fig. 7.14, we can see that, although very noisy, it seems consistent with a scaling near $1/d^4$. This investigation into a poorly understood source of motional decoherence in trapped ions is of great interest to ion trap quantum information processing and may also have relevance to

condensed matter systems that are sensitive to fluctuating electrical potentials.
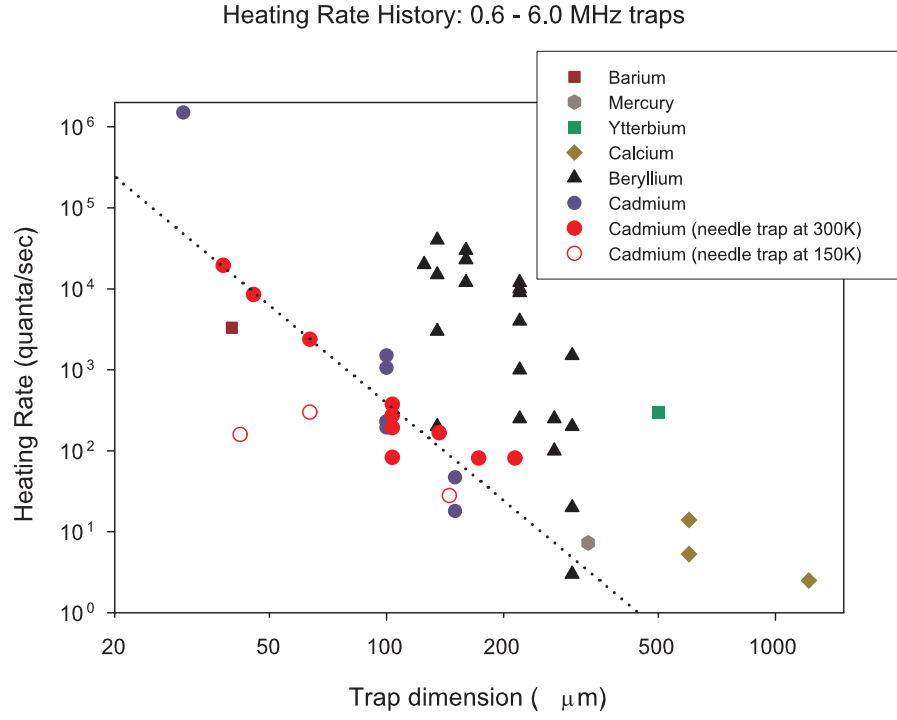

Figure 7.13: A combination of all the heating data $\dot{\bar{n}}$ from the needle trap and from other ion trap research groups worldwide. The heating measurements are shown for trap frequencies from 0.6-6.0 MHz. The dashed line is a guide to the eye for $1/d^4$ scaling.
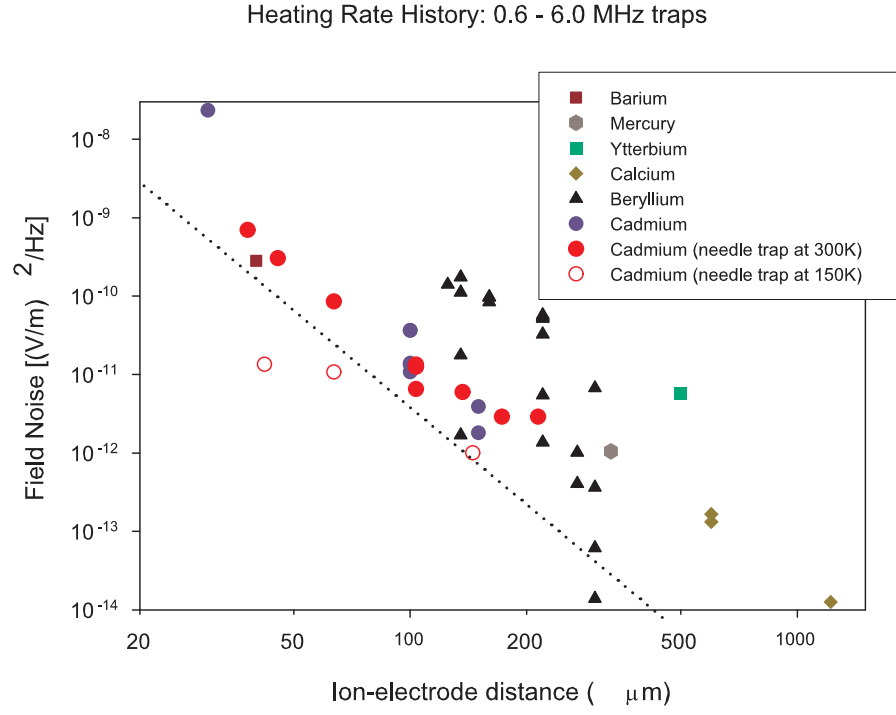
Figure 7.14: A combination of all the spectral density of electric field noise $S_E(\omega_x)$ data from the needle trap and from other ion trap research groups worldwide. Since $S_E(\omega_x)$ does not depend on any particular trapped-ion species, it provides a useful metric for comparison. The heating measurements are shown for trap frequencies from 0.6-6.0 MHz. The dashed line is a guide to the eye for $1/d^4$ scaling.

BIBLIOGRAPHY

BIBLIOGRAPHY

[1] A Einstein, B Podolsky, and N Rosen, "Can Quantum-Mechanical Description of Physical Reality Be Considered Complete?,," Phys. Rev. **47**, 777 (1935).

[2] E Schrödinger, Naturwissenschaften **23**, 807 (1935).

[3] M A Nielsen and I L Chuang, *Quantum Computation and Quantum Information.*, Cambridge, Cambridge (2000).

[4] A Steane, "The Ion Trap Quantum Information Processor," Appl. Phys. B **64**, 623 (1997).

[5] P K Ghosh, *Ion Traps*, Clarendon Press, Oxford (1995).

[6] F M Penning, volume 3, Amsterdam (1936).

[7] D Wineland, P Ekstrom, and H Dehmelt, "Monoelectron Oscillator," Phys. Rev. Lett. **31**(21), 1279 (1973).

[8] W Paul, "Electromagnetic traps for charged and neutral particles," Rev. Mod. Phys. **62**, 531 (1990).

[9] W Neuhauser M Hohenstatt, P E Toschek, and H Dehmelt, "Localized visible Ba^+ mono-ion oscillator," Phys. Rev. A **22**(3), 1137 (1980).

[10] N F Ramsey, *Molecular Beams*, Oxford University Press, London (1963).

[11] D J Wineland and H G Dehmelt, Bull. Am. Phys. Soc. **20**, 637 (1975).

[12] T W Hänsch and A L Schawlow, Opt. Commun. **13**, 68 (1975).

[13] D J Wineland, R E Drullinger, and F L Walls, Phys. Rev. Lett. **40**, 1639 (1978).

[14] W Neuhauser, M Hohenstatt, P Toschek, and H Dehmelt, Phys. Rev. Lett. **41**, 233 (1978).

[15] F Diedrich, J C Bergquist, W M Itano, and D J Wineland, "Laser Cooling to the Zero-Point Energy of Motion," Phys. Rev. Lett. **62**(14), 403 (1989).

[16] C Monroe, D M Meekhof, B E King, S R Jefferts, W M Itano, D J Wineland, and P Gould, "Resolved-Sideband Raman Cooling of a Bound Atom to the 3D Zero-point Energy," Phys. Rev. Lett. **75**(22), 4011 (1995).

[17] Ch Roos, Th Zeiger, H Rohde, H C Ngerl, J Eschner, D Leibfried, F Schmidt-Kaler, and R Blatt, "Quantum State Engineering on an Optical Transition and Decoherence in a Paul Trap," Phys. Rev. Lett. **83**, 4713 (1999).

[18] L Deslauriers, P C Haljan, P J Lee, K-A Brickman, B B Blinov, M J Madsen, and C Monroe, "Zero-Point Cooling and Low Heating of Trapped Cd Ions," Phys. Rev. A **70**, 043408 (2004).

[19] P W Shor, "Algorithms for Quantum Computation: Discrete Logarithms and Factoring," in "Proceedings of the 35th Annual Symposium on the Foundations of Computer Science," page 124, IEEE Computer Society, IEEE Computer Society Press, New York (1994).

[20] J I Cirac and P Zoller, "Quantum Computation with Cold, Trapped Ions," Phys. Rev. Lett. **74**(20), 4091 (1995).

[21] C Monroe, D M Meekhof, B E King, W M Itano, and D J Wineland, "Demonstration of a Fundamental Quantum Logic Gate," Phys. Rev. Lett. **75**(25), 4714 (1995).

[22] D J Berkeland, J D Miller, J C Bergquist, W M Itano, and D J Wineland, "Laser-Cooled Mercury Ion Frequency Standard," Phys. Rev. Lett. **80**(10), 2089 (1998).

[23] A Sørensen and K Mølmer, "Quantum computation with ions in thermal motion," Phys. Rev. Lett. **82**, 1971 (1999).

[24] E Solano, R L de Matos Filho, and N Zagury, "Two-ion entanglement," Phys. Rev. A **59**, 2539 (1999).

[25] G J Milburn, S Schneider, and D F V James, Fortschr. Physik (2000).

[26] Q A Turchette, D Kilepinski, B E King, D Leibfried, D M Meekhof, C J Myatt, M A Rowe, C A Sackett, C S Wood, W M Itano, C Monroe, and D J Wineland, "Heating of trapped ions from the quantum ground state," Phys. Rev. A **61**, 063418 (2000).

[27] M A Rowe, A Ben-Kish, B DeMarco, D Leibfried, V Meyer, J Beall, J Britton, J Hughes, W M Itano, B Jelenkovic, C Langer, T Rosenband, and D J Wineland, "Transport of quantum states and separation of ions in a dual rf ion trap," Quantum Information and Computation **2**, 257 (2002).

[28] R G DeVoe, J Hoffnagle, and R G Brewer, "Role of laser damping in trapped ion crystals," Phys. Rev. A **39**, 4362 (1989).

[29] W Nagourney, J Sandberg, and H G Dehmelt, "Shelved Optical Electron Amplifier: Observation of Quantum Jumps," Phys. Rev. Lett. **56**(26), 2797 (1986).

[30] Th Sauter, W Neuhauser, R Blatt, and P E Toschek, "Observation of Quantum Jumps," Phys. Rev. Lett. **57**(14), 1696 (1986).

[31] J C Bergquist, R G Hulet, W M Itano, and D J Wineland, "Observation of Quantum Jumps in a Single Atom," Phys. Rev. Lett. **57**(14), 1699 (1986).

[32] B Blinov, D L Moehring, L-M Duan, and C Monroe, "Observation of entanglement between a single trapped atom and a single photon," Nature **428**, 153 (2004).

[33] D J Griffiths, *Introduction to Electrodynamics - 3rd ed.*, Prentice Hall, New Jersey (1999).

[34] D W Jordan and P Smith, *Nonlinear ordinary differential equations*, Oxford, Great Clarendon Street, Oxford (1999).

[35] H G Dehmelt, "Radiofrequency Spectroscopy of Stored Ions I: Storage," Adv. Atom. Mol. Phys. **3**, 53 (1967).

[36] D J Wineland, C Monroe, W M Itano, D Leibfried, B E King, and D M Meekhof, "Experimental issues in coherent quantum-state manipulation of trapped atomic ions," J. Res. Nat. Inst. Stand. Tech. **103**, 259 (1998).

[37] S R Jefferts, C Monroe, A S Barton, and D J Wineland, "Paul trap for optical frequency standards," IEEE Transaction on Instrumentation and Measurement **44**(2), 148 (1995).

[38] W K Hensinger, S Olmschenk, D Stick, D Hucul, M Yeo, M Acton, L Deslauriers, and C Monroe, "T-juntion ion trap array for two dimensional ion shuttling, storage and manipulation," Appl. Phys. Lett. **88**, 034101 (2006).

[39] D J Wineland and W M Itano, "Laser Cooling of Atoms," Phys. Rev. A **20**(4), 1521 (1979).

[40] R G DeVoe and C Kurtsiefer, "Experimental study of anomalous heating and trap instabilities in a microscopic ^{137}Ba$^+$ ion trap," Phys. Rev. A **65**, 063407 (2002).

[41] W W Macalpine and R O Schildknecht, "Coaxial resonators with helical inner conductor," Proceedings of the IRE (1959).

[42] W W Macalpine and R O Schildknecht, "Helical resonator design chart," Electronics **33**, 140 (1960).

[43] P R Berman, editor, *Cavity Quantum Electrodynamics*, Academic Press, Inc., New York (1994).

[44] B Blinov, D Leibfried, C Monroe, and D J Wineland, "Quantum Computing with Trapped Ion Hyperfine Qubits," (2004).

[45] B Blinov, L Deslauriers, P Lee, M Madsen, R Miller, and C Monroe, "Sympathetic Cooling of Trapped Cd+ Isotopes," Phys. Rev. A **65**, 040304 (2002).

[46] D L Moehring, B B Blinov, D W Gidley, R N Kohn, M J Madsen, T B Sanderson, R S Vallery, and C Monroe, "Precision Lifetime Measurement of a Single Trapped Ion with Ultrafast Laser Pulses," quant-ph/0505111 (2005).

[47] A Kastler, J. Phys. Rad. **11**, 255 (1950).

[48] H J Metcalf and P van der Straten, *Laser Cooling and Trapping*, Springer, New York (1999).

[49] M Acton, K-A Brickman, P C Haljan, P J Lee, L Deslauriers, and C Monroe, "Near-Perfect Simultaneous Measurement of a Qubit Register," quant-ph/0511257 (2005).

[50] W M Itano, J C Bergquist, J J Bollinger, J M Gilligan, D J Heinzen, F L Moore, M G Raizen, and D J Wineland, "Quantum projection noise: Population fluctuations in two-level systems," Phys. Rev. A **47**(5), 3554 (1993).

[51] R P Feynman, F L Vernon Jr, and R W Hellwarth, "Geometrical representation of the Schrödinger equation for solving maser problems." J. Appl. Phys. **28**, 49 (1957).

[52] J J Sakurai, *Modern Quantum Mechanics*, Addison Wesley, New Jersey (1994).

[53] M Abramowitz and I A Stegun, *Handbook of Mathematical Functions*, U.S. Gov't. Printing Office, Washington, D.C. (1964).

[54] D P DiVincenzo, "Two-bit gates are universal for quantum computation," Phys. Rev. A **51**(2), 1015 (1995).

[55] G Rempe and H Walther, "Observation of quantum collapse and revival in a one-atom maser," Phys. Rev. Lett. **58**(4), 353 (1987).

[56] P J Lee, B B Blinov, K Brickman, L Deslauriers, M J Madsen, R Miller, D L Moehring, D Stick, and C Monroe, "Atomic qubit manipulations with an electro-optic modulator," Optics Lett. **28**, 1852 (2003).

[57] P J Lee, K A Brickman, L Deslauriers, P C Haljan, L M Duan, and C Monroe, "Phase control of trapped ion quantum gates," J. Opt. B: Quantum Semiclass. Opt. **7**, S371 (2005).

[58] M T Asaki, C Huang, D Garvey, J Zhou, H C Kapteyn, and M M Murnane, "Generation of 11-fs pulses from a self-mode-locked Ti:Sapphire laser," Opt. Lett. **18**, 977 (1993).

[59] H Kapteyn, "private communication," (2005).

[60] N Kjaergaard, L Hornekaer, A M Thommesen, Z Videsen, and M Drewsen, "Isotope selective loading of an ion trap using resonance-enhanced two-photon ionization," Appl. Phys. B **71**, 207 (2000).

[61] S Gulde, D Rotter, P Barton, F Schmidt-Kaler, R Blatt, and W Hogervorst, "Simple and efficient photo-ionization loading of ions for precision ion-trapping experiments," Appl. Phys. B **73**, 861 (2001).

[62] D M Lucas, A Ramos, J P Home, M J McDonnell, S Nakayama, J-P Stacey, S C Webster, D N Stacey, and A M Steane, "Isotope-selective photoionization for calcium ion trapping," Phys. Rev. A **69**(1), 012711 (2004).

[63] C. Cohen-Tannoudji, J. Dupont-Roc, and G. Grynberg, *Photons and Atoms: Introduction to Quantum Electrodynamics*, Wiley, New York (1989).

[64] D N Madsen, S Balslev, M Drewsen, N Kjrgaard, Z Videsen, and J W Thomsen, "Measurements on photo-ionization of $3s3p^1P_1$ magnesium atoms," J. Phys. B: At. Mol. Opt. Phys. **33**, 4981 (2000).

[65] LW He, C E Burkhardt, M Ciocca, J J Leventhal, and S T Manson, "Absolute cross sections for the photoionization of the $6s6p^1P$ excited state of barium," Phys. Rev. Lett. **67**(16), 2131 (1991).

[66] R R Adzhimambetov I Sh Muzhdabaev A T Tursunov and Khalilov, "Study of the CdS Crystal Evaporation Kinetics by Laser Step Atomic Photoionization," Technical Physics (Zhurnal Tekhnicheskoi Fiziki) **48**, 1020 (2003).

[67] F Rosebury, "Handbook of Electron Tube and Vacuum Techniques," American Institute of Physics, New York (1993).

[68] D Stick, W K Hensinger, S Olmschenk, M J Madsen, K Schwab, and C Monroe, "Ion Trap in a Semiconductor Chip," Nature Physics **2**, 36 (2006).

[69] J J Bollinger, D J Heinzen, W M Itano, S L Gilbert, and D J Wineland, "A 303-MHz Frequency Based on Trapped Be$^+$ Ions," IEEE Trans. Instr. Meas. **40**(2), 126 (1991).

[70] D. Kielpinski, C Monroe, and D J Wineland, "Architecture for a large-scale ion-trap quantum computer," Nature **417**, 709 (2002).

[71] D J Larson, J C Bergquist, J J Bollinger, W M Itano, and D J Wineland, "Sympathetic cooling of trapped ions: A laser-cooled two-species nonneutral ion plasma," Phys. Rev. Lett. **57**, 70 (1986).

[72] D Kielpinski, B E King, C J Myatt, C A Sackett, Q A Turchette, W M Itano, C Monroe, and D J Wineland, "Sympathetic cooling of trapped ions for quantum logic," Phys. Rev. A **61**, 032310 (2000).

[73] G Morigi and H Walther, "Two-species Coulomb chains for quantum information," Eur. Phys. J. D. **13**(2), 261 (2001).

[74] H Imajo, K Hayasaka, R Ohmukai, U Tanaka, M Watanabe, and S Urabe, "High-resolution ultraviolet spectra of sympathetically-laser-cooled Cd$^+$ ions," Phys. Rev. A **53**, 122 (1996).

[75] H Rohde, S T Gulde, C F Roos, P A Barton, D Leibfried, J Eschner, F Schmidt-Kaler, and R Blatt, "Sympathetic ground-state cooling and coherent manipulation with two-ion crystals," J. Opt. B: Quantum Semiclassic. Opt. **3**(1), S34 (2001).

[76] M D Barrett, B DeMarco, T Schaetz, V Meyer, D Leibfried, J Britton, J Chiaverini, W M Itano, B Jelenkovic, J D Jost, C Langer, T Rosenband, and D J Wineland, "Sympathetic cooling of $^9Be^+$ and $^{24}Mg^+$ for quantum logic," Phys. Rev. A **68**, 042302 (2003).

[77] Q A Turchette, C S Wood, B E King, C J Myatt, D Leibfried, W M Itano, C Monroe, and D J Wineland, "Deterministic entanglement of two trapped ions," Phys. Rev. Lett. **81**, 1525 (1998).

[78] J P Home and A M Steane, "Electric Octopole Configurations for Fast Separation of Trapped Ions," quant-ph/0411102 (2005).

[79] O Astafiev, Yu A Pashkin, Y Nakamura, T Yamamoto, and J S Tsai, "Quantum Noise in the Josephson Charge Qubit," Phys. Rev. Lett. **93**, 267007 (2004).

[80] J M Martinis, S Nam, J Aumentado, and K M Lang, "Decoherence of a superconducting qubit due to bias noise," **67**, 094510 (2003).

[81] J B Camp, T W Darling, and R E Brown, "Macroscopic variations of surface potentials of conductors," J. Appl. Phys. **69**, 7126 (1997).

[82] J W Goodman, *Statistical Optics*, John Wiley & Sons, Inc., New York (1985).

[83] H G Dehmelt and F L Walls, Phys. Rev. Lett. **21**, 127 (1968).

[84] D J Wineland and H G Dehmelt, "Principles of the Stored Ion Calorimeter," J. Appl. Phys. **46**(2), 919 (1975).

[85] J B Johnson, Phys. Rev. **21**, 127 (1932).

[86] V Sandoghdar, C I Sukenik, S Haroche, and E A Hinds, Phys. Rev. A **53**, 1919 (1996).

[87] G Gabrielse, A Khabbaz, D S Hall, C Heimann, H Kalinowsky, and W Jhe, Phys. Rev. Lett. **82**, 3198 (1999).

[88] C Kleint, Ann. Phys. (Leipzig) **10**, 309 (1963).

[89] G W Timm and A Van der Ziel, Physica (Utrecht) **32**, 1333 (1966).